DISSERTATION

Simulation of Particle Failure in Particle Reinforced Ductile Matrix Composites

ausgeführt zum Zwecke der Erlangung des akademischen Grades eines
Doktors der technischen Wissenschaften unter der Leitung von

ao.Univ.Prof. Dipl.-Ing. Dr.techn. Helmut Johann BÖHM, MSc.
E317
Institut für Leichtbau und Flugzeugbau

eingereicht an der Technischen Universität Wien
Fakultät für Maschinenbau

von

Dipl.-Ing. Anton ECKSCHLAGER
Matrikelnummer: 9027349
Schließmanngasse 5-7/A/5
A-1130 Wien

Wien, im August 2002   Anton Eckschlager

Contents

Acknowledgments

Nomenclature

Symbols

a	crack length
a_0	reference crack length
$a_\mathrm{c}(\sigma)$	critical flaw at stress distribution σ
$D_\mathrm{i}^{(\mathrm{m})}$	damage indicator in the matrix phase
d_n	normal separation function
d_t	tangent separation function
δ_i	normal/tangent separation
$\delta_{i,0}$	normal/tangent maximum separation
$\delta_{\mathrm{n},0}$	normal maximum separation
$\delta_{\mathrm{t},0}$	tangent maximum separation
ε	strain
$\underline{\underline{\varepsilon}}$	strain tensor
ε_{ij}	strain tensor components
ε^a	applied strain in the uniaxial case
$\varepsilon_\mathrm{uniaxial}^\mathrm{max}$	uniaxial strain maximum
$\varepsilon_\mathrm{eq,p}$	accumulated equivalent plastic strain
$\dot{\varepsilon}_\mathrm{eq,p}$	equivalent plastic strain rate
ε_0	uniaxial failure strain (ductile failure)
ε_f	multiaxial failure strain (ductile failure)
$\eta^{(\mathrm{m})}$	triaxiality of the matrix stress tensor
E	elastic modulus
E^*	effective elastic modulus
$f(\sigma)$	general function dependent on stress σ
$g(a)$	distribution function of microdefects
θ, φ	crack orientation angles

$I_k(r)$	number of particle centers within a spherical volume of radius r
K_I	stress intensity factor, mode I
K_II	stress intensity factor, mode II
K_III	stress intensity factor, mode III
$K_\mathrm{I,eq}$	equivalent stress intensity factor, mode I
$K_\mathrm{I,c}$	critical stress intensity factor, mode I
$l_{0,i}$	initial unit cell edge length in direction $i = 1, 2, 3$
m	Weibull modulus
M_1	separation function coefficient M1
M_2	separation function coefficient M2
M_n	normal separation function coefficient
M_t	tangent separation function coefficient
$\underline{n}$	normal vector
$\bar{n}(r)$	mean number of inclusions within a spherical volume of radius r
$n(\sigma)$	density of risk of fracture
$\langle N_{\mathrm{c},V} \rangle$	average number of critical defects in a volume
N_V	total number of particle centers within a volume V
ν	Poisson's ratio
ν^*	effective Poisson's ratio
Φ_sep	interface decohesion separation work
P_fr	fracture probability
$P_{\mathrm{fr},j}$	fracture probability of particle j
P_s	survival probability
$P_\mathrm{fr}^\mathrm{cr}$	critical particle fracture probability
$P_{\mathrm{fr},j}^{(\mathrm{tol})}$	fracture probability limit of particle j
$P_{\mathrm{fr},j}^{(\mathrm{actual})}$	actual Weibull fracture probability of particle j
$P_{\mathrm{fr},j}^{(\mathrm{max})}$	maximum survived Weibull fracture probability of particle j
$\underline{r}$	position vector
r_0	radius
σ	stress
$\underline{\underline{\sigma}}$	stress tensor
σ_{ij}	stress tensor components
$\underline{\sigma}$	stress vector (traction vector)
σ^a	applied stress evaluated by the simulation
σ_cr	critical stress

$\sigma_{\mathrm{I,c}}$ critical stress for mode I fracture

$\sigma_{\mathrm{I,eq}}$ equivalent stress for mode I fracture

σ_{eq} effective/v. Mises stress

σ_{fr} fracture stress

σ_{H} hydrostatic stress

σ_{u} lower stress limit

σ_1 maximum principal stress

σ_2 intermediate principal stress

σ_3 minimum principal stress

σ_{m} mean stress

$\sigma_{\perp}$ normal stress with respect to a plane

σ_0 Weibull characteristic strength

$\sigma_{0,I}$ Weibull characteristic strength for mode I fracture

σ_{y} yield stress

${}^{0}\sigma_{\mathrm{y}}^{(\mathrm{m})}$ initial yield stress of matrix

$\tau_{\parallel}$ in-plane shear stress

$\underline{t}_1, \underline{t}_2$ unit vectors lying in-plane

T traction field at an interface

T_{n} normal traction components at an interface

T_{t} tangential traction components at an interface

$T_{n,0}$ limit normal traction component on surface

$T_{t,0}$ limit tangential traction component on surface

u_i separation

u_{n} normal separation

u_{t} tangential separation

V_0 Weibull normalising parameter, reference volume V_0

$V_{\mathrm{model}}^{(\mathrm{geom})}$ model volume, geometrically determined

$V_{\mathrm{model}}^{(\mathrm{int})}$ integration volume (computed volume)

Y_{I} geometry factor, mode I fracture

Y_{II} geometry factor, mode II fracture

Y_{III} geometry factor, mode III fracture

Symbols, Superscripts and Subscripts

$^{(m)}$ Matrix

$^{(p)}$ Particle

$\langle\rangle$ Average

Abbreviations

arr.	arrangement
CTE	Coefficients of Thermal Expansion
FE Method	Finite Element Method
HIP	Hot Isostatic Pressing
HSS	High Speed Steel
MMC	Metal Matrix Composite
PRDMC	Particle Reinforced Ductile Matrix Composite
PDF	Pair Distribution Function
PIA	Principle of Independent Action
PM	Powder Metallurgical
RPC	Randomly Pruned Cubic (arrangement)
RSA	Random Sequential Adsorption (arrangement)
RVE	Representative Volume Element
SEM	Scanning Electron Microscope
sc	simple cubic arrangement
bcc	body centered cubic arrangement
fcc	face centered cubic arrangement
WLT	Weakest Link Theory
WR-model	Weibull Rankine model
MCW-model	Monte Carlo Weibull model

Abbreviations for Modeled Materials

$AA2618/SiC_p\text{-}T4$	MMC-aluminimum reinforced by SiC particles
$HSS^{\mu y}_{\text{vol.\%}}$	HSS microstructure of type μy (where $y = 1, \ldots, 9$)

Abstract

The aim of the present study is the modeling of the successive brittle failure of particles embedded in a ductile matrix subjected to global uniaxial tensile loading. The work is based on three-dimensional multi-particle unit cells and uses the Finite Element method. Micro-geometries are generated by appropriately arranging a number of spherical particles within the unit cell. On the one hand so called Randomly Pruned Cube (RPC) arrangements are employed, in which the unit cell is split into a number of cube-shaped subvolumina some of which are randomly selected to contain a centered particle. On the other hand periodic pseudo-random particle arrangements are generated by a modified Random Sequential Adsorption (RSA) algorithm. Elastic material properties are used for the particles and the matrix is described by J_2 plasticity.

Predefined fracture surfaces, which are assumed to be oriented perpendicularly with respect to the direction of the overall uniaxial stress state, are provided for within the reinforcements. Brittle failure of the reinforcements, which is modeled as instantaneous cleavage at these surfaces, is implemented by a node release technique. Failure in a given particle is controlled by Weibull-type fracture probabilities in combination with a Monte Carlo algorithm. The fracture probabilities are evaluated for the whole particle on the basis of the current stress distribution.

Within the modeling assumptions used, which do not account for other local failure mechanisms such as ductile damage of the matrix and decohesion at the interface between the constituents, successive particle cleavage and the resulting stress redistribution effects are simulated for two types of materials, a particle reinforced aluminium matrix composite and a high speed tool steel. Results are presented in terms of predictions for the overall stress vs. strain behavior and for damage relevant fields at the microscale for the above types of composite, which represent materials with highly ductile and rather hard matrices. Special consideration is given to influences of the material properties and the relative sizes of the particles on the predicted fracture behavior.

Kurzfassung

Das Ziel der vorliegenden Arbeit ist die Modellierung des sukzessiven spröden Versagens von in einer duktilen Matrix eingebetteten und global einachsig belasteten Partikeln. Die Arbeit basiert auf dreidimensionalen Mehrpartikel-Einheitszellen und verwendet die Finite Elemente Methode. Die Mikrogeometrien wurden durch die geeignete Anordnung einer Anzahl von Partikeln in der Einheitszelle generiert. Einerseits wurden sogenannte Randomly Pruned Cube (RPC) Geometrien entwickelt, für die die Einheitszelle in eine bestimmte Anzahl von Subvolumina aufgespalten wird und von welchen einige zufallsgesteuert ein zentral positioniertes Partikel beinhalten. Andererseits wurden periodische pseudozufällige Partikelanordnungen mittels eines modifizierten Random Sequential Adsorption (RSA) Algorithmus generiert. Für die Partikel wurden elastische Materialeigenschaften verwendet und die Matrix wurde mit einem J_2-Plastizitätsmodell beschrieben.

Bruchflächen sind innerhalb der Verstärkungsphase vordefiniert und werden als normal zur Richtung der globalen einachsigen makroskopischen Spannung angenommen. Sprödes Versagen der Verstärkungsphase, welches als instantanes Versagen an diesen Flächen modelliert wird, ist mittels einer Knotenöffnungstechnik implementiert. Das Versagen der individuellen Partikel wird durch Bruchwahrscheinlichkeiten vom Weibull-Typ in Kombination mit einem Monte-Carlo-Algorithmus gesteuert. Die Bruchwahrscheinlichkeiten werden auf Basis der aktuellen Spannungsverteilung für das ganze Partikel berechnet.

Innerhalb der verwendeten Modellierungsannahmen, die andere lokale Versagensmechanismen, wie duktile Schädigung der Matrix und Ablösung am Interface zwischen den Konstituenten, nicht berücksichtigen, wurden sukzessiver Partikelbruch und die daraus resultierenden Spannungsumlagerungseffekte für zwei Werkstoffe simuliert: Partikelverstärktes Aluminium und Schnellarbeitsstahl. Ergebnisse werden in Form von Vorhersagen des globalen Spannungs-Dehnungs-Verhaltens und der schädigungsrelevanten Felder in der Mikroebene präsentiert, wobei die untersuchten Verbunde Werkstoffe mit hochduktiler bzw. mit einer relativ steifen Matrix repräsentieren. Speziell wird auf den Einfluß der Ma-

terialeigenschaften und der relativen Partikelgrößen auf das vorhergesagte Bruchverhalten eingegangen.

Chapter 1

Introduction

The strong demand for improved engineering materials in the past decades has been a driving force for introducing composite materials. Materials showing improved properties have opened the way for new applications. An important goal has been functionally oriented materials design, which seeks to leverage the growing understanding of the interactions between the constituents of inhomogeneous materials into the development of materials of enhanced user value. In addition, refined modeling capabilities provide a basis for appropriately focussing experimental efforts and reducing the length of development cycles.

In the present work two ductile matrix composites are studied which differ considerably in their mechanical properties. On the one hand, a metal matrix composite consisting of a matrix of AA2618-T4 reinforced by silicon carbide particles is investigated and, on the other hand, the mechanical behavior of a powder metallurgically produced high speed steel is studied.

1.1   Heterogeneous Solids and Structures

Even though they have similar microstructures, hard phase composite materials, based e.g. on iron, and light metal composites, based on e.g. aluminium, both of which show different advantages corresponding to "standard alloys", can be distinguished from the point

of view of their field of application.

Within the former group high wear resistance, high strength and high stiffness are aimed for and these materials are used e.g. in tooling applications. The big advantage of the second group compared to conventional alloys is their low density combined with improved strength and stiffness. These factors make low weight **M**etal **M**atrix **C**omposites (MMCs) an alternative to "classical" materials such as steel and light metal alloys based on aluminium or titanium, depending on the application.

MMCs aim at combining favorable physical and/or chemical properties of the constituents, e.g. ductility and toughness with wear resistance, as well as low density with high strength and stiffness. In contrast to the production routes of standard alloys most MMCs are produced from their constituents by additional processes. Three basic types of the geometry of the reinforcing phases can be distinguished which also require different processes. Whereas continuous fiber reinforced composites are typically produced with liquid-state processes (squeeze or gas pressure infiltration) short fiber reinforced composites nowadays may also be produced, beside mixing in the melt, infiltration and spray deposition, by semi-solid-state (e.g. rheo-casting) and solid-state processes like powder metallurgy (Suresh *et al.* [1993]; Clyne and Withers [1993]). These reinforcement types are not part of the investigations in the present work, where the focus is put on particle reinforced MMCs, produced by one of the above production routes, and on powder metallurgically produced **H**igh **S**peed **S**teels (HSSs). Both are referred to as **P**article **R**einforced **D**uctile **M**atrix **C**omposites (PRDMCs) in the following. It has to be mentioned that throughout this work "reinforcement", "particle" and "inclusion" are used interchangeably.

Depending on the production routes the spatial distribution of the particles (and their sizes) can be controlled to some extent. The materials show homogeneous or inhomogeneous dispersion of the reinforcing phase, the first resulting in isotropic material behavior and the second in anisotropic overall material properties.

For the development of improved PRDMCs a fundamental understanding of the behavior of their constituent materials and their interactions is necessary, which can be achieved by both experimental and theoretical methods. A considerable number of published experimental studies on PRDMCs offer results on the overall material properties, but the measurement of the constituents' mechanical behavior in isolation is very difficult and it is generally hard to deduce the local behavior of these materials from their overall response. Therefore theoretical studies of MMCs at different length scales are an important tool. Within such approaches the behavior at larger length scales can be obtained from that at

smaller length scale by homogenization, while localization methods infer the local behavior at smaller length scales from the conditions at larger scales.

1.1.1   Continuum Mechanical Description of Composites

PRDMC materials consist of several phases. The reinforcement phases, either being ionic, like Al_2O_3, or metallic, like carbides (e.g. M_7C_3), exist as precipitates of the sizes of some nm up to particles of approximate 20μm.

The present study deals with two-phase and three-phase composites at length scales, where the behavior of the constituents can be described within a continuum mechanics framework, the particle diameters being taken to be about 1 to 20μm. Furthermore, the constituents are viewed as continua and for this length scale no "sub-continuum" treatments such as, for example, dislocation mechanics or molecular dynamics are assumed to be required. Following e.g. Böhm [1991] and Plankensteiner [2000] the length scale where the present discussions are carried out will be called the microscale.

This is based on the idea that for materials such as MMCs and HSSs suitable continuum mechanical descriptions can be devised on the basis of two length scales. At the *macroscale*, a length scale comparable to the overall dimensions of specimens or components, smeared out material properties are used, whereas at the *microscale* the inhomogeneity of the material is accounted for, each of the constituents being taken to be homogeneous (the effects of smaller length scales are included via the constituents' material properties). An intermediate scale, the *mesoscale*, may be introduced, when the material shows an appropriate structure, such as layered or clustered particle arrangements.

The overall (effective, homogenized) material properties are evaluated by averaging microscale stress and strain fields of the composite over suitable volumina. The effects of these microfields, which directly depend on the constituent (matrix, reinforcements, interfaces) properties, the loading state and the loading history, as well as on the arrangement of the constituents (the microgeometry), on the macroscopic behavior can be investigated. However, the predictions are limited by necessary modeling idealizations and the difficulty in obtaining reliable constituent material data.

1.1.2   Microstructural Effects

Many PRDMCs are designed to fulfill specific goals, e.g. increasing the wear resistance, optimizing the **C**oefficients of **T**hermal **E**xpansion (CTE) of structural components, pro-

viding thermal conductivity. These properties of the PRDMCs are not the core of investigations within the present study, but the mechanical properties of PRDMCs. Thus, microstructural effects on the mechanical behavior are the topic of this section, where first some considerations on particles and particulates in general are given, followed by aspects specific to the particles of the studied PRDMCs.

The post-yield mechanical properties of composite materials at room temperature are a result of different hardening mechanisms. Finely dispersed (nanometer-sized) precipitates within the base lattice give rise to strain fields in their surroundings and consequently hinder dislocation movements. A moving dislocation, may, on the one hand, cut a particle. On the other hand, the dislocation may be incapable of shearing the particle and may have to pass it, leaving it surrounded by dislocation loops. Such processes which require considerable driving forces, are aimed at in precipitate strengthened alloys. These two competing mechanisms are strongly dependent on the particle size, so that the fine calibration of the particles sizes for optimizing strength must be carried out with appropriate adjustment of heat treatment and heat treatment sequences. Details on this *Orowan*-mechanism and other dislocation mechanisms, generating strengthening dislocation rings (e.g. *Frank-Read*), can be found in the literature, see e.g. Weißmantel and Hamann [1980].
In contrast, the major effect of reinforcement phases with particle sizes discussed in the present work (about 1 to 20μm) on the composites' mechanical behavior is the stiffening effect. It is caused, because these μm-sized particles due to their higher stiffness markedly change the stress and strain fields in the matrix, the reinforcements acting as stress concentrators. Accordingly the interface between matrix and reinforcement plays an important role. In practice perfect bonding between the constituents is not always the case (for alloying additional elements for increasing the wettability may be required), and for a considerable number of MMCs a chemical bonding does not really occur, i.e. the bonding forces can be expected to lie in the region of Van der Waals-forces, see Clyne and Withers [1993]. In the present work perfect bonding is assumed as a first step of idealization.

1.1.3   Microscale Damage Mechanisms

At the length scale of the reinforcements, the microscale, PRDMCs such as particle reinforced MMCs and powder metallurgically produced HSSs, show three basic mechanisms for the initiation and progress of damage, viz. brittle cleavage of the particles, decohesion at the interface between matrix and reinforcements, and ductile failure of the matrix. Under given loading conditions, the relative importance of and the interactions between these

local damage modes (see e.g. the schematic drawing in figure 1), and consequently the overall ductility and damage behavior of the composite, are determined by the strength as well as stiffness properties of all constituents and by their geometrical arrangement.

Ductile matrix failure starts with the nucleation of pores, as a consequence of the local stress and strain states (i.e. triaxiality), and continues with their growth and ongoing coalesce to microcracks, see figures 1 and 2. In general, pore nucleation is more or less temperature dependent and dislocation mobility is the main mechanism for plastic relaxation. Therefore these conditions are strongly influenced by the volume fraction of the reinforcements and their individual sizes and shapes (i.e. corners), compare Goods and Brown [1978]. For example close to elongated reinforcements that are oriented in loading direction, initial pores could be found in experiments. Tests with aluminium reinforced by SiC particles are presented in LLorca *et al.* [1991].

Along interfaces material debonding can occur, caused by weak bonding or by advanced plastic deformation, especially at reinforcement corners or at elongated particles (reinforcements) oriented in loading direction, see figure 3. The interface strength is highly dependent on the chemical bonding of the phases, therefore influenced by diffusion processes and consequently by temperature; investigations and results are described e.g. in Flom and Arsenault [1986]; Lee and Subramanian [1992].

Reinforcement failure takes place when some critical stress within the particle is exceeded (figure 4). Upon increasing the plastic deformation of the embedding matrix frequently an increased number of failed particles can be observed; experimentally it has been shown that in tensile tests the reinforcing particles tend to fail predominantly perpendicularly to the overall loading direction. Beside that the size and shape (rod shaped, platelike, equiaxed) of the particles and also the yield strength of the matrix and therefore temperature play important roles in the failure behavior (Wallin *et al.* [1987]).

For illustrating the complexity of the problem one may refer to figure 5 (from Gross-Weege [1996]). Evidently after failure of a particle the microcrack may propagate either into the matrix or along the interface. The modeling strategies used in the present study are aimed at studying microscale damage due to particle fracture in isolation, the idea being to open an avenue for a better understanding of the factors involved by reducing the complexity of the problem (see chapter 3).

1.1.4 Models and Descriptions for Nonlinear Heterogeneous Solids

Modeling work on the stiffness and strength behavior of PRDMCs has been largely based on continuum micromechanics, where the stresses and strains acting within the material are resolved at length scales comparable to the size of the particles. Within this framework a considerable number of micromechanically based modeling studies have been reported on the initiation and evolution of microscale damage and failure in PRDMCs, in which analytical (Tohgo and Weng [1994]), numerical (Pandorf [2000]) as well as combined approaches (Estevez *et al.* [1999]; LLorca and González [1998]) were employed. Unit cell models, in which the local stress and strain fields can be resolved to a high degree, have covered all of the above damage modes for planar and axisymmetric model geometries, see e.g. Berns *et al.* [1998]; Ghosh and Moorthy [1998]; Nutt and Needleman [1987], and for simple periodic arrays of particles (Hom and McMeeking [1991]). Recent work (Iung and Grange [1995]; Böhm and Han [2001]), however, has shown that two-dimensional models tend to give unsatisfactory predictions for the mechanical response of particle reinforced materials. Plane stress models generally underestimate and plane strain as well as generalized plane strain models overestimate the overall elastic and elastoplastic stiffness of such materials. Compared to three-dimensional unit cells, both groups of planar models have been shown to give rise to considerably different phase averages of the microscale stresses and strains and underestimate the widths of their distributions (Böhm and Han [2001]). As a consequence, two dimensional models may not give reliable predictions for damage relevant variables. For example the Weibull fracture probabilities of the particles were found to be markedly underestimated by two-dimensional unit cells at a given reinforcement volume fraction (Han *et al.* [2001a]). Axisymmetric cell descriptions fare better in this respect, but by design can handle only highly regular microgeometries, so that local "hot spots" caused by irregular particle spacing can hardly be investigated. Accordingly, it is of considerable interest to study the initiation and progress of microscale damage in PRDMCs by three-dimensional unit cells that involve a number of particles in irregular arrangements.

Experiments have shown that in a number of PRDMC systems, among them AA2618-T4 reinforced by SiC particulates (LLorca and González [1998]) and HSS (Mishnaevsky *et al.* [2001]), brittle cleavage of the particles tends to be the primary microscale mechanism for initiating damage (This behavior, however, is by no means universal. Among the wide range of PRDMCs produced and studied, essentially any combination of critical damage modes can be found). Cracks in such materials have been found to be preferentially oriented normally to the applied uniaxial tensile loading direction (Mawsouf [2000]) and, depending

on particle shape and size, to often run through the inclusions' centers (Wallin *et al.* [1987]; Pandorf [2000]).

The study presented in the following was planned as a major step towards modeling a damage mechanism of this type in PRDMCs via three-dimensional multi-particle unit cells. Due to the complexity of the problem and to minimize interaction effects between the damage mechanisms it was focussed on the brittle failure of reinforcements in ductile matrix composites reinforced by stiff spherical particles. This choice of spherical particles is quite realistic for powder metallurgically produced HSS, but is more of an idealization for MMCs in which SiC particles reinforce an aluminium matrix. The present modeling strategy differs considerably from the published literature (Pandorf [2000]; Broeckmann [2001]), where two-dimensional models were used but all of the above mentioned damage mechanisms were modeled.

1.2   Particle Reinforced Composite AA2618/SiC$_p$-T4

Lightweight MMCs based on commonly used matrix materials such as aluminium can be produced economically with liquid-state processes. In order to approach homogeneous particle distributions well controlled stiring is necessary. However, the production route is limited to lower particle volume fractions and the problems of particle wetting and of the trends towards segregating of the commonly used SiC and Al$_2$O$_3$ particulates are persisting. For increasing the reinforcement volume fraction rheo-casting is used. Spray deposition methods are alternatively employed for higher volume fractions, the melt being spray nozzled under the use of nitrogen and deposited together with the ceramic particles, which are blown into the spray zone. However, these methods have limitations in the geometrical shapes that can be attained.
Arbitrary reinforcement volume fractions are possible with powder metallurgical processes, which also offer very homogeneous reinforcement distributions. Consolidation is done via vacuum hot pressing or **H**ot **I**sostatic **P**ressing (HIP) processes or extrusion, which make this method quite expensive.

For the present studies an MMC has been specifically chosen, which is known to have particle failure as a dominant damage mechanism and the required component material properties of which are reasonably well known. In LLorca and González [1998] AA2618/SiC$_p$-T4 is described as an MMC with such a behavior, the particle sizes ranging from 5 to 20μm. The chemical composition of the matrix material used, AA2618-T4,

is given in table 1. For the mechanical properties for both the matrix AA2618-T4 and the reinforcing material SiC used in the simulations refer to table 3. Note, that the SiC particulates are treated as isotropic (and thus not as monocrystalline), that the elasto-plastic behavior of the AA2618-T4 matrix is taken to include all effects of the submicron microstructure of the alloy (e.g. precipitate hardening effects) and that the grain structure of the matrix is not accounted for explicitly.

1.3   High Speed Steel

Due to its high working hardness, wear resistance and its toughness HSS is the most widely used material for tools in machining processes such as shaping and forming, extrusion and punching. The usually high content of metallic carbides makes HSS capable for applications up to the temperature range of 550–600ºC. For attaining specific properties careful adjustment of alloying elements is a precondition. In contrast to proper MMCs, the carbides are formed in HSS according to thermodynamics and kinetics, but the resulting microstructure clearly can be treated as a PRDMC.

Most of the world production of HSS still relies on electro slag remelting technology. This process typically gives an inhomogeneous distribution of hard carbidic particles in the material of the size of micrometers, the primary carbides. Nanometer-sized carbides, referred to as secondary carbides, are more or less homogeneously distributed throughout the matrix phase. Alternatively the more expensive **P**owder **M**etallurgical (PM) routes allow a "larger window of opportunity" in controlling the arrangements of the primary carbides and have become more and more important in tool design.

However, even though HSS has been widely used for a long time, the influence of the complex morphology of such heterogeneous materials on the effective material properties and on their failure behavior is yet not well understood. The present work is intended to be a step towards obtaining additional insight into the damage and failure behavior of HSS. It is mainly focused on HSSs produced by PM routes. Throughout the present study primary carbides will be referred as "carbides", their material being chosen to represent either of two groups of "mixed metallic carbides". The matrix is treated as homogeneous isotropic elastoplastic material, the secondary carbides and other inhomogeneity effects (martensite-austenite topology) being smeared out and accounted for in the material parameters. An example of the chemical composition of a typical HSS produced by PM is given in table 2, the constituent material properties used in this work for modeling the mechanical behavior are listed in table 4.

Chapter 2

Modeling Damage in PRDMCs on the Microscale

As is well known from everyday experience the failure behavior of brittle materials differs strongly from typical ductile failure behavior. In principle it could be said, that catastrophic failure at widely varying stress levels takes place.

In general, failure, and in the special case failure of brittle materials, is attributed to always present inhomogeneities within the material. "Inhomogeneity" is characteristic for all real materials at atomic, micro-, meso- and macroscale. At the macroscopic level the random inhomogeneity is evident in the random variations of macroscopic properties, such as hardness, deformation or strength properties. At the smaller scales the random inhomogeneity refers to size, orientation, topology, physical properties of the materials' constituents and at the submicroscopic level, it takes the form of geometrical defects in the almost perfect structure, vacancies, precipitates, grain boundaries, and dislocations. The present study corresponds to conditions at the microscale. Simulation allow idealizations to be introduced, where e.g. inhomogeneities at lower length scales are smeared out and each of the constituents, matrix and reinforcement, can be assumed to be homogeneous and isotropic. This results in a reduction of degrees of freedom within the models to be considered. Furthermore, the simulation methods used in the present work offer a tool for studying the microscale damage modes of inhomogeneous materials in isolation, which opens an avenue for a better understanding of the factors involved by reducing the complexity of the problem. The focus has been put on the brittle failure of particulate reinforcements.

First, this chapter tries to give a survey of models proposed in the literature for the brittle fracture of bulk ceramics. Then the method chosen for the description of the failure of brittle particles in a ductile matrix is explained. For completeness useful damage relevant parameters for describing damage in the matrix and failure in the interface are also introduced.

2.1 Fracture of Brittle Reinforcements

Fracture processes that are neither preceded nor accompanied by inelastic, especially plastic, deformation, because the material does not possess any mechanism by which significant amounts of strain energy can be dissipated (e.g. slip mechanisms, or existing mechanisms are blocked because of environmental conditions such as temperature), are designated as "brittle fracture": the whole applied energy is reversibly stored and can be dissipated only by the formation of new (fracture) surfaces (Freudenthal [1965]).

With the survey of experimental results given in Wallin *et al.* [1987] the main aspects of brittle particle failure in PRDMCs relevant to the present work are:

- On the average larger particles fail preferentially compared to smaller ones.

- The crack orientation in particles tends to be perpendicular to the direction of the maximum tensile stress.

- Experiments show that the ultimate strength of PRDMCs under tensile loading shows a considerable statistical scatter.

From these findings it is clear, that a failure description similar to brittle bulk ceramics may be suitable.

The experimental fact that experiments on uniformly sized samples of brittle ceramics subjected to equal tensile loads show a wide statistical scatter, was the basis for the statistical probability model published by Weibull [1939] which is well established in the literature for describing the failure probabilities of brittle materials. This idea has been extended into Weibull probability models for describing the brittle failure of reinforcements in composite materials, which have seen fairly wide use (Wallin *et al.* [1987]; Bréchet *et al.* [1991]; LLorca *et al.* [1993]; Lewis and Withers [1995]), the main alternative being critical

particle stress criteria, see e.g. (Li and Ellyin [1998]). Weibull fracture probabilities have been used in this framework both in the form of Rankine-type criteria and in combination with Monte-Carlo algorithms, see e.g. Pandorf [2000].

The modeling of the generation or growth of cracks proper (i.e. the generation of new free surface) in numerical methods like the **F**inite **E**lement **M**ethod (FEM), has been realized via cohesive zone models (Finot *et al.* [1994]; Steglich [1999]), instantaneous opening by node release (Broeckmann [1996]; Pandorf [2000]) or by the instantaneous introduction of an elliptical crack (Ghosh and Moorthy [1998]). Within special FE formulations the first approach uses so called cohesive elements, which link the nodes lying at predefined crack planes and which lose their stiffness under appropriate loading and deformation conditions (such elements are also frequently used for modeling interfacial debonding). This behavior is typically controlled by a cohesive potential, which links local tractions and displacements while prescribing the appropriate energy of fracture. Within the second method crack planes open after some fracture criterion is fulfilled (e.g. controlled by Weibull fracture probabilities) either by node release, in which case "double nodes" must be provided along predefined crack planes, or by fully remeshing the FE mesh. In the third method, special elements are used which provide for the presence of particles within each element, each particle, in turn, having the capability of forming an elliptical crack. This has been achieved within the extended **V**oronoi **C**ell **F**inite **E**lement **M**ethod (VCFEM, Ghosh and Moorthy [1998]) essentially by embedding appropriate analytical solutions via enriched hybrid shape functions. Note that whereas cohesive zone models are capable of modeling the progress of a crack, in the other two models crack opening is instantaneous, which makes them suitable for the use in combination with Weibull-type probabilistic models.

In the present study a Weibull based node release technique at predefined fracture surfaces is used. In the following the Weibull model is discussed in general, i.e. the basic application to bulk ceramics is introduced and considerations on uniaxial and multiaxial loading conditions for brittle materials are given. Finally the Weibull model is applied to the description of the brittle failure of reinforcements, and, to come to the core of the present work, to the brittle particle fracture in PRDMCs.

2.1.1 General

A statistically relevant number of test results of nominally identical brittle specimens under nominally identical loading conditions typically give strengths that differ widely around the mean values, obtained by simple Gauß type statistics, and for material evaluation and

material design the significance of such average values is rather doubtful. Experiments have shown that the scatter of test results has to be considered as a part of the physical process of brittle fracture. A single "tensile strength" cannot be given, but there is a certain definable probability that a given sample will have a given strength.

A first general consideration of experiments on brittle materials typically shows, that the average tensile stress of fracture is smaller than the average bending fracture stress, i.e.

$$\bar{\sigma}_{\text{fr,tensile}} < \bar{\sigma}_{\text{fr,bending}} \tag{2.1}$$

can be observed. The reason for this behavior obviously is the different stress distributions inside the specimen. In bending tests of brittle specimens the part of the cross section which is exposed to compressive stresses must not be regarded in the discussion of fracture behavior (Ashby and Jones [1986]; Green [1998]) and only flaws lying in the tensile loaded section of the specimen can become critical. Thus, compressive stresses can be safely assumed to have no influence on the risk of rupture and the specimen will survive higher stresses under bending.

A second important result of experiments, a typical volume dependence of the failure of brittle materials, shows that larger specimens of the same material fail at lower stresses than small ones, on the average. One must assume, that this is a consequence of the inner structure of the material. A higher likelihood of defects, namely in larger samples, results in a higher probability of failure at the same applied load. Or, in other words, the brittle fracture of a material under a state of (tensile) stress is related to its defect structure, i.e. to the concentration and severity of defects in the specimen and the likelihood of the existence of a critical crack is greater in large specimens than in small ones.

These findings were first combined into a reliability model by Weibull [1939]. The statistical considerations lead to a size effect on brittle fracture strength in the meaning of having either a certain number or a certain severity of flaws for causing fracture; the likelihood of the occurrence of failure is dependent on the statistical expectation of the critical conditions in the sample and it is directly related to the specimen's size. Failure of many brittle materials initiates at micro cracks that reach or exceed a certain effective critical length, and naturally depends on their bias compared to the local stress state. Furthermore the flaw distribution in bulk ceramics individually differs from specimen to specimen, for typical distributions of microdefects $g(a)$ see figure 8. Thus, as mentioned above, the failure of brittle materials cannot be satisfactorily described by deterministic

methods and the statistical description has to be used.

In the following, first a group of methods for describing the failure of brittle materials in general will be discussed and then their applications to the brittle failure of particles embedded in a ductile matrix will be focussed on.

2.1.2   Uniaxial Stress State

Weibull [1939] showed, that for uniaxially loaded specimens of elastic brittle materials the probability of failure P_{fr} is simply related to the applied (tensile) stress σ and the specimen volume V by

$$P_{\mathrm{fr}} = 1 - \exp(-n(\sigma) \cdot V) \quad , \tag{2.2}$$

where $n(\sigma)$ is called the "density of risk of fracture". Defects and inhomogeneities are assumed not to influence each other, they are independent; therefore probabilities of interrelated parts of a discussed structure can be multiplied. The fracture probability of the whole sample can be obtained by the use of the **W**eakest **L**ink **T**heory (WLT) (the probability of the nonfailure of e.g. a chain is equal to the simultaneous probability of nonfailure of all of the links):

$$P_{\mathrm{s}} = (1 - P_{\mathrm{fr}}) = \prod_{j=1}^{k} P_{\mathrm{s},j} \tag{2.3}$$

The probability of survival P_{s} of a given specimen of volume V is the result of the independent probabilities of survival $P_{\mathrm{s},j}$ of the k considered and relevant volume elements.

Weibull [1939, 1951] related the density of risk of fracture (the logarithmized survival probability) to the actual stress acting on the body in the following way, based on empirical observations:

$$n(\sigma) := -\ln(1 - P_{\mathrm{fr}}) = \frac{1}{V_0} \left(\frac{\sigma - \sigma'_u}{\sigma'_0} \right)^{m'} \quad . \tag{2.4}$$

Here V_0 represents an arbitrary scaling parameter (reference volume), σ'_u a lower limit of strength, where $P_{\mathrm{fr}}(\sigma \leq \sigma'_u) = 0$, and σ'_0 and m' are material parameters, respectively, compare Weibull [1951]; Wallin *et al.* [1987]; Margetson and Cooper [1984]. The frequently used two-parameter relations set the threshold stress $\sigma'_u = 0$ and lead to the well known relation for the fracture probability for a specimen

$$P_{\text{fr}} = 1 - P_{\text{s}} = 1 - \exp\left\{ -\frac{V}{V_0} \left(\frac{\sigma}{\sigma_0} \right)^m \right\} \quad , \tag{2.5}$$

where m is known as the Weibull modulus. The characteristic strength σ_0 is defined such that for a specimen of volume $V = V_0$ the probability of fracture is

$$P_{\text{fr}} = 1 - \exp\left\{ -\left(\frac{\sigma}{\sigma_0} \right)^m \right\} = 1 - \exp\left\{ -1 \right\} = 0.632 \quad , \tag{2.6}$$

i.e. where the density of risk of fracture $n(\sigma) = 1$. For a given material, the characteristic strength σ_0, the normalizing parameter V_0 and the Weibull modulus m are taken to be material constants and consequently

$$V_0 \sigma_0^m = \text{const.} \tag{2.7}$$

For a homogeneous stress state σ_0 and V_0 determine the position of the curve $P_{\text{fr}}(\sigma)$ since $P_{\text{fr}}(\sigma_0) = 0.632$ at $\sigma = \sigma_0$ and $V = V_0$. The slope of $P_{\text{fr}}(\sigma)$ is given by the Weibull modulus m. The typical volume dependence of a Weibull distribution as function of the applied (homogeneous) stress state is schematically presented in figure 6: different specimen volumes of the same material have the same fracture probability at different stress levels. More detailed mathematical considerations of the Weibull distribution are given in appendix B.

Following Danzer [1992] the density of risk of fracture $n(\sigma)$ can be associated with the average number of critical defects $\langle N_{\text{c},V} \rangle$ within the specimen (averaged over a number of specimens),

$$\langle N_{\text{c},V} \rangle = n(\sigma) \cdot V \quad , \tag{2.8}$$

from which the influence of the specimen dimensions becomes obvious. A larger specimen of the same material (the interpretation of $n(\sigma)$ is discussed in more detail in the following section) means a higher average number of critical defects $\langle N_{\text{c},V} \rangle$, and leads, together with eqn. (2.2), to a higher probability of failure.

The shapes of Weibull distribution functions for different m are schematically drawn in figure 7. Perfectly predictable materials are characterized by $m \to \infty$, resulting in a step function $P_{\text{fr}}(\sigma)$ with σ_0 representing a discrete strength value.

In the next subsection a physical interpretation of the Weibull fracture distribution function, eqn. (2.5), is introduced, in the case of limitation to uniaxial tensile stress states.

Defect Density and Strength Distribution:

In order to link Weibull fracture probabilities with defect densities in a sample, one can assume that all critical cracks are oriented perpendicularly to the loading orientation and, for simplicity, that the failure criterion is of "Griffith"-type, who originally considered the strain energy change of an infinite plate of elastic material with a central elliptical flaw loaded under uniform tension and under plane strain conditions (more complex criteria are possible, but not necessary for the basic message). Hence failure occurs, when the stress intensity factor K of at least one flaw exceeds the fracture toughness related to mode I loading, $K_{\mathrm{I,c}}$, i.e. (see Freudenthal [1965] and Danzer *et al.* [1992])

$$K = \sigma Y \sqrt{a} \geq K_{\mathrm{I,c}} \quad . \tag{2.9}$$

Here σ is the applied stress multiplied by Y (a geometry factor) and the length of the flaw is a. The critical crack length $a_{\mathrm{c}}(\sigma)$ therefore is given by the critical value $K_{\mathrm{I,c}}$, Y and σ and all cracks of length $a \geq a_{\mathrm{c}}(\sigma)$ are supposed to lead to specimen failure

$$a \geq a_{\mathrm{c}}(\sigma) = \left(\frac{K_{\mathrm{I,c}}}{\sigma Y} \right)^{2} \quad . \tag{2.10}$$

The density of critical flaws of sizes $a \geq a_{\mathrm{c}}(\sigma)$ for a given stress σ and hence the probability of fracture per volume unit then is

$$n(\sigma) = \int_{a_{\mathrm{c}}(\sigma)}^{\infty} g(a) da \quad , \tag{2.11}$$

where the size distribution of the microdefects distribution function $g(a)$ (compare figure 8) may be approximated by an inverse power law $h(a)$ for explicit evaluation, compare Danzer *et al.* [1992]:

$$h(a) = h_0 \left(\frac{a}{a_0} \right)^{-\rho} \quad . \tag{2.12}$$

The proportionality factor $h_0/a_0^{-\rho}$ is given by metallographically obtained material parameters h_0, ρ and the scaling length a_0 (flaws are assumed to be small in relation to the specimen dimensions). The relation between eqn. (2.12) and the Weibull parameters can be obtained by inserting eqn. (2.12) into eqn. (2.11). With the use of eqn. (2.10) one obtains

$$n(\sigma) = \frac{a_0 h_0}{\rho - 1} \left(\frac{\sqrt{a_0 \pi}\, \sigma Y}{K_{\mathrm{I,c}}} \right)^{2(\rho - 1)} \tag{2.13}$$

and comparison with eqns. (2.2) and (2.5) leads to

$$m = 2 \cdot (\rho - 1) \tag{2.14}$$

and

$$\sigma_0 = \left(\frac{\rho - 1}{h_0 a_0 V_0} \right)^{\frac{\rho - 1}{2}} \cdot \frac{K_{\mathrm{I,c}}}{Y \sqrt{a_0}} \qquad . \tag{2.15}$$

(see also Lewis and Withers [1995] and Mura [1987]).

Strictly speaking these considerations are valid only for homogeneous crack distributions within the discussed specimen. For inhomogeneous defect distributions the density of cracks, $h(a)$, and the density of critical defects, $n(\sigma)$, are position dependent, i.e. $h_0(a) \to h(a, \underline{r})$, $\rho \to \rho(\underline{r})$ (Sutherland *et al.* [1999]). However, locally the Weibull fracture probability distribution can be expected to hold true. Another type of position dependence can result from inhomogeneous stress distributions, so that $a_{\mathrm{c}}(\sigma) \to a_{\mathrm{c}}(\sigma(\underline{r}))$ in eqn. (2.10). Under such conditions eqn. (2.5) becomes:

$$P_{\mathrm{fr}} = 1 - \exp \left\{ -\frac{1}{V_0} \int_V \left(\frac{\sigma(\underline{r})}{\sigma_0} \right)^m dV \right\} \qquad . \tag{2.16}$$

Whereas eqn. (2.14) is true even for multiaxial stress states and other crack orientations, eqn. (2.15) changes. Eqn. (2.16) requires additional discussion, considering that an arbitrary oriented crack under a uniaxial stress state in general is loaded multi-modally. The linkage between fracture mechanics and Weibull fracture probabilities and the treatment of other damage modes (mode II and mode III), are considered e.g. in Thiemeier [1987] and Heger [1993].

2.1.3 Treatments of Multiaxial Stress States in the Literature

For generalizing the concept of the WLT for considering multiaxial stress states the following methods have been proposed in the literature:

- Mapping the stress tensor onto an equivalent stress, e.g. using the normal stress component acting on a given plane, and, after exponentiating by the Weibull parameter m, averaging over all plane orientations for forming the density of risk of fracture. This idea goes back to Weibull [1939].

- In a number of publications the Weibull fracture probabilities of multiaxially loaded bodies are based on the so called **P**rinciple of **I**ndependent **A**ction (PIA) of the principal stresses, see e.g. Freudenthal [1965]. Within this assumption the probability of survival for each of the principal stresses are evaluated using the original model and their combination by multiplication results in the probability of survival of the specimen, see e.g. Margetson and Cooper [1984]; Stanley *et al.* [1973]; R'Mili *et al.* [1996].
  For anisotropic materials such as fiber composites this implies a description based on lengths instead of volumes, where the Weibull parameters m_l, m_b and m_d are not necessarily equal (Sutherland *et al.* [1999]) and for two specimens A and B instead of eqn. (2.7) the following relationships hold for length, breadth and depth

$$\frac{\sigma_B}{\sigma_A} = \left(\frac{l_A}{l_B}\right)^{\frac{1}{m_l}} \qquad \frac{\sigma_B}{\sigma_A} = \left(\frac{b_A}{b_B}\right)^{\frac{1}{m_b}} \qquad \frac{\sigma_B}{\sigma_A} = \left(\frac{d_A}{d_B}\right)^{\frac{1}{m_d}} \quad . \qquad (2.17)$$

  Similarly, a so called "Noninteractive Macroscopic Reliability Model" based on the PIA assumption interprets the risk of fracture as a function only dependent on a set of invariants that correspond to the physical mechanisms related to fracture of the individual problem, and are "constructed" out of the stress tensor and an orientation unit vector (Duffy and Arnold [1990]).

  Experiments have shown, however, that with the PIA under certain conditions underestimation of multiaxiality influences can result (Batdorf and Crose [1974]).

- More complex methods treat the failure mechanism on the basis of fracture mechanics. Defects are assumed to be plane cracks subjected to certain stress levels depending on orientation and stress state and this results in an influence of the stress state on the failure probability.

2.1.4 Modeling Brittle Particle Failure in Heterogeneous Materials

The General Model

For the present work an approach based on the third of the above groups of methods is used:

In analogy to Thiemeier [1987] an equivalent stress $\sigma_{\mathrm{I,eq}}$ which accounts for considering only mode I loading of a crack oriented by angles θ and φ (see figure 9) has to be found out of the local stress tensor

$$\sigma_{\mathrm{I,eq}} = \sigma_{\mathrm{I,eq}}(\sigma_1(x,y,z), \sigma_2(x,y,z), \sigma_3(x,y,z), \varphi, \theta)$$

$$\Rightarrow \sigma_{\mathrm{I,eq}} = \sigma_{\mathrm{I,eq}}(x,y,z,\varphi,\theta) \tag{2.18}$$

on the basis of some appropriate fracture criterion. With the knowledge of the orientation of the normal of a given crack to the local principal axes of the stress tensor and a criterion for the multiaxiality in terms of an equivalent stress $\sigma_{\mathrm{I,eq}}$, the fracture probability then follows as:

$$P_{\mathrm{fr}} = 1 - \exp\left[-\frac{1}{V_0}\int_V \frac{1}{2\pi}\int_{\varphi=0}^{\pi}\int_{\theta=0}^{\pi}\left(\frac{\sigma_{\mathrm{I,eq}}(x,y,z,\varphi,\theta)}{\sigma_{0,I}}\right)^m \sin\theta \; d\theta \; d\varphi \; dV\right] \quad , \tag{2.19}$$

compare Thiemeier [1987], with the characteristic strength to mode I loading, $\sigma_{0,I}$.

An approach similar to eqn. (2.19) was developed by Gyekenyesi and Nemeth [1987] and Hunt and McCartney [1979], the latter additionally considered different types of defects having different fracture criteria. In appendix A some expressions for equivalent stresses for evaluating Weibull-type fracture probabilities are given.

In the next section the assumptions for the fracture criterion used in the present work are listed.

FE Model for Particle Cleavage in PRDMCs

In the present work, ductile matrices reinforced by spherical particles are considered. This particle shape avoids crack initiation at surface features of the particles such as notches,

which may act as local stress concentrators in more general particle shapes. Also, for geometrical reasons, multiple cracks in a particle are not very probable. Accordingly, particle cleavage along planar fracture surfaces running through the particle centers is a reasonable assumption. Because experimental work has shown that the crack orientations correlate strongly with the direction of the overall maximum principal stress, the assumption can also be made that crack planes (provided by the FE-mesh of the particle) are oriented normally to the direction of the overall principal stress.

A node release algorithm was chosen to model the actual opening up of the crack (see chapter 3), which is activated by Weibull-type fracture probabilities. For evaluating the fracture probabilities within each particle j the following simple extension was chosen. For the calculation of the equivalent stress $\sigma_{\mathrm{I,eq}}$, relevant for evaluating the particle fracture probability, the stress tensor for each integration point is analyzed. As a consequence of assuming mode I failure of the particles the maximum principal stresses can be used for the equivalent stresses $\sigma_{\mathrm{I,eq}}$, only one crack plane, oriented perpendicularly to the global loading direction being regarded:

$$\sigma_{\mathrm{I,eq}} = \sigma_1 \quad \text{and} \quad \sigma_0 = \sigma_{0,I} \tag{2.20}$$

The resulting relation for the fracture probability of particle j as used in the present work is, rewriting eqn. (2.19):

$$P_{\mathrm{fr},j} = 1 - \exp\left\{ -\frac{1}{V_{0,j}} \int_{V_j : \sigma_1(\underline{r}) > 0} \left(\frac{\sigma_1(\underline{r})}{\sigma_{0,j}} \right)^{m_j} dV \right\}. \tag{2.21}$$

With the material characteristic Weibull modulus of the particle, m_j, the first maximum principal stress distribution within the particle, $\sigma_1(\underline{r})$, related to a characteristic material strength, $\sigma_{0,j}$, integrated over the particle volume V_j and normalized by the reference volume $V_{0,j}$, the Weibull fracture probability is determined. The WLT assumption, integrated into Weibull models by definition, considers, on the one hand, that the probability of fracture increases when the particle size increases and, second, increases when stresses acting on the particle increases.

Numerical experiments showed that for the conditions studied, i.e. loading by uniaxial tension of a PRDMC with randomly positioned spherical particles, eqn. (2.21) gives very similar results to the more complex expressions listed in appendix A.2, compare also appendix A.3.

Details of the implementation are discussed in chapter 3.

2.2 Matrix Failure

Methods for describing the evolution of ductile damage in metallic matrices are the topic of this section. Two main approaches have been used in the published literature for the description and modeling of matrix failure. First, the previously mentioned cohesive zone models have been used by a number of authors, especially in cases where the position of the crack is known beforehand from symmetry considerations (Finot *et al.* [1994]).
Second, damage type models have been used, in which the initiation and evolution of spatially distributed damage is followed, the effects of which may be accounted for by a gradual reduction of local stiffness or by element elimination techniques. A well known group of descriptions of this type are Gurson models (Gurson [1977] and Tvergaard [1982]; Tvergaard and Needleman [1984]), which describe ductile damage in metals via yield functions that depend on the void volume fraction. In their fully developed form they contain an evolution law that covers void nucleation, growth and coalescence.

A common drawback of damage type models that give rise to local stiffness reductions is their marked mesh dependence. This difficulty can be resolved by regularizing the models by invoking higher order or nonlocal continuum theories or by carrying out time dependent analyses with some dissipation.

Ductile matrix damage is not a primary topic of the present study and, accordingly, no analyses involving stiffness reduction due to matrix damage were carried out. Where appropriate, assessments of the vulnerability of the matrix to ductile matrix damage were made, however, by evaluating a ductile damage indicator (Fischer *et al.* [1995]), which may also be considered as belonging to the damage type family of models. This damage indicator was developed by Gunawardena *et al.* [1991] on the basis of work by Rice and Tracey [1969] as well as Hancock and Mackenzie [1976]. It uses a reference failure strain

$$\varepsilon_{\mathrm{f}} = 1.65\ \varepsilon_0\ \exp\left(-\frac{3}{2}\ \eta\right) \quad \text{with} \quad \eta = \frac{\sigma_{\mathrm{H}}}{\sigma_{\mathrm{eq}}} \quad , \tag{2.22}$$

where the stress triaxiality ratio η, given by the relation of the hydrostatic stress $\sigma_{\mathrm{H}} = \frac{1}{3}\sigma_{kk}$ divided by the Mises equivalent stress, σ_{eq}, influences the initiation and growth of ductile matrix damage. The failure strain ε_{f} relates the fracture strain in the uniaxial case, ε_0, to the general triaxial case. That is, for

$$\sigma_1 \neq 0, \ \sigma_2 = \sigma_3 = 0 \tag{2.23}$$

the triaxiality becomes $\eta = \frac{1}{3}$ and

$$-\frac{3}{2}\frac{\sigma_{\mathrm{H}}}{\sigma_{\mathrm{eq}}} = -\frac{1}{2} \implies \exp\left(-\frac{1}{2}\right) = \frac{1}{1.65} \quad . \tag{2.24}$$

The differential damage indicator then is defined as the increment of the accumulated plastic strain related to the reference failure strain, eqn. (2.22):

$$dD_{\mathrm{i}} = \frac{d\varepsilon_{\mathrm{eq,p}}}{\varepsilon_{\mathrm{f}}} \quad . \tag{2.25}$$

By inserting eqn. (2.22) into this relation one obtains

$$dD_{\mathrm{i}} = \frac{1}{1.65\ \varepsilon_0} \exp\left(\frac{3}{2}\eta\right) d\varepsilon_{\mathrm{eq,p}} \quad . \tag{2.26}$$

Provided the evolution of both $\varepsilon_{\mathrm{eq,p}}$ and η are known over the full deformation history, the above expression can be integrated, leading to the following ductile damage indicator:

$$D_{\mathrm{i}} = \frac{1}{1.65\ \varepsilon_0} \int_0^{\varepsilon_{\mathrm{eq,p}}} \exp\left(\frac{3}{2}\eta\right) d\varepsilon_{\mathrm{eq,p}} \quad . \tag{2.27}$$

Within numerical engineering methods the local stress (and thus η) as well as the plastic strains are available at each integration point at each increment, so that an approximate evaluation of eqn. (2.27) e.g. by the trapeze rule is rather straightforward. At $D_{\mathrm{i}} = 1$ the material locally has "used up its ductility" and ductile failure must be expected. For other values of D_{i} (except, of course, the trivial value of $D_{\mathrm{i}} = 0$), however, a physical interpretation of D_{i} is not possible.

A major strength of the concept of the ductile damage indicator is the fact that only one material parameter, ε_0, is required, which can be obtained from uniaxial tests (Fischer *et al.* [1995]). Ductile damage indicators can be combined with element elimination algorithms which are activated upon reaching $D_{\mathrm{i}} = 1$ to actually model the progress of ductile cracks, see e.g. Mishnaevsky *et al.* [1999]. Note that in the present studies an uncoupled method is used (the damage indicator does not influence the elastoplastic analysis) and a damage free structure is investigated in the stress analysis. In the present study the damage indicator concept has been used only for an estimation of possible damage within the matrix in addition to the particle fracture.

2.3   Interfacial Debonding

Interfacial failure at phase boundaries can have a significant influence on the deformation properties of PRDMCs. First approaches for modeling interfacial failure were based on energy-balance evaluations similar to Eshelby models (Goods and Brown [1978]). The energy released by interfacial decohesion must be higher than the energy required for creating new surface. This is a necessary but not a sufficient condition for interfacial decohesion. Additionally a critical interface strength has to be exceeded.

Therefore models based on stress-strain criteria have been developed, e.g. by Nutt and Needleman [1987], for quantitative description of pore growth at reinforcement ends, where the continuum mechanics based approach of a cohesive zone model, suggested by Needleman [1987], enables activation of different damage modes:

- Exceeding a critical normal stress leads to decohesion normal to loading direction, in the sense of mode I failure. Cyclic loading would make crack closure possible.

- Sliding along the interface, mode II failure, occurs after exceeding a critical shear stress.

- Mixed mode failure, superimposing both modes can occur, as a consequence of multiaxial loading of the interface.

Evaluation of interfacial decohesion via FE-methods and on the basis of the cohesive zone model can be realized either by interface elements (Needleman [1990]; Steglich [1999]), setting the element stiffness to zero after exceeding the critical value, or by node release techniques, introducing interface failure at appropriate positions of the modeled interface (Gross-Weege [1996]).

   In the present work the interface conditions after applying mechanical loads and possible particle failure are only analyzed on the basis of the evaluated magnitudes of the interfacial tractions. It should be noted, however, that within the implemented user subroutines interfacial decohesion could be realized. For a detailed description refer to appendix C.

Chapter 3

The Unit Cell Model

With the present levels of computational power particle reinforced materials can be routinely modeled by three dimensional periodic arrangements of particles using unit cells that contain a limited number of particles. For the description unit cells have to be created, which ideally should correspond to representative volume elements (Hashin [1983]; Markov [2000]) that fully describe the statistics of the microstructure.

Within the unit cell the position distribution of the inclusions can be either regular and/or more or less symmetric/oriented (for different particle shapes). Simple but regular structures can be treated by special unit cell design or by axisymmetric models. Random arrangements of inclusions offer more general microgeometries and foundations for more general studies of MMCs; they are used within this work. Nevertheless, the periodic arrangement of the unit cells itself prevents them from fully describing statistically homogeneous microgeometries.

Within this chapter the unit cell models used are introduced: The techniques for generating particle arrangements are explained and a method for a geometrical characterization of the unit cells is discussed. The realization of the Finite Element model and the preparation of the input data for the Finite Element code are presented, including a description of subroutines required for implementing particle failure.

3.1 Multi Inclusion Unit Cells

The principal aim of the present work consists in using unit cell models for studying the mechanical behavior of PRDMCs subjected to multiple sequential particle fracture, the failure events being triggered by the stress states of the individual particles. Implicit with this task is the need for unit cells that contain a number of particles that may either form "simple periodic" arrays (such as **s**imple **c**ubic (sc), **b**ody **c**entered **c**ubic (bcc) or **f**ace **c**entered **c**ubic (fcc) microgeometries) or may be positioned in some random manner that aims at approximating the statistically homogeneous arrangements of particles found in most particle reinforced composites. While the former type of model microgeometry may pose slightly lower computational requirements for a given number of particles per unit cell, it suffers from the disadvantages of leading to inhomogeneous overall properties even in the elastic range, compare e.g. Weissenbek [1994], and of considerably underestimating the fluctuations of the microstresses in the particles (Han *et al.* [2001a]). It is also incapable of accounting for inter-particle fluctuations of the stresses and strains, which are an important arrangement effect that can be studied by unit cells with statistically based microgeometries (Han and Böhm [2002]).

Accordingly, in the following unit cells are used that aim at approaching the properties of **R**epresentative **V**olume **E**lements (RVEs) for statistically homogeneous particle distributions. In addition, the following assumptions are made:

- All particles are assumed to be of the same shape (which fits well for modeling powder metallurgically produced HSS, see figure 10, but is an approximation for MMCs consisting of aluminium reinforced by SiC),

- have isotropically elastic material behavior up to failure,

- and are perfectly bonded to the matrix.

Two algorithms were used for generating the particle arrangements of the unit cells. Initial development work was performed on **R**andomly **P**runed **C**ube (`RPC`) arrangements, which are fairly easy to mesh. For "production runs" geometries generated by **R**andom **S**equential **A**dsorption (`RSA`) algorithms were employed. It may be noted that the algorithms developed here can in principle be used for any type of microgeometry consisting of spherical particles embedded in a matrix. The `RSA`-approach is limited to a particle volume fraction of about 25 %, depending on number, size and shape of the particles,

whereas the RPC-method would allow a considerably higher reinforcement volume fractions, theoretically, for a qualitatively acceptable FE-mesh, but with the price of having higher regularity (it approaches the sc arrangement).

3.1.1 Randomly Pruned Cube Arrangement of Spheres in a Unit Cell (RPC-Cells)

In this subsection the creation of one RPC-unit cell used within the present work is described. The cube shaped unit cell is built up of an appropriate number of identical cube shaped subvolumes, in each of which provision is made for a centered spherical region. In order to obtain phase arrangements of some given volume fraction of particles, an appropriate number of these spheres is selected by a random procedure to have the material properties of particles. All other spheres as well as all other volumes are treated as matrix. Figure 11 shows such an RPC arrangement consisting of 64 subvolumes of side length $l_{1,2,3}^{subcell} = 0.25$, the diameter of all spheres being $d_{\o} = 0.2$. Designating fifteen of these spheres as particles results in a total particle volume fraction of $\xi = 6.3\%$.

This method evidently gives rise to phase arrangements that are much more irregular than the sc, bcc or fcc arrays that were frequently used in the literature (see e.g. Hom and McMeeking [1991]; Weissenbek *et al.* [1994]). Even arrangements with differently sized spheres can be generated this way up to a certain point.

Nevertheless, even though considerable irregularity is evident in such microgeometries, interparticle distances are constrained to remain relatively large and particle positions in figure 11 clearly show patterns of layering and alignment. For identifying the individual spheres for later discussion they are assigned to four layers, named A to D. The numbering scheme is explained in figure 11. It may be noted that the realism of the arrangements might be improved by using spheres that are randomly offset from the centers of the subcubes, but at the cost of losing much of the simplicity of the basic scheme.

3.1.2 Cells Created by the Random Sequential Adsorption Approach (RSA-Cells)

A variant of the RSA, see e.g. Rintoul and Torquato [1997], is the technique of choice for approximating random distributions of inclusions by unit cells in the present work.

In general, this method for generating reinforcement positions starts with choosing the

volume fraction, number of reinforcements per unit cell and limiting variations of sizes and shapes of the reinforcements. With this initial information positions are created sequentially for each reinforcement center by using a random number generator. These positions are accepted, if the "new" reinforcements do not intersect with or do not approach too closely to (with respect to some minimum distance) reinforcements already present. Otherwise new center coordinates have to be generated. For nonspherical reinforcements the orientations, sizes and shapes of the reinforcements have to be considered additionally. Depending on the number, shape and size variations RSA-type approaches are limited to particle volume fractions below, say, 25%. Higher volume fractions tend to lead to geometric frustration due to the scarcity of free volumes for additional particles.

A general version of the modified RSA approach accounting for user specified particle distances and the periodicity of unit cells can be explained in detail as follows (Han *et al.* [2001b]):

The surface of each inclusion j can be described by a parametric equation

$$ {}^{j}\underline{X} = {}^{j}\underline{X}({}^{j}\underline{c}, {}^{j}\underline{\beta}, {}^{j}R, {}^{j}s) \quad \text{with} \quad j = 1, \ldots, N, \tag{3.1} $$

where the vector valued function ${}^{j}\underline{X}$ gives the position of each point on the j-th particle's surface, ${}^{j}\underline{c}$ is a reference position of the particle center, ${}^{j}\underline{\beta}$ the orientation vector, ${}^{j}R$ the size parameter and ${}^{j}s$ is a free parameter (e.g. describing the shape). For positioning the next new particle i its distance ${}^{i,j}\Delta$ to each of the previously accepted particles $j = 1, i-1$ has to be equal to or larger than a user selected minimum separation D:

$$ {}^{i,j}\Delta = \| {}^{i}\underline{X}({}^{i}\underline{c}, {}^{i}\underline{\beta}, {}^{i}R, {}^{i}s) - {}^{j}\underline{X}({}^{j}\underline{c}, {}^{j}\underline{\beta}, {}^{j}R, {}^{j}s) \| \tag{3.2} $$

$$ {}^{i,j}\Delta \geq D \quad \text{with} \ j = 1, i-1. \tag{3.3} $$

In order to allow the use of periodic boundary conditions (eqn. (3.12)) of the unit cells for the surfaces of neighboring particles in adjacent unit cells the relations

$$ {}^{j}\underline{X}({}^{j}\underline{c}^{\,k}, {}^{j}\underline{\beta}, {}^{j}R, {}^{j}s) = {}^{j}\underline{X}({}^{j}\underline{c} \pm \underline{h}^{k}, {}^{j}\underline{\beta}, {}^{j}R, {}^{j}s) = {}^{j}\underline{X}({}^{j}\underline{c}, {}^{j}\underline{\beta}, {}^{j}R, {}^{j}s) \pm \underline{h}^{(k)} \quad \forall \ k \tag{3.4} $$

must hold, i.e. each of the cubes making up the phase arrangement contains the same number and arrangement of particles as the original cell. Here k describes the k-th adjacent cell ($k = 1, \ldots, 26$ in the case of cube-shaped unit cells: 6 nearest neighbors, 12 next-nearest neighbors, 8 third-nearest neighbors) and $\underline{h}^{(k)}$ the unit cell translation (periodicity) vector for obtaining the k-th adjacent cell

$$ \underline{h}^{(k)} = q_1^{(k)} \cdot \underline{a}^{\,(1)} + q_2^{(k)} \cdot \underline{a}^{\,(2)} + q_3^{(k)} \cdot \underline{a}^{\,(3)} $$

$$\text{with } q_l^{(k)} = 0, \pm 1, \ l = 1, 2, 3, \ k = 1, \ldots, 26. \tag{3.5}$$

where $\underline{a}^{(1)}$, $\underline{a}^{(2)}$ and $\underline{a}^{(3)}$ represent the base vectors of the unit cell. Note that eqn. (3.2) and eqn. (3.3) also have to be fulfilled for particles positioned in adjacent unit cells; for nonspherical reinforcements their evaluation can be a considerable computational effort.

This method allows to generate rather realistic and general arrangements of spheres. Figures 12 to 15 display arrangements obtained by positioning fifteen equally or bidispersely sized spherical particles within unit cells using the modified `RSA`-method. It is clear that more irregular microgeometries can be generated for a given volume fraction, numbers of particles, particle size and particle shape with this approach, compared to the `RPC`-method.

Even though the maximum number of inclusions per unit cell has been chosen to fifteen for the present work, which is expected to be sufficient for a satisfactory description of the overall elastic properties (compare Drugan and Willis [1996]) of the modeled PRDMCs (with overall isotropic material behavior), a higher number of inclusions per unit cell would be preferable for modeling the behavior in the elastoplastic and damage regimes. At present the number of particles is limited by hardware and software resources, especially for modeling 3D unit cells by Finite Elements with the present sequential particle cleavage approach (for more detailed discussions refer to section 3.3, too).

3.2 Geometric Characterization of Inclusion Arrangements

The aim of ideal multi-inclusion unit cells is to correspond to RVEs for the full description of the material to be studied Hashin [1983]; Markov [2000]. Actually, as mentioned above, the size of phase arrangements is limited at present by available computational power. In general it is difficult to show that a given volume element is a proper RVE for a given material.
Drugan and Willis [1996] estimated for the case of elastic statistically isotropic composites with matrix-sphere inclusion topology, that the overall moduli can be approximated within errors of less than 5% (1%) by volume elements of the size of approximately two (five) inclusion diameters independent of the reinforcement volume fraction. Even though the above estimates were not developed for periodic microgeometries, they were also found to be applicable to this case (Gusev [1997]). No comparable estimates are available for nonlinear composites. Studies, however, strongly point out that the use of larger volume

elements for nonlinear material behavior is necessary for obtaining accuracies comparable to the linear case (Böhm and Han [2001]).

Arrangements of non-overlapping ("hard core") inclusions can be characterized in different ways.

First, the so called second-order intensity function (Bulsara *et al.* [1999]; Pyrz [1994a]) may be used, which is defined as

$$K(r) = \frac{\bar{n}(r)}{N_V} = \frac{1}{N_V} \sum_{k=1}^{N_V} \frac{I_k(r)}{N_V}, \tag{3.6}$$

where $\bar{n}(r)$ is the mean number of inclusions within a spherical volume of radius r around a particle center, $I_k(r)$ is the number of particle centers within this region and N_V is the total number of particle centers within the viewing region (= unit cell). So $K(r)$ gives the average number of particles within a radius r of an arbitrary particle of the diameter D and should be able to differentiate between different (more or less regular) arrangements (Pyrz [1994a]). For two arrangements of fifteen particles each, one created by the `RPC` method and one by the `RSA` method, the comparison with the Poisson pattern is given in figure 16. The differences are not too significant, even with the small number of particles, and the $K(r)$ computed for the unit cells deviate from the reference Poisson arrangement only by about 5% within one unit cell distance.

Second, the intensity distribution of inter-inclusion distances is of interest, to answer the question of what are the most (less) frequent distances of particles in the arrangements. With the definition of a **P**air **D**istribution **F**unction (PDF) of the particle centers,

$$g(r) = \frac{1}{N_V} \frac{dK(r)}{4\pi r^2 dr}, \tag{3.7}$$

where $dK(r) = K(r + dr) - K(r)$ is the number of particle centers within the spherical shell $4\pi r^2 dr$ at the distance r and N_V is the number of the particles within the viewing volume, a correlation length r_0 can be determined. Following Pyrz [1994b] r_0 is defined as the distance beyond which the PDF $g(r)$ ceases to deviate strongly from unity, provided a statistically homogeneous particle center distribution is given (note that $g(r) = 1$ represents the random Poisson point distribution).

In the two diagrams in figure 17 $g(r)$ is given as a function of the non-dimensional radius $\frac{r}{D}$, where r is the distance and D the particle diameter, respectively: the left diagram represents the PDF for one `RPC`-generated unit cell and for one `RSA`-generated unit cell. Even after averaging the PDFs of five different `RPC`-generated arrangements of hard core

inclusions and doing the same for the PDFs of `RSA`-generated arrangements, see figure 17, right, noticeable peaks in $g(r)$ are present, which are due to the periodic arrangement of unit cells containing a small number of particles (a much smoother behavior is evident when a unit cell containing some 5000 particles is evaluated). Whereas averaging different `RSA`-generated PDFs shows a clear tendency towards smoothing the $g(r)$-function, the average of the PDFs of `RPC`-generated unit cells continues to demonstrate their regularity. Naturally this is a consequence of the method itself, arranging particles on quite a low number of possible positions within the cell, in contrast to the `RSA` approach, where the particle positions are in principle statistically equivalent (every point within the unit cell may be a particle center). This means that within the unit cells created by the `RPC`-method, certain particle distances are quite probable and averaging over a number of arrangements does not reduce this geometrical regularity. In contrast, averaging the PDFs of some unit cell arrangements generated by the use of the `RSA`-approach shows the deterministic nature of these geometries.

Nevertheless it should be noted that even unit cells sized either to the estimates of Drugan and Willis [1996] or to the correlation length generally are not RVEs in a strict sense, and the homogenized behavior of each cell will usually differ from the corresponding ensemble average over a number of cells.

For `RSA` unit cells with a side length $l_0 = 1$ that contain fifteen particles at particle volume fractions of $\xi = 6.3\%$ (15%), the side lengths normalized to the particles' diameter, $d_\emptyset = 0.2$ (0.268) are $l_0/d_\emptyset \approx 5.0$ (3.7), which is in the range given by Drugan and Willis [1996] to obtain overall elastic behavior within errors of a few percent. However, the relatively low number of particles provides only a rather coarse approximation of the particle arrangement statistics as is indicated by the diagrams in figure 17. Accordingly, the results are best interpreted as pertaining to periodic model composites that approximate but do not attain the microstructures of actual composites.

3.3   Implementation

3.3.1   Modeling Assumptions

In order to keep the study reasonably simple and in accordance with the aims stated in section 3.2, idealized models of PRDMCs were generated and studied. Simplifications in terms of the constituent material response took the form of prescribing isotropically

elastic material behavior for the particles, assuming perfect bonding between matrix and particles, and describing the matrix by a J_2 continuum plasticity model with a modified Ludwik hardening law of the type

$$\sigma_{\mathrm{y}} = {}^{0}\sigma_{\mathrm{y}}^{(\mathrm{m})} + h \cdot (\varepsilon_{\mathrm{eq,p}}^{(\mathrm{m})})^{n}, \tag{3.8}$$

where σ_{y} is the actual flow stress, ${}^{0}\sigma_{\mathrm{y}}^{(\mathrm{m})}$ the initial yield stress of the matrix, $\varepsilon_{\mathrm{eq,p}}^{(\mathrm{m})}$ the accumulated equivalent plastic strain in the matrix, and h and n stand for the hardening coefficient and the hardening exponent, respectively. All analyses were carried out for initially stress free and virgin materials, i.e. the residual stress states that are typically present in PRDMCs (Ho and Lavernia [1995]) were not accounted for (even though this is in principle possible with the methods used). Because the thermal residual stress states of the reinforcements of PRDMCs typically are compressive, the latter assumption may lead to some underestimation of the strength with respect to particle failure.

Brittle failure of the particles under uniaxial tensile loading was modeled as "instantaneous total cleavage" along predefined fracture surfaces, which in the undeformed state are assumed to be planar, to be oriented normal to the macroscopic loading direction and to pass through the particles' centers. These assumptions, while not unreasonable, neglect perturbations to the local stress fields caused by both intact and fractured neighboring inclusions, which may influence the position and orientation of cracks within the inclusions (for more detailed considerations distinguishing between polycrystalline particles and monocrystalline particles would be necessary, where for the latter specific cleavage planes must be regarded). While always leading to total splitting of the involved particle, cracks were assumed to be arrested immediately after starting to penetrate into the matrix. Damage and crack growth by interfacial decohesion or ductile matrix damage were not accounted for. This modeling approach is related to the one proposed in Ghosh and Moorthy [1998]. It limits the evolution of damage to the sequential failure of particles and clearly constitutes a major simplification compared to the complexities of microscale damage in actual PRDMCs. It is, however, very suitable for studying the influence of various parameters on particle fracture.

Weibull-type (Weibull [1951]) fracture probabilities were evaluated for each particle j at each load increment by using the expression given by eqn. (2.21). The use of Weibull fracture probabilities for modeling the brittle failure of particles embedded in ductile matrices can account for effects of the absolute size of the inclusions and is well established in the literature, see e.g. Antretter and Fischer [1998]; Bréchet *et al.* [1991]; Lewis and

Withers [1995]; LLorca *et al.* [1997]. A detailed discussion of the strengths and weaknesses of such approaches can be found in Wallin *et al.* [1987]. It should be noted, however, that Mummery *et al.* [1993] found that Weibull-type criteria for failure could not account for the dependence of experimentally measured acoustic emission events on the particle size in a particle reinforced MMC (in their work, particle and interfacial failure are brittle and thus amenable to detection by acoustic emission methods).

A further simplification was introduced by approximating the microgeometry of an actual composite by an infinite periodic arrangement of particles described by three-dimensional unit cells that contain a limited number of identically shaped inclusions. Within this modeling strategy, the failure of a single inclusion in the unit cell corresponds to a material in which a periodically repeating pattern of local damage occurs. Two modeling schemes were used to generate unit cell geometries that approach statistically isotropic particle arrangements, as was described above, see sections 3.1.1 and 3.1.2.

3.3.2   Particle Cracking Model

The particles in the multi-inclusion unit cell model are assumed to be fully intact and initially stress-free when no loading has been applied to the material. This "virgin state" serves as the beginning of the simulations (however, the influence of thermal residual stresses can be considered in future investigations). Furthermore an inclusion is supposed to have two different exactly defined geometrical states, which may be called intact state, with the probability p (one sphere), and cracked state, probability q (two halves of a sphere). The intact particle can be treated as "one piece", in our case of spherical shape with elastic material properties. On the other hand the cracked particle is split into "two halves", load transfer across the crack(planes) within the particle being impossible.
Each of the particle states has a certain probability; one state excludes the other, i.e. for the probabilities of both possible states

$$p + q = 1 \tag{3.9}$$

must hold. The question now is the determination of the probability q of the cracked state.

As mentioned in chapter 2, in the literature the Weibull approach is well established for probabilistic descriptions of particle fracture. On the one hand, the Weibull fracture probability $P_{\mathrm{fr},j}$ of particle j, computed with eqn. (2.21) can be directly interpreted as the probability of the cracked state, q. A criterion for deciding that the particle fails, would

be the comparison of the actual particle fracture probability with a critical fracture probability limit $P_{\mathrm{fr},j}^{(\mathrm{tol})}$. Because the particle fracture probability is directly related to the stress distribution inside the particle, this method is equivalent to a comparison with a particle averaged critical stress limit, that is sensitive to the particle size. In this work this type of particle failure activation, frequently used in literature (e.g. see LLorca [1996]), is referred to as a **W**eibull **R**ankine method (`WR`-method).

On the other hand, additional considerations lead to an alternative method for activating particle failure, the so called **M**onte **C**arlo **W**eibull method (`MCW`-method): As the applied load on a composite is increased, the Weibull fracture probabilities of the individual particles also tend to increase. It should be noted, however, that due to load redistribution effects, caused e.g. by plastic yielding of the matrix or by the failure of other particles, the Weibull fracture probability of any given particle does not necessarily grow monotonically, even for strictly monotonically increasing radial macroscopic loading and neglecting other damage mechanisms. In the present simulations a Random Walk procedure decides for each inclusion at which step of the numerical loading process the change from state p to state q happens (after the change no "healing" of the intact particle is allowed, so no more Random Walk procedure is required). The question is the relation between the probability p of the intact state and the probability q of the cracked state which must change in dependence on the loading state of each individual inclusion. For this relation the following method is used:

> The probability of failure $P_{\mathrm{fr},j}$ of particle j is given by the Weibull relation eqn. (2.21), as described in chapter 2.
>
> Within the Random Walk model employed in the present work it is assumed, that Weibull fracture probabilities previously survived by a given particle will not give rise to fracture later on. Accordingly, it is the increase in the Weibull fracture probability with respect to highest previous value, $\Delta P_{\mathrm{fr},j}$, which is used to determine of a given particle fails under a given applied load, compare Pandorf [2000].
>
> This modeling assumption appears to be realistic for approximately radial load paths. For different stress distributions within a given particle that lead to similar fracture probabilities (e.g. under radically different applied loads), however, the validity of the concept may be questionable, because different populations of flaws may be activated.
>
> Thus, assuming that previously survived stress levels within the particles will not lead to particle failure, only the effects of increases in the stresses in the

particles must be considered. This means, based on the maximum Weibull fracture probability $P_{\mathrm{fr},j}^{(\mathrm{max})}$ survived, the increment $\Delta P_{\mathrm{fr},j}$ to the actual probability $P_{\mathrm{fr},j}^{(\mathrm{actual})}$ has to be taken into account and we define (compare figure 18 for an explanation of a difference $\Delta P_{\mathrm{fr},j}$ of probabilities related to two different stress states σ_i and σ_{i+1})

$$\Delta P_{\mathrm{fr},j} = P_{\mathrm{fr},j}^{(\mathrm{actual})} - P_{\mathrm{fr},j}^{(\mathrm{max})} \tag{3.10}$$

$$\text{if} \quad \Delta P_{\mathrm{fr},j} \geq 0 \quad \text{then} \quad p = 1 - \Delta P_{\mathrm{fr},j} \quad \text{and} \quad q = \Delta P_{\mathrm{fr},j}. \tag{3.11}$$

With a Random Walk procedure the failure of a particle is decided, where the probability for the cracked state q is determined by the difference given by the actual Weibull fracture probability and the previously survived fracture probability. The implementation actually employed is described in section 3.3.4.

One benefit of using the Random Walk method for the activation of particle failure is the possibility of using the same particle arrangement for a number of simulations to obtain statistically more relevant results for the material simulated. Of course, each application of the Random Walk procedure leads to a different sequence of failure events for the same particle arrangement and the same load history, in accordance with the assumed statistical nature of particle fracture (in the meaning of having different critical flaw distributions within each particle). In the present study the combination of the generation of different geometrical arrangements and the Random Walk procedure applied to particle fracture for the same geometrical arrangement is used for generating statistically relevant data.

3.3.3   Finite Element Model

The microscale stress and strain fields in the unit cells were evaluated with the FE-code ABAQUS/Standard V.5.8 (Hibbitt *et al.* [1998]) using modified tetrahedral elements with quadratic shape functions (3D10M) to avoid possible volume locking in yielded matrix regions. Contour plots of the stress fields were generated with the ABAQUS/Post Processor V.5.8. based on the computed integration point data. Note that the ABAQUS/Post Processor does not average across element set and material set boundaries. This can be seen in stress field images, where two element sets of the same material are adjacent and the contour plots are not continuous across the element set boundary, see e.g. figure 31. Meshing was carried out either with the preprocessor PATRAN V.8.0 (MacNeal-Schwendler Corp. [1998]) or with the preprocessor NETGEN (Schöberl [1997]), a fracture surface (or a set of three perpendicular fracture surfaces) as described above being provided for each

particle. The analyses in the present study were carried out as displacement controlled geometrically nonlinear incremental-iterative computations describing loading by uniaxial tension and the incrementation was chosen automatically by ABAQUS. The models are prepared for general loading conditions (tension, biaxial tension, shear, hydrostatic tension and compression), but particle failure can only take place along the predefined crack planes, presently modeled parallel to the unit cell faces.

For leading to valid results both in the deformed and undeformed geometry states, the usage of unit cells requires the correct formulation of boundary conditions for all nodes lying at the unit cell surfaces, giving rise to a periodically repeating model that avoids gaps and overlaps. Thus periodic displacement boundary conditions were used throughout:

$$u_i(x_k + l_i) = u_i(x_k) + c_i \quad . \tag{3.12}$$

Here l_i represents the edge lengths of the unit cell, $c_i = l_i - l_{0,i}$ the overall deformation of the unit cell in $i-$direction and u_i are displacements at the node with the coordinates x_k. Typical element counts for a model as shown in figure 12 were about 50000 10-node tetrahedra (for RPC-arrangements good mesh qualities are obtained with about 40000 tetrahedra per unit cell, shown in figure 11).

Particle failure on the predefined fracture surfaces (perpendicular to the global loading direction) was modeled by a node release technique and was controlled by the Weibull fracture probabilities of the individual particles as discussed above. The actual implementation used the ABAQUS user subroutines MPC, UVARM, and UEXTERNALDB (described in section 3.3.4) to identify particles fulfilling the failure conditions, to instantaneously disconnect all degrees of freedom across the fracture surface within such a particle, and to subsequently reestablish equilibrium within the next load increment. Despite the numerical difficulties associated with the reduction in overall stiffness and the marked rearrangement of local stresses upon the instantaneous release of a considerable number of degrees of freedom, the above procedure was found to be reliable in obtaining convergence. In the present model particle cleavage occurs at actual loads which evidently depend on the local stress distributions and thus on the chosen arrangement of particles, and in the case of MCW-models, additionally on the statistics of each simulation run. Accordingly, an important point in the implementation was the development of a fully automatic algorithm, in which no user intervention is required during a run involving successive fracture of a number of particles. The calculation of the inclusions' Weibull fracture probabilities made use of a feature of ABAQUS that allows the approximate evaluation of volume integrals of some

function f over some subvolume, in this case particle j, by a weighted sum of the type

$$\langle f \rangle_j = \frac{1}{V_j} \int_{V_j} f(\underline{r}) dV \approx \frac{1}{V_j^{(\text{int})}} \sum_{l=1}^{N_j} f_l V_l \quad \text{with} \quad \sum_{l=1}^{N_j} V_l = V_j^{(\text{int})} \quad . \tag{3.13}$$

Here f_l stands for the value of the function $f(\underline{r})$ at integration point l, which is weighted by the volume V_l associated with this integration point and $V_j^{(\text{int})}$ is the particle volume. N^j is the total number of integration points within particle j.

Note that in the FE-meshes generated by the automatic mesher of the preprocessors the node positions typically are in full agreement with the prescribed geometry, but between the nodes the geometry is interpolated by triquadratic functions. For spherical particles this typically leads to meshes in which the discretized particle volume $V_j^{(\text{int})}$ is slightly smaller than the prescribed volume $V_j^{(\text{geom})}$, i.e.

$$V_j^{(\text{int})} \leq V_j^{(\text{geom})} \quad . \tag{3.14}$$

For the RPC unit cells used in the present work (arrangements A and B) the actual particle volume fraction (as evaluated from the corresponding integration point volumes) is about $\xi^{(\text{int})} = 6.1\%$ (instead of a nominal value of $\xi^{(\text{geom})} = 6.3\%$). The corresponding values for the RSA models are $\xi^{(\text{int})} = 14.7\%$ for arrangement C, $\xi^{(\text{int})} = 14.8\%$ for arrangement D, $\xi^{(\text{int})} = 14.4\%$ for arrangement E and $\xi^{(\text{int})} = 14.6\%$ for arrangement F, the nominal particle volume fraction being $\xi^{(\text{geom})} = 15\%$. The relatively high differences of up to 4% of the particle volume fraction in arrangements E and F are due to the presence of smaller particles, the relatively high curvature of the surface of which is approximated by a relatively small number of quadratically interpolated triangular facets. It should be noted that differences in the volume fractions of the above order of magnitude typically have the consequence that numerical predictions for the elastic moduli using the discretized geometry tend to lie somewhat below variational bounds evaluated for the nominal volume fraction, compare sections 4.1 and 4.2.2.

Evaluation of Homogenized Stress and Strain

Predictions of the overall responses of the model materials were characterized in terms of the effective (elastoplastic) stress vs. strain curves, the effective Young's moduli and the effective Poisson's ratios, all of which were evaluated as the homogenized responses of the unit cell. Within the displacement based FE-formulation used by ABAQUS the unit cell responses to applied strain were obtained in terms of their overall displacements u_i ($i = 1, 2, 3$, coordinate).

For reasons of convergence the simulations were carried out under displacement control, i.e. the load was applied in form of an uniaxial displacement prescribed to an appropriate master node, where $|\underline{u}| = u_{ii}$ in direction i and $i = 1, 2, 3$ (the u_{jk} $\forall j, k = 1, 2, 3$ and $j, k \neq i$ result out of the Poisson effect). The corresponding overall logarithmic strains were evaluated as (where for the present study only uniaxial loading states in i-direction are considered and therefore only the i-components are of interest)

$$\varepsilon_{ii} = \int_{l_{0,i}}^{l_i} \frac{dl}{l} = \ln \frac{l_i}{l_{0,i}} \quad , \tag{3.15}$$

where $l_{0,i}$ is the initial length (reference length) of a side of the unit cell and $l_i = l_{0,i} + u_i$ is the corresponding length in i-direction in some deformed state. The actual stress components then can be obtained from the predicted reaction force $\underline{F}$ acting on the unit cell surface area $A^{(i)}$. The area $A^{(i)}$ is defined by the unit cell lengths in the deformed state

$$A^{(i)} = |\underline{l}^{(j)} \times \underline{l}^{(k)}| \quad i, j, k = 1, 2, 3 \quad i \neq j \neq k \quad . \tag{3.16}$$

Hence for all directions i, and where again in fact only the components $i = j$ are of interest, the stress components follow as

$$\sigma_{ij} = \frac{F_i}{A^{(j)}} \tag{3.17}$$

and for uniaxial strains $\varepsilon_{ii} \neq 0$ in i-direction this means $\sigma_{ii} \neq 0$ and $\sigma_{kl,k\neq l} = 0$.

The logarithmic strain and the true stress formulation are used, because for some computations considerable macroscopic strains are involved. Piecewise linear stress-strain curves were obtained from the increment-wise predictions for the homogenized stresses and strains. The overall Young's moduli E^* were evaluated by numerically differentiating the overall stress-strain curves.

Evaluation of Porosity

Following fracture the fragments of particles tend to be pulled apart, which gives rise to voids. With the actual overall model volume $V_{\text{model}}^{(\text{geom})} = l_1 \cdot l_2 \cdot l_3$ (where l_1, l_2 and l_3 correspond to the actual edge lengths of the unit cell) and the sum of all element volumes, the overall integration volume $V_{\text{model}}^{(\text{int})} = \sum_i V_i^{\text{element}}$ (where the element volume $V_i^{\text{element}} = \sum_l V_l^{(i)}$ is the sum of the integration point volumes $V_l^{(i)}$ of element i, compare eqn. (3.13)), the overall void volume fraction can be obtained as

$$f_v = 1 - \frac{V_{\text{model}}^{(\text{int})}}{V_{\text{model}}^{(\text{geom})}} \quad . \tag{3.18}$$

Together with the applied strain data the evolution of the pore volume fraction (due to particle cleavage) can be observed. The growth of these voids into the matrix, however, was not evaluated in the present study.

Evaluation of the Matrix Damage Indicator

In section 2.2 a ductile damage indicator is explained. Within the present study an user defined ABAQUS subroutine UVARM was implemented, which evaluates this damage indicator in each of the integration points of the matrix elements, but does not affect the local stiffness of the matrix material, i.e. it provides an uncoupled damage description of the matrix state. With the ABAQUS/Post Processor V.5.8 (Hibbitt *et al.* [1998]) critical integration point volumes in the meaning of having a damage indicator of $D_i^{(m)} \geq 1$ can be shown via contour plots. Thus, at least qualitative predictions can be obtained on the basis of the prescribed material data (tables 3 and 4) and regions in the unit cell, where matrix damage may be expected, are identified.

Evaluation of Interfacial Tractions

For a qualitative discussion of the situation within the interfaces between particle and matrix the magnitudes of the normal and tangential tractions were evaluated using the stress data available in the integration points of elements adjacent to the interface (Hibbitt *et al.* [1998]). However, stiffness loss due to interfacial damage was not activated in the studies presented here.

Within each integration point of the FE mesh close to the particle's surface (more precisely it is the nodes lying on the particle surface that are associated to the interface particle–matrix) a coordinate system was defined as follows. First a unit radius vector of the particle (which is by definition a normal vector of the surface of a spherical particle), $\underline{n}$, pointing outwards, was defined. Second, a unit vector $\underline{t}_1$ oriented perpendicularly to $\underline{n}$, and thus lying in the tangent plane to the particle surface, was chosen. Finally a second tangent unit vector $\underline{t}_2$ was obtained as $\underline{t}_2 = \underline{n} \times \underline{t}_1$, so that a tangent plane at the integration point is defined by $\underline{t}_1$ and $\underline{t}_2$. With the stress tensor $\underline{\sigma}$, given in the integration point, and with the unit vectors of the local coordinate system, $\underline{n}$, $\underline{t}_1$ and $\underline{t}_2$, the components of the traction vector are obtained as:

$$T_n = (\underline{\sigma} \cdot \underline{n})\, \underline{n} \quad T_{t,1} = (\underline{\sigma} \cdot \underline{t}_1)\, \underline{t}_1 \quad T_{t,2} = (\underline{\sigma} \cdot \underline{t}_2)\, \underline{t}_2 \quad . \tag{3.19}$$

The results can then be visualized as separate contour plots with the ABAQUS/Post Processor V.5.8 (Hibbitt *et al.* [1998]), which extrapolates these integration point data onto the particle surfaces, i.e. the interface particle–matrix. These contour plots on the one hand show the magnitude of the normal traction, T_n, and, on the other hand, the magnitude of the tangential tractions,

$$T_t = \sqrt{T_{t,1}^2 + T_{t,2}^2} \quad . \tag{3.20}$$

For referring to positions on the particles' surface, the poles of the particles are defined as the points on the particle surface for which the coordinates have minimum or maximum values in the direction of the global maximum principal stress. Consequently the equatorial plane coincides with the predefined crack plane.

3.3.4 Routine for Simulating Particle Cleavage

Figure 19 schematically shows the algorithm implemented for controlling particle fracture, the user defined ABAQUS subroutines `MPC`, `UVARM` and `UEXTERNALDB` being employed. Within the ABAQUS subroutine `UVARM` the required stress values and the integration point volumes of each integration point within the model are available. For each element within a particle the risk of fracture (eqn. (2.4)) is computed for every iteration. At the end of each increment (after finding a new equilibrium state after increasing/decreasing the applied uniaxial strain) with this data the fracture probabilities of each of the particles are accumulated, using the subroutine `UEXTERNALDB`. At this position in the program the decision on particle failure is made.

If the "Rankine Procedure" `WR` (section 3.3.2) is used, the actual Weibull fracture probability of particle j is simply compared with a limit, $P_{fr,j}^{(tol)}$ (green path in figure 19). On exceeding this threshold, particle fracture is activated.

Alternatively the "Monte Carlo Method" `MCW` can be used. Following the red path in figure 19, this method stipulates, that particle failure can take place only if the actual Weibull fracture probability, $P_{fr,j}^{(actual)}$, exceeds the maximum Weibull fracture probability previously survived by the particle. The difference $\Delta P_{fr,j}$ (eqn. (3.11)) is compared with a random number z. When the value of $\Delta P_{fr,j}$ is higher than z the particle fails. Otherwise the actual survived Weibull particle fracture is updated to $P_{fr,j}^{(max)} = P_{fr,j}^{(actual)}$. This is done for each of the modeled particles, failure of multiple particles being possible. Within the next increment stress redistribution takes place and a new equilibrium has to be found. This method implies that a strong increase of the maximum principal stress inside some

particle within one load increment increases the probability of the particle to fail.

Once a particle has been flagged for fracture, the **M**ulti **P**oint **C**onstraints (MPCs), which tied together the crack planes of the two halves of the particle up to this point, are released via the subroutine MPC before applying the next load increment. This "node release" results in a reduction of stiffness, stress redistribution has to take place within the model, and therefore a new equilibrium state must be found in the next increment. For the latter task three different schemes may be used: In the case of load controlled analyses a "zero load increment" can be specified, i.e. a new equilibrium strain at the current load level is solved for. This gives rise to horizontal sections (i.e. jumps in overall strain) in the stress-strain diagram, compare A in figure 20. Typically this strategy leads to considerable numerical difficulties and convergence problems, especially in the highly non linear range. Accordingly, analyses using load control typically are not the best choice for the particle fracture simulations. Instead, the simulations were carried out under displacement control, i.e. overall displacements were applied instead of forces. Applying a "zero displacement increment" for reestablishing equilibrium, leads to a global stress-strain behavior marked as B in figure 20, i.e. a sudden drop in the overall stress. In the present study a third alternative for the step control was used, which consists of letting the auto incrementation algorithms of ABAQUS select an appropriate displacement increment following the node release event. This gives rise to equilibria that lie between those activated by "freezing" either the applied stress or the applied strain. These solutions are perfectly valid, but some care may be required in interpreting the resulting stress-strain diagrams, where particle fracture gives rise to reductions in stress with a finite negative derivative, compare figure 20. Besides being relatively simple to code this approach has the advantage that the standard ABAQUS incrementation algorithm is disturbed as little as possible, typically leading to a relatively low total number of increments (and thus reduced computational effort).

It is worth noting that with some minor modification the same set of user subroutines may also be used to simulate interfacial decohesion between particles and matrix, see appendix C. This option, however, was not explored in depth in order to concentrate on modeling particle fracture.

Chapter 4

Results – Discussion

The unit cell models were used for studying the material behavior of materials with spherical reinforcements. The assumption of spherical reinforcing particles, on the one hand, is motivated by the emphasis of the present study on powder metallurgically produced PRDMCs, which in many cases show sphere-like reinforcements and, on the other hand, is a consequence of the need to minimize the modeling effort and to facilitate the interpretation of the results. For the materials covered, certain aluminium matrix MMCs and powder metallurgically produced HSSs, it is known from experiments that particle cleavage plays an important role in the initiation of damage and failure. In this section unit cell models are used for numerical materials characterization, mainly in terms of generating overall stress-strain diagrams and for studying "particle damage relevant parameters" such as maximum principal stresses and particle fracture probabilities. Furthermore, in the course of the simulations the evolution of the matrix behavior and the interface conditions are "observed" via the evaluation of the damage indicator and the magnitudes of interface traction components, respectively. In addition, the evolution of porosity due to particle fracture is followed.

Due to the considerable number of results presented in this chapter, a unified scheme for designating the unit cell models is used. All unit cell results, which are typically ensemble averages over a number of equivalent geometries and/or load cases, are identified by a designator of the type $AA_{vol.\%}^{bb} - X/CCC$. "$AA_{vol.\%}^{bb}$" informs about the material

to be modeled, where "$_{\text{vol.\%}}$" gives the total particle volume fraction ($\xi = 6.3$ vol.% or $\xi = 15$ vol.%) and "^{bb}" denotes the information on the modeled microstructure. For the material AA2618/SiC$_p$-T4 (section 4.1) this takes the form of either uniformly sized ("^{eq}") or bidispersely sized ("^{bi}") reinforcements. For HSS, a total of nine groups of results ("$^{\mu 1}$" up to "$^{\mu 9}$") are distinguished, which differ in particle volume fraction particle size distribution and particle material properties, see section 4.2. The descriptor "X" denotes the individual unit cells and arrangements used, which are introduced in sections 3.1.1 and 3.1.2 and are classified alphabetically from "A" to "F". "CCC" provides information on the type of particle failure triggering method used ("WR" or "MCW", refer to section 3.3.2).

Listings of the two groups of constituent material parameters used in the simulations are given in tables 3 and 4, where E denotes the Young's modulus, ν the Poisson's ratio, σ_0 stands for the average strength of the particles and m is the particles' Weibull modulus. For the elastoplastic matrices J$_2$ continuum plasticity models are used, the strain hardening behavior being described by a modified Ludwik hardening law as given in eqn. (3.8). This isotropic hardening law does not take into account for effects of the grain structure of the matrix. The effects of submicrometer inhomogeneities, such as secondary carbides in the case of HSS, are assumed to be included within the constitutive behavior of the matrix. Time dependent or rate effects of the matrix behavior, which play a negligible role for the scenarios considered here, were not taken into consideration. The reinforcements are treated as isotropic elastic continua.

In the present studies on the one hand a deterministic (Rankine-type) failure criterion was used, in which a particle j is assumed to fail when its fracture probability according to eqn. (2.21) exceeds values of $P_{\text{fr},j}^{(\text{tol},1)} = 0.593$ or $P_{\text{fr},j}^{(\text{tol},2)} = 0.632$. In the case of highly dilute inclusions (within which the stresses and strains are uniform (Eshelby [1957])), these choices correspond to failure occurring when the maximum principal stress in the particle reaches 90% or 100% of the characteristic strength σ_0, respectively. On the other hand, as discussed in section 3.3.4, triggering of particle fracture by the Monte Carlo Weibull model was carried out.

4.1 Simulation of a MMC: AA2618-T4 reinforced by SiC-Particles

The constituent material properties used for the AA2618/SiC$_p$-T4 MMC, see table 3, follow closely the data given in Elomari *et al.* [1998] and LLorca and González [1998]. In the latter work the characteristic strengths of the particles were estimated to lie in the range $\sigma_0 = 0.9$ GPa to $\sigma_0 = 1.5$ GPa and Weibull moduli of $m = 1$, 3 and 6 were considered. Similar estimates for the Weibull modulus of SiC were published by other authors, too, compare Bréchet *et al.* [1991]. For the present work the *median* of the reported data was chosen, see table 3.

The modeled three microstructures studied for the MMCs differ in total particle volume fractions and in the (relative) particle sizes:

- Microstructure AA2618/SiC$_{6.3p}^{eq}$-T4: aluminium matrix reinforced by uniformly sized SiC particles of a total volume fraction $\xi = 6.3$ % arranged in `RPC`-generated unit cells, e.g. arrangement `A` as shown in figure 11.

- Microstructure AA2618/SiC$_{15p}^{eq}$-T4: aluminium matrix reinforced by uniformly sized and randomly arranged SiC particles, total particle volume fraction $\xi = 15$ %. The modeled arrangements `C` and `D` are shown in figures 12 and 14.

- Microstructure AA2618/SiC$_{15p}^{bi}$-T4: aluminium matrix reinforced by bidispersely sized and randomly positioned SiC-particles, total particle volume fraction $\xi = 15$ %; see figures 13 and 15 for arrangements `E` and `F`.

For the computations on AA2618/SiC$_p$-T4-type materials both the `WR`- and `MCW`-particle cleavage activation models were used.

Predictions of Microscale Phase Averages of Stresses and Strains

The different reinforcement volume fractions directly affect the overall materials' stiffnesses and the effective Young's moduli are predicted as $E^* = 76.78$ GPa for microstructure AA2618/SiC$_{6.3p}^{eq}$-T4, and $E^* = 87.41$ GPa and $E^* = 86.75$ GPa for microstructures AA2618/SiC$_{15p}^{eq}$-T4 and AA2618/SiC$_{15p}^{bi}$-T4, respectively. The latter are quite similar, because the microstructures have the same total particle volume fractions and differ only in the particle sizes and arrangements. Generally, the predicted phase averages of the

microscale stresses for an applied strain of $\varepsilon^{\mathrm{a}} = 0.0005$, i.e. in the linear elastic range, are higher in the microstructures with higher total particle volume fractions, see tables 5 and 6. There is some tendency for the stresses to be somewhat higher for geometries with uniformly sized inclusions, microstructure $AA2618/SiC^{eq}_{15p}$-T4, than in those with particles of two sizes, microstructure $AA2618/SiC^{bi}_{15p}$-T4. The former microgeometries also show somewhat stronger intra-particle stress fluctuations as evidenced by the higher standard deviations. For the smaller total particle volume fractions differences between the predicted particle stress averages for unit cells A and B (both represent microstructure $AA2618/SiC^{eq}_{6.3p}$-T4) are not recognizable. A comparison of tables 5 and 6 shows that the numerical predictions for the Young's moduli fall slightly below the lower Hashin-Shtrikman bounds. This behavior is due to meshing effects, the actual volumes of the particles as meshed being slightly smaller than those of the spheres used in generating the microgeometries (to which the nominal particle volume fractions pertain), see eqn. (3.14).

Similar trends are predicted for an applied strain of $\varepsilon^{\mathrm{a}} = 0.22$ when no particle fracture has been activated (table 7), the corresponding overall stresses being listed in table 10. As expected the matrix is yielded at this strain level. The microscale stress averages and standard deviations computed for the matrices for all three microstructures lie in similar ranges, with only slightly smaller magnitudes for $AA2618/SiC^{eq}_{6.3p}$-T4. Marked differences are predicted for the average stresses in the particles. Especially the von Mises stresses and the maximum principal stresses are computed to be higher in $AA2618/SiC^{eq}_{6.3p}$-T4. The high standard deviations of the stresses are due to two effects: On the one hand, there are significant stress gradients in some particles ("intra-particle fluctuations") and on the other hand different particle can be subject to very different stress levels ("interparticle fluctuations"). For a short discussion of these considerations see Böhm *et al.* [2002].

While for suppressed particle failure the highest overall stresses resulting for an applied overall strain of $\varepsilon^{\mathrm{a}} = 0.22$ are predicted for microstructure $AA2618/SiC^{eq}_{15p}$-T4, the most significant reduction of the homogenized stresses due to particle fracture is computed for microstructure $AA2618/SiC^{bi}_{15p}$-T4, about 12%, compared to about 5% (for $AA2618/SiC^{eq}_{6.3p}$-T4, by the use of unit cell A, and $AA2618/SiC^{eq}_{15p}$-T4) and about 3% ($AA2618/SiC^{eq}_{6.3p}$-T4 using model B), see table 10. Comparison with table 9 shows, that this can be interpreted as a size effect. Big particles are expected to fail more easily (Weibull theory) and the failure of a big particle has a larger effect on the response of the unit cell. However, despite some differences in the standard deviations, for all three models the stress averages of the remaining intact particles are predicted to be of the same range. The comparison of the matrix microscale responses obtained for the models where particle

cleavage occured (table 8) with the results obtained with the damage-free model (table 7) for the same applied overall strain $\varepsilon^{\mathrm{a}} = 0.22$ shows similar values with small reductions in the stress averages in the case of particle damage. However, the predicted equivalent plastic strains are more significantly reduced in microstructures AA2618/SiC$_{15\mathrm{p}}^{eq}$-T4 and AA2618/SiC$_{15\mathrm{p}}^{bi}$-T4. For the higher particle volume fraction a higher proportion of the overall strain of $\varepsilon^{\mathrm{a}} = 0.22$ is due to particle failure, but, locally, the strains in the matrix are increased and this means locally high strain gradients.

The same microstructure also gives rise to the largest volume of pores caused by fractured particles, compare table 9. The same table also gives the average stresses of the remaining intact particles, which, of course, are considerably higher than the averages over all particles listed in table 8. They do not, however, reach the stress levels predicted in the model without particle fracture, table 7, mainly on account of the smaller overall load.

In the next sections (4.1.1,4.1.2,4.1.3) some individual simulation results are discussed in detail for each of the modeled microstructures.

4.1.1 Uniaxial Loading of Microstructure AA2618/SiC$_{6.3\mathrm{p}}^{eq}$-T4

Particle Failure Triggered by the Weibull Rankine Model (`WR`)

Uniaxial tensile loading up to overall nominal strains of some 20%, which may exceed the strain range of the actual material, was simulated for the `RPC` phase arrangement (Al2618-T4 reinforced by SiC-Particles, compare table 3) shown in figure 11b. For loading in the 1-direction and using critical Weibull fracture probabilities of $P_{\mathrm{fr},j}^{(\mathrm{tol},1)} = 0.593$ and $P_{\mathrm{fr},j}^{(\mathrm{tol},2)} = 0.632$ the model predicted failure by brittle cleavage of 7 particles, the sequence of fracture being `B15`, `A09`, `B14`, `D03`, `C07`, `C01` and `D05` (Eckschlager *et al.* [2001b]). The end states of the deformation process are displayed in figure 21, where the fractured particles can be easily discerned. Figure 22 shows an analogous result for arrangement `B`.

The corresponding overall uniaxial stress vs. strain relationships obtained by homogenizing the response of unit cell `A` using the above two critical Weibull fracture probabilities are given in figure 23. Each of the curves shows sudden reductions of the overall stress at 5 different strain values, the first three of which correspond to failure of a single inclusion, whereas the other two were each caused by the fracture of 2 particles in quick succession. These marked drops in the homogenized stress, which are not found in experimentally obtained stress vs. strain curves, are a direct consequence of using a periodically repeating microgeometry that contains only 15 particles per unit cell – the failure of a single inclusion

in the unit cell accordingly corresponds to the simultaneous fracture of approximately 6.7% of all particles in the composite. Comparison between the two stress–strain relations shows that for given material properties and a given geometrical arrangement of the spherical particles within the unit cell only the different critical Weibull fracture probabilities control the occurrence of particle cracking at certain overall strains. In figure 23 the sequence of particle cracking is the same for both values of $P_{\mathrm{fr},j}^{(\mathrm{tol})}$, which indicates that for this geometry and for the material properties used here the nonlinear behavior of the matrix does not give rise to major stress redistribution in the load range where particle fracture takes place. As expected, the maximum load carrying capacity of the model composite under uniaxial loading in the 1-direction depends on the critical Weibull fracture probability; for the present example it is coincident with the failure of the third particle (`B14`) at nominal overall strains of approximately 16.6% and 17.8%, respectively.

Because a unit cell description was used, the evolution of damage relevant parameters due to particle cracking could be followed in some detail in the present model. Figure 24 shows the evolution of the Weibull fracture probabilities of 5 selected particles, `D14`, `C01`, `B15`, `B14` and `A09` (the numbering of the particles follows figure 11), the same abscissa scaling being used as in figure 23. The first four of these particles fail within the load sequence under study, whereas the last one is not subjected to sufficiently high loads.

Generally, the Weibull fracture probabilities of the particles depend nonlinearly on the overall strain and there are rapid increases of the P_{fr}^{j} in terms of the overall stress once the matrix has yielded. In addition, there is a marked dependence on the position of a given inclusion, indicating considerable inter-particle variations of the maximum principal stresses. Load redistribution effects upon fracture of a particle are predicted to be fairly complex. The first failure of a reinforcement (`B15`) leads to marked unloading of particle `B14`, which is a direct neighbor in loading direction and causes a very small increase of the failure probability of inclusion `A09`, which also is a close neighbor due to periodicity, but is somewhat offset. As a consequence, initial trends in fracture probability are changed and particle `A09` fails considerably earlier than `B14`. Failure of both particles `B15` and `A09` gives rise to small decreases of the fracture probability for particle `C01`, but increases for particle `D14`, both of which are situated relatively far away from the fractured inclusions. The latter reinforcement does not become critical for the loads considered here.

Particle Failure Triggered by the Monte Carlo Weibull Model (MCW)

As mentioned in chapter 3, the probabilistic behavior inherent in the MCW model causes it to give different results for each simulation run, see figure 25. Predictions for overall stress-strain diagrams are accordingly best obtained by averaging over a number of individual analyses. An example showing the averaged response of 10 runs using two different arrangements, A and B, is shown in figure 26, the result being a relatively smooth overall stress-strain curve, which shows a considerable loss in stiffness compared to the damage free case.

4.1.2 Uniaxial Loading of Microstructure AA2618/SiC$^{eq}_{15p}$-T4

The RSA-Unit Cells containing 15 spheres presented in section 3.1.2 are used for the FE-simulations presented in this section, adapted for a particle volume fraction of $\xi = 15\%$, see figures 12 and 14 (arrangements C and D).

In figure 27, which shows predictions for uniaxial loading in each of the three coordinate directions of the same particle arrangement, unit cell C, the dependence of the Weibull fracture probabilities on the particles' position in relation to neighbors is recognizable. In all three load cases the highest value of the fracture probability is attained for different particles (marked by yellow color). Nevertheless, this situation could change with increasing load, i.e. when additional regions between the particles yield, the stress transfer to the particles varies and another particle is the one with the highest fracture probability.

Figure 29 shows a prediction for the state after failure of some particles within model C (figure 28) at an overall strain of $\varepsilon^{\mathrm{a}} = 0.155$, obtained by loading in 2–direction and using the MCW method. A number of stress-strain curves predicted for the same unit cells are shown in figure 30, the runs leading to different results due to the use of the MCW algorithm to trigger particle failure. Each of the stress-strain responses shows the sudden reductions of the overall stress indicating particle failure. In analogy to figure 25 (averaged result of five different runs obtained by microstructure AA2618/SiC$^{eq}_{6.3p}$-T4) the effects of individual failure events are less marked in the ensemble averaged curve. With the averaging of three results a clear trend of the reduction in overall stress caused by particle failure is given, which for an overall applied tensile strain of $\varepsilon^{\mathrm{a}} = 0.22$ amounts to a reduction of about 5% compared to the damage free predictions.

In the following a more detailed discussion is given for the run corresponding to the

blue curve in figure 30, where at the end of the load history just two particles (inclusions number 2 and 3) of the unit cell have failed (for particle designations compare figure 12). Figure 31 shows a series of sections through inclusion 3 (the viewing direction is sketched in the bottom right corner of the figure), the first to fracture in this simulation. The maximum principal stresses are indicated in the form of a contour plot (legend is given) and an arrow plot (only the relative sizes and orientations of the arrows within each individual plot are relevant for the considerations here), corresponding to three overall loading conditions, two representing the predicted situation within the intact particle at different load states and the bottom one showing situation in the cracked particle.

In both plots showing states where the particle is intact some inhomogeneity of the stress field can be recognized. The general orientation of the maximum principal stresses before any particle cleavage, however, is as expected. The inclusion acts as a stress concentrator and the assumption of maximum principal stresses acting in perpendicular direction to the predefined crack plane (oriented here to lie parallel to the 1-3-plane) is fulfilled. The higher stress level in the lower left part of the section through the inclusion can be attributed to the influence of the closest neighbor, here inclusion 8. After particle failure the contour plot shows a totally changed situation, where increased stress gradients within the particle are present. Note the orientation of the maximum principal stresses, which are oriented almost tangentially to the particle surface close to the crack plane, but remain approximately normal to the particle surface elsewhere.

For this sequence additionally the relative movement of the particle, with respect to the particle's initial position (grey colored, the crack planes are schematically displayed as red lines), are depicted in the right column of figure 31. Beside the translation of the particle due to the overall deformation of the unit cell a noticeably rotation of the inclusion (the images are magnified five times) before damage can be seen. After cleavage each of the particle fragments is translated into loading direction and is further rotated, but, interestingly, the crack planes remain parallel.

The particle cracking model used here assumes the crack planes in the particles to be oriented normally to the averaged maximum principal stress in the particles, the orientations of which is approximated by the direction of the applied overall uniaxial stress. In this paragraph a closer look is taken on the orientations of the stress tensors in the particles.

The histograms given in figures 32 and 33 display the predicted distributions of the orientations of the maximum principal stresses (evaluated at the integration points) within the closely neighboring particles 3, 4 and 8, right before the failure of particle 3 and imme-

diately afterwards, respectively. The similarly distributed orientations before the failure event indicate that the conditions are very similar in these particles, the orientations of the maximum principal stresses overwhelmingly deviating from the global load direction by less than ten degrees (note that there is a tendency for the orientations of the maximum principal stresses to deviate to some extent from the overall loading direction close to the surface of the particles).

Interestingly, the failure of particle 3, while totally changing the situation in that inclusion, has little effect on the distributions of the orientations of the maximum principal stresses in the closest neighbors. The maximum principal stresses after particle cleavage, figure 31, bottom, show the highest values close to the particle-matrix interface, especially in the vicinity of the crack tip, which in this model is positioned in the immediately surrounding matrix region. The orientations of the maximum principal stresses remain approximately parallel near the poles of the particle, but are almost tangential to the interface closer to the crack.

A somewhat different picture emerges when the distributions of the magnitudes of the maximum principal stress distributions within the particles are considered. Before the failure of particle 3 the distributions are predicted to be very similar, see figure 34, even though some intra-particle variations of the stresses are evident. The failure of particle 3 can be seen in figure 35 to lead to some unloading of its closest neighbor, particle 8, while somewhat higher stresses are carried by the next nearest neighbor, particle 4. Interestingly, the inhomogeneity of the maximum principal stress is somewhat reduced in inclusion 8 and somewhat increased in 4. It is also noteworthy that failure does not lead to a total unloading of particle 3, parts of which continue to carry considerable loads.

Even though local failure by interfacial decohesion and by ductile damage of the matrix are not a primary topic of the studies reported here, it is possible to assess some of the effects of the brittle cleavage of a particle on the above damage modes by studying the microfields near the failed inclusion. Figure 36 shows a sequence of images corresponding to three global load states in the form of contour plots of the normal components (eqn. (3.19)) and of the magnitude of the tangential components (eqn. (3.20)) of the interfacial tractions acting on particle 3. The view orientation is the same as used in figure 31 (note, however, that the situation on the particle's surface and not in a section through the particle is shown). The highest tensile normal traction components are predicted in the regions of the particle's poles, whereas the equatorial regions are subjected to compressive normal interfacial tractions, for both the intact state and the failed state of the particle. With the load acting in the polar axis, the compressive normal tractions can be understood as a

consequence of the stiffness (and Poisson's ratio) mismatch between the constituents. The actual maximum values of the tensile normal tractions occur at positions slightly offset from the poles, evidently due to the proximity of neighboring particles and in accordance with the images showing the sections through the particle with maximum principal stress contour plots (figure 31). The tangential interfacial tractions also show perturbations due to neighboring particles, the details of their distributions, however, being different. The highest magnitudes of the tangential components predicted for this loading condition (applied strain $\varepsilon^a = 0.017$, corresponding to an overall stress of $\sigma^a = 301.8$ MPa) are found in ring-shaped regions at angles of approximately 45° from the direction of the applied load.

With the material data given in table 3 a ductile damage indicator, see eqn. (2.25), was evaluated for the matrix region surrounding the particle to obtain some data on matrix damage, see figure 37. The damage indicator, which can be interpreted only for the two states failure ($D = 1$) or no damage ($D = 0$) and not for states between these values, is depicted for the global tensile strain of $\varepsilon^a = 0.017$ ($\sigma^a = 301.8$ MPa) and confirms the above predictions by the maximum principal stress plots and the interfacial traction plots: the critical matrix regions in the vicinity of particles, on the one hand, are situated closely to the poles defined by the direction of the overall loads, and, on the other hand, preferentially occur at positions where there are close neighboring particles.

To give a more global view of regions susceptible to matrix damage, figure 38 shows all elements in which the damage indicator reaches a value of at least 0.90 in at least one integration point for the same conditions as figure 37, i.e. an overall uniaxial strain of $\varepsilon^a = 0.017$ acting in 2-direction. The very inhomogeneous distribution of initial matrix damage in a particle reinforced MMC is immediately evident.

The fact that figure 37 and 38 show initial matrix damage at a fairly low applied strain, which is in contradiction to the experimental result that damage in AA2618-T4 PRDMCs is initiated by particle failure, indicates that the material parameters available for the present study are not sufficiently realistic to capture the competition between the damage modes involved. Further inaccuracies may be due to the fact that the size of the load increments used may be rather coarse for integrating the damage indicator (which was a by-product of the analyses). Despite the lack of appropriate strength data it can be expected that with a full material damage model (including all three damage mechanisms) damage may be expected in this region quite early in the loading sequence, either within the interface, see figure 36, and/or in the closely neighboring matrix.

Accumulated Equivalent Plastic Strain in the Matrix

Figures 39 and 40 depict isosurfaces of the equivalent plastic strain for the same load state as studied in figures 37 and 38, i.e. $\varepsilon^{\mathrm{a}} = 0.017$ in 2-direction. For these conditions, the maximum value was evaluated as $\varepsilon_{\mathrm{eq,p}} = 0.165$, i.e. about ten times the macroscopic strain. In figure 39 only one isosurface is shown, that for $\varepsilon_{\mathrm{eq,p}} = 0.053$ (green). Evidently, for the relatively low overall plastic strains of the load state considered, the local plastic strains tend to be highest close to the particles, even though some regions of elevated plastic strains have also started to develop in the inter-particle matrix bridges. This becomes more evident in figure 40, top, where isosurfaces for equivalent plastic strains ranging from $\varepsilon_{\mathrm{eq,p}} = 0.031$ (light blue) to $\varepsilon_{\mathrm{eq,p}} = 0.053$ (green) are given. This plot also allows a contiguous region of elevated plastic strains to be discerned, which crosses the unit cell in loading direction. Such "tube-like" structures characterize the distribution of plastic strains at higher load levels (see also figure 65). Finally, figure 40, bottom, gives isosurfaces for $\varepsilon_{\mathrm{eq,p}} = 0.0006$ (dark blue). Interestingly, even though the overall stress of $\sigma^{\mathrm{a}} = 301.8$MPa is clearly in excess of the overall yield stress of the composite, considerable regions of the matrix remain elastic.

Interparticle Distances – Further Considerations

Even though it is known that the particle interaction in PRDMCs works in a rather complicated way, it appears worthwhile to discuss the evolution of damage within the periodically arranged unit cells by simply determining the geometrical distances between the particles. To evaluate the minimum widths of the matrix bridges between neighboring particles the interparticle distances must be computed for all unit cells and their periodic neighbors. Furthermore, a "virtual string" may be fixed at a certain particle position and connected to the corresponding partner particle position one period apart (in loading direction). Stretching the string to all other particle positions lying between the above chosen pair of particles in all possible combinations, leads to a number of different possible string lengths. Summing up all *interparticle* distances for such a string, that is the accumulated width of the matrix bridges within one particle arrangement period (=unit cell), doing this for all possible strings of the periodic unit cell arrangement, and comparing them to each other using their lengths gives at least one smallest value. In figure 41 the scheme of computing the interparticle distances is sketched on the basis of periodically arranged 2D unit cells and considering loading direction 1: for the example arrangement the interparticle distances within a "period" of the inclusion named 1 and 1' are $A_1 + A_2$, $B_1 + B_3$ and

$B_1 + B_2 + A_2$.

Particles lying on such a string with the shortest "matrix length with respect to the overall loading direction", are drawn in figure 42, different colors being used for the different loading directions. A comparison with figures 39 and 40 shows a clear correlation in that matrix damage appears more probable in regions of small interparticle distances in loading direction, where there are load paths in which there is a series of small interparticle distances. The predicted Weibull fracture probabilities for the same model composite, shown in figure 27, show a similar behavior. Note, however, that the Weibull fracture probabilities of particles embedded in a ductile matrix increase in a nonlinear and position dependent way with growing applied loads, so that different particles may have the maximum Weibull fracture probability during the load history even before the onset of damage.

Thus in the damage-free composite a clear tendency can be discerned for elevated local stress levels to occur along strings of particles that are closely spaced along the direction of an applied uniaxial stress. Such regions show a increased vulnerability to microscale damage in matrix, particles and interface. The above procedure tended to be quite successful in indicating regions susceptible to damage in the relatively small periodic phase arrangements considered in the present study. Its extension to larger unit cells or to nonperiodic microgeometries, however, is not clear.

4.1.3 Uniaxial Loading of Microstructure AA2618/SiC$^{bi}_{15\mathrm{p}}$-T4

For the investigations on MMCs with nonuniform particle sizes reported in this section the unit cell models `E` and `F`, see figures 13 and 15, were used. For the material properties of the constituents refer to table 3.

Loading the unit cell model `E` in 2-direction up to an applied strain of $\varepsilon^{\mathrm{a}} = 0.095$ and using `MCW` triggered particle failure resulted in the state shown in figure 43. Due to the cracking sequence the crack surfaces of the first failed particle, here `15`, are most widely separated. Note that all failed particles are big ones, `6`, `7`, and `15`. The matrix, see some regions on the unit cell's surface (regions `A` and `B` in figure 43), tends to be particularly highly strained in the neighborhood of the bigger particles. The apparent rising of some particles (region `A`) above the unit cell surface is due to this effect and to the periodicity of the unit cell, whereas the rising of the matrix region around particle `7` (which is positioned in this unit cell such that the crack plane is identical with the unit cell face) is caused by the failure of the particle.

Figure 44 compares the distributions of the maximum principal stresses evaluated for

all large and for all small particles at two applied uniaxial tensile loads. At a small load, where all particles remain intact and the matrix shows elastic behavior, the distributions of the maximum principal stresses are very similar, the one predicted for the smaller particles being slightly wider and shifted slightly to higher stresses. In the high strain regime the average of the maximum principal stresses can be seen to be higher for the small particles, some of the larger ones having failed by this time. In figure 45 the stress states in the large particles are shown in more detail for the latter state by separately evaluating the distributions of those particles which have failed and those which remain intact. While the latter particles clearly carry higher stresses, it can again be seen that substantial stresses are carried by the fractured reinforcements, in which, of course, there is a marked tail of the distributions of the maximum principal stresses towards lower values. In fact, small regions of the failed particles can be seen to be in hydrostatic compression, the maximum principal stress being negative.

It is noteworthy that for both stress states shown in figure 44 the small particles show higher stresses than the large ones. Due to the size sensitivity of the Weibull model, however, the fracture probabilities of the large particles are generally much higher. This is evident in figure 46, which shows the evolution of the Weibull fracture probabilities within each of the particles. In all cases the fracture probabilities of the large particles grow significantly faster than those of the small ones, particle positions effects playing a secondary role. Due to the differences in volume fraction, the failure of large particles also has a much larger effect on the overall stress-strain relations, see figure 47, where failure events of small particles occured for loading in 1- and 3-direction, but can hardly discerned.

Figures 48 to 51 show the magnitudes of the normal and tangential interfacial tractions at the particles' surfaces within the unit cell at four points in the loading history, in analogy to section 4.1.2. Generally the normal tractions are highest for all particles in their polar regions, the uniaxial macroscopic load being applied in the 1-direction. As in the case of equally sized particles, the maxima of the tangential tractions can be found in ring-shaped regions at angles of about 45º with respect to the loading directions, see figure 48. A trend can be discerned for perturbations due to the presence of neighboring particles to be more marked in the tangential than in the normal tractions.
The situation after the cleavage of one big particle and when some matrix regions have yielded is depicted in figure 49. Here the maxima of the normal tractions have shifted from the poles of some particles. This is clearly an effect of the particle positions within the unit cell. Furthermore, the maxima of the tangential tractions of the failed particle 7 are now positioned close to the crack, in contrast to the state before failure. The neighboring

inclusions seem to be hardly influenced by the failure of particle 7. Qualitatively similar predictions were attained for higher applied strains of $\varepsilon^{\mathrm{a}} = 0.095$, where the failure of particle 11, a small particle, has taken place, see figure 50, and for an applied strain of $\varepsilon^{\mathrm{a}} = 0.155$, where a third inclusion, particle 4, has failed, see figure 51. Interestingly, especially for small particles the positions of the maxima of the normal tractions tend to change under conditions of large scale matrix plasticity, see e.g. particle 2 (for numbering refer to figure 48) in figures 50 and 51.

Generally, for relatively soft matrix material such as aluminium, the failure of a particle tends to have only a very limited effect on the principal stress orientations within the closely neighboring particles. Evidently all variables of interest, such as the maximum principal stress in the particles, the interfacial tractions, and the equivalent plastic strain in the matrix show considerable inhomogeneity in all stress ranges, the effects being most marked in the highly plastic regime of the matrix. Finally, figure 52 shows results obtained from a uniaxial loading-unloading-sequence on the MMC AA2618/SiC$_{15\mathrm{p}}^{bi}$-T4 using the unit cell arrangement F (for particle designations refer to figure 15).

The sequence of particle cleavage events, which show up as reductions in the overall stress in the macroscopic stress-strain curve, can be seen from the numbers of the particles involved, the numbering scheme following figure 15. As mentioned earlier, there is a marked trend for large particles to fail before small ones. Nevertheless, the latter type of fracture event can occur with a significant probability, compare particles 8, 13, 12 in figure 52. However, the cleavage of a big particle, 15, reduces the composites' elastic modulus from initially $E^* = 87.6$ GPa to $E_{\mathrm{A}}^* = 83.7$ GPa, the corresponding generated pore volume fraction being $f_{\mathrm{A}} = 0.063\%$. The following two unloading-loading sequences result in overall elastic moduli of $E_{\mathrm{B}}^* = 75.5$ GPa (when four additional particles have failed), and $E_{\mathrm{C}}^* = 75.4$ GPa (no further particle failure occured). Approximating the failed particles by voids and using the Mori-Tanaka Method for calculating the corresponding stiffnesses, one obtains values of $E_{\mathrm{A}}^* = 82.0$ GPa, $E_{\mathrm{B}}^* = 70.8$ GPa and $E_{\mathrm{C}}^* = 70.8$ GPa. Noting that the Mori-Tanaka Method predicts the Young's modulus of the damage free material as $E^* = 87.6$ GPa, i.e. with excellent accuracy, the above results again show that broken particles continue to carry loads.

Focusing, for example, on the last load reversal (marked by C in figure 52), it is evident that a very small pore volume fraction of about 0.8% gives rise to a marked reduction in the overall stress of about 14% compared to the damage-free case. This behavior, which may be surprising at the first look, is due to the fact that all voids correspond to cracks within the stiff particles. These, of course, carry a high proportion of the applied load,

especially after large scale yielding of the matrix.

Within this simulation run the unloading processes were continued into the overall compressive range. Even though isotropic hardening was specified for the matrix, reverse plasticity occurred at relatively low compressive macrostresses, i.e. a pseudo-Bauschinger effect is present in the macroscopic material behavior. In addition, the fragments of previously failed particles approach more and more closely and may touch (note that overlapping of the fragments was precluded by the formulation of the node release algorithm), so they can carry compressive loads. Such a behavior was found for particle 4.

4.2 Simulation of HSS reinforced by M_xC_y-Particles

Modeled Material

The constituent material properties used in this section are listed in table 4. The material properties of the matrix and of the MC-type carbides designated here as `carbide A` correspond to those used in Plankensteiner [2000] for describing the matrix and the primary carbides in a S 6-5-2-5 HSS. These carbides are rather stiff and strong, similar to VC or TiC (see e.g. Miodownik [1994]). A second population of carbides is also considered in some of the models, designated as `carbide B` (table 4); these are rather softer and weaker, with material properties similar to those of M_6C and M_7C_3. (Note that similar material properties were used in studies of HSS by Gross-Weege *et al.* [1996] and Lippmann *et al.* [1996]). The elastoplastic behavior of the matrix, which is taken to include the effects of the secondary carbides, is described by J_2 plasticity plus a Ludwik hardening law, compare eqn. (3.8). Note that the above material models cause the predicted mechanical behavior of the HSS to be independent of particle size before the onset of particle failure.

Overview of Modeled Microstructures

A number of different types of microstructures are studied in order to allow some assessment of the influence of a number of parameters on the particle fracture behavior of HSS (compare table 11):

- HSS microstructure 1 ($\mathrm{HSS}^{\mu 1}_{6.3\%}$): stiff particles (e.g. VC- or TiC-carbides) of the same size, total particle volume fraction $\xi = 6.3$ vol.%.

- HSS microstructure 2 ($\mathrm{HSS}^{\mu 2}_{15\%}$): stiff particles (e.g. VC- or TiC-carbides) of the same size, total particle volume fraction $\xi = 15.0$ vol.%.

- HSS microstructure 3 ($\mathrm{HSS}^{\mu 3}_{15\%}$): soft particles (e.g. M_7C_3-carbides, M_6C-carbides) of the same size, total particle volume fraction $\xi = 15.0$ vol.%.

- HSS microstructure 4 ($\mathrm{HSS}^{\mu 4}_{15\%}$): larger stiff particles with smaller soft particles, total particle volume fraction $\xi = 15.0$ vol.%.

- HSS microstructure 5 ($\mathrm{HSS}^{\mu 5}_{15\%}$): larger soft particles with smaller stiff particles, total particle volume fraction $\xi = 15.0$ vol.%.

- HSS microstructure 6 ($\text{HSS}_{15\%}^{\mu 6}$): large and small stiff particles, total particle volume fraction $\xi = 15.0$ vol.%.

- HSS microstructure 7 ($\text{HSS}_{15\%}^{\mu 7}$): large and small soft particles, total particle volume fraction $\xi = 15.0$ vol.%.

- HSS microstructures 8/9 ($\text{HSS}_{15\%}^{\mu 8}/\text{HSS}_{15\%}^{\mu 9}$): soft and stiff particles of equal size in two different arrangements with slightly different volume fractions, total particle volume fraction $\xi = 15.0$ vol.%.

For all models a nominal reinforcement volume fractions of $\xi = 15.0$ vol.% was used with the exception of $\text{HSS}_{6.3\%}^{\mu 1}$, for which a nominal volume fraction of $\xi = 6.3$ vol.% was studied. For all of the computations on HSS-type materials the `MCW` particle cleavage activation model was used.

4.2.1 Microstructure $\text{HSS}_{6.3\%}^{\mu 1}$

For modeling microstructure $\text{HSS}_{6.3\%}^{\mu 1}$ the particles' material properties were set to `carbide A` (compare table 4). The case of $\xi = 6.3$ vol.% particles was investigated by `RPC`-unit cells. As expected, compared to the case of aluminium based particle reinforced MMCs, the particles are exposed to higher stresses and the likelihood of particle failure before the onset of large-scale yielding is increased. Figure 53 shows data obtained by sets of two simulations, each done with arrangement `A` (orange) and with arrangement `B` (green) as well as the averaged behavior obtained for all four runs (black). Both configurations show the same elastic modulus of $E^* \approx 219.7$ GPa (table 13), which is in good agreement with analytical estimates given in table 12.

Microscale stresses and strains obtained from models using unit cells `A` and `B` are listed in tables 13 and 14, for elastic and elastoplastic matrix states, respectively. The results are given in terms of phase averages $\pm$ the corresponding standard deviations. Only very small differences in the predictions are present (mainly in the standard deviations), which indicates that the unit cells follow very similar arrangement statistics in the damage free regime. In table 15 predictions for the phase averaged microfields are given for models incorporating particle failure, the applied strain being equal to that used in table 14. Slight reductions are present in the phase average of the equivalent plastic strain, but the plastic strains are much more inhomogeneous (as evident by the markedly increased standard deviations). This behavior is caused by the presence of high plastic strains in the vicin-

ity of the cracked particles (the cracks being assumed to be stopped in the matrix) in combination with some unloading in other regions. Note that such a marked increase of the fluctuations of the equivalent plastic strains was not found in "analogous" modeling runs for AA2618/SiC$_p$-T4 MMCs, see table 8, where particle fracture typically occurs at much higher average plastic strains in the matrix. The phase averages of $\sigma_{\text{eq}}^{(\text{m})}$, $\sigma_1^{(\text{m})}$, and $\sigma_{\text{H}}^{(\text{m})}$ are similar for models with and without particle fracture, with somewhat lower values predicted for the former case. As expected the failure of some carbides leads to a considerable reduction in the phase averages of the particle stresses, but to considerably higher standard deviations of the stress distributions. Because the different failure sequences in the modeling runs lead to a considerable difference in the overall stresses of arrangements A and B, there are also clear differences in the phase averaged particle stresses, especially in $\sigma_{\text{H}}^{(\text{p})}$, in table 15.

In table 16 stress measures averaged over the remaining intact particles at the same applied strain of $\varepsilon^{\text{a}} = 0.032$ are listed together with predictions for the volume fraction of the voids generated between the fragments of broken particles. Again markedly lower stress levels are found for arrangement A compared to arrangement B, even though the relative differences are slightly smaller than those shown by the phase averages in table 16. Especially noteworthy are the high standard deviations of the stress measures for the intact particles in arrangement A. The much higher pore volume fraction in the latter microgeometry can be conjectured to allow for the low phase averages of the mean stress noted above. For the matrix stresses only minor differences can be observed in table 15, but the accumulated equivalent plastic strains in the matrix with lower pore volume fraction are slightly increased. For the model with fewer failed particles at the overall strain of $\varepsilon^{\text{a}} = 0.032$ ($\frac{\sigma^{\text{a}}}{0\sigma_{\text{y}}^{(\text{m})}} = 1.08$, arrangement B) the values for the listed parameters show smaller standard deviations. Generally, it may be stated that the results for the two RPC arrangements are surprisingly difficult to interpret: whereas they lead to quite similar behavior in the damage free case, models A and B gave rather different predictions once particle failure was activated. From the limited number of simulation runs carried out it is not clear if these differences are statistically significant.

4.2.2   Microstructures $\text{HSS}_{15\%}^{\mu 2}$ and $\text{HSS}_{15\%}^{\mu 3}$

Microstructures $\text{HSS}_{15\%}^{\mu 2}$ and $\text{HSS}_{15\%}^{\mu 3}$ are based on the same microgeometries, which comprise 15 randomly positioned spherical particles of equal size, the volume fraction of each particle being 1% and the total nominal particle volume fraction 15%. For the simulations

arrangements created on the basis of the `RSA` approach and presented in figures 12 and 14 were used (i.e. arrangements `C` and `D`). The difference between the two microstructures lies in the different material properties employed for the carbides, stiff and strong particles (`carbide A`) being used in $\mathrm{HSS}^{\mu2}_{15\%}$, whereas for microstructures $\mathrm{HSS}^{\mu3}_{15\%}$ softer and weaker particles of type `carbide B` were specified. The latter microstructures show only a very small elastic contrast between matrix and carbides (compare table 4 for the material parameters).

The different stiffnesses of the particles in the two microstructures show up directly in the effective Young's moduli, which are predicted as 234 GPa for $\mathrm{HSS}^{\mu2}_{15\%}$ and 212 GPa for $\mathrm{HSS}^{\mu3}_{15\%}$, see table 18. Both values are in good agreement with the Hashin-Shtrikman type lower bounds given in table 17, the numerical results falling slightly below the bounds on account of the particle volume fraction in the unit cells being slightly lower than the nominal value of 15% due to meshing effects (see eqn. (3.14)). For a given applied strain in the elastic range, both the overall stresses and the phase averaged stresses are significantly higher in microstructure $\mathrm{HSS}^{\mu2}_{15\%}$ for both matrix and particles.
As expected, microstructure $\mathrm{HSS}^{\mu2}_{15\%}$ shows a stiffer overall response throughout the considered strain range, which reached to an applied strain $\varepsilon^{\mathrm{a}} = 0.032$ ($\frac{\sigma^{\mathrm{a}}}{_0\sigma_{\mathrm{y}}^{(\mathrm{m})}} = 1.15$), i.e. well into the elastoplastic range. At the latter strain the overall tensile stress carried by model $\mathrm{HSS}^{\mu2}_{15\%}$ exceeds that of model $\mathrm{HSS}^{\mu3}_{15\%}$ by about 1.3% (see table 26). For this applied strain both the phase averaged stresses in the particles and the equivalent plastic strain in the matrix are predicted to be significantly higher in model $\mathrm{HSS}^{\mu2}_{15\%}$, while the averaged stresses in the matrix are almost of the same value, despite the markedly higher standard deviation computed for model $\mathrm{HSS}^{\mu2}_{15\%}$, compare table 21.

In figure 54 predicted uniaxial stress-strain diagrams of microstructures $\mathrm{HSS}^{\mu2}_{15\%}$ and $\mathrm{HSS}^{\mu3}_{15\%}$ are shown, which were obtained by ensemble averaging over the results of simulation runs in which particle failure activated by the `MCW` method was considered. In both cases the first carbides were predicted to fail early in the loading history, especially so for model $\mathrm{HSS}^{\mu3}_{15\%}$, where the particle damage starts before yielding of the matrix (this, of course, is a consequence of the low strength of these particles). At the maximum strain considered, $\varepsilon^{\mathrm{a}} = 0.032$, all particles had failed in the simulation runs performed for model $\mathrm{HSS}^{\mu3}_{15\%}$, the stress carried at this point being reduced by more than 18% compared to the damage free case — in fact, they are lower than the yield stress of the unreinforced matrix ($\frac{\sigma^{\mathrm{a}}}{_0\sigma_{\mathrm{y}}^{(\mathrm{m})}} = 0.93$). Microstructure $\mathrm{HSS}^{\mu2}_{15\%}$ is less susceptible to particle fracture and at the above applied strain shows a reduction in the stress carried of some 11%, the overall stress being $\frac{\sigma^{\mathrm{a}}}{_0\sigma_{\mathrm{y}}^{(\mathrm{m})}} = 1.02$, compare also table 26.

The higher number of failed particles at the applied strain of $\varepsilon^{\mathrm{a}} = 0.032$ also has a marked influence on the microfields in microstructure $\mathrm{HSS}_{15\%}^{\mu 3}$, the phase average of the maximum principal stress for the particle phase being halved compared to the damage free case and the phase average of the mean stress being in the compressive rather than in the tensile range, see table 24. Similar, although much less marked effects are present for model $\mathrm{HSS}_{15\%}^{\mu 2}$. In both cases the high standard deviations of the stress measures indicate strongly fluctuating microstresses in the fractured particles, a behavior that was also evident in the studies of aluminium based MMCs, see e.g. figure 31. Interestingly, for model $\mathrm{HSS}_{15\%}^{\mu 2}$ both the averages and the standard deviations of the microstresses in those particles that have survived an applied strain of $\varepsilon^{\mathrm{a}} = 0.032$, see table 25, are comparable to the corresponding values evaluated from simulations in which damage was not activated (table 21), most of the differences between the two sets of results being consequences of the different overall stress levels obtained with and without damage. Table 25 also shows that the higher number of failed particles together with the earlier occurence of the failure events in the loading sequence leads to a significantly higher level of porosity in microstructure $\mathrm{HSS}_{15\%}^{\mu 3}$ at the reference overall strain of $\varepsilon^{\mathrm{a}} = 0.032$. This opening up of the voids between the fragments of fractured particles provides an explanation for the reduced levels of the phase averaged equivalent plastic strains in the matrix predicted for the simulation with particle damage (table 24) compared to the damage free cases (table 21) at the same applied strain.

Because of the similar material combinations the differences between the predictions attained for $\mathrm{HSS}_{15\%}^{\mu 2}$ and $\mathrm{HSS}_{6.3\%}^{\mu 1}$ (section 4.2.1) are just mentioned here with a few words. Of course, because the same number of particles per unit cell is used to describe a higher particle volume fraction, the failure of these particles in microstructure $\mathrm{HSS}_{15\%}^{\mu 2}$ has a greater impact on the overall stiffness of the material compared to arrangement $\mathrm{HSS}_{6.3\%}^{\mu 1}$. Due to the higher elastic stiffness of microstructure $\mathrm{HSS}_{15\%}^{\mu 2}$ with a carbide volume fraction of 15 vol.% compared to the case of $\xi = 6.3$ vol.%, somewhat higher phase averages of the stresses in matrix and carbides are reached at the same applied strain in the former material, compare tables 13 and 18. Not surprisingly, the higher reinforcement volume fraction also results in increased stresses and strains within the matrix when no failure is activated, compared to the situation predicted with the use of microstructure $\mathrm{HSS}_{6.3\%}^{\mu 1}$, see tables 18 and 19, at the same elastic strain. Sequential particle cleavage affects the results in such a way that the effective stresses, the maximum principal stresses and the hydrostatic stresses in the matrix have similar values in both microstructures (see tables 15 and 24), but the plastic strain is somewhat higher in microstructure $\mathrm{HSS}_{15\%}^{\mu 2}$. Averaging over

all particles (intact plus failed) results in approximately the same hydrostatic stresses as for the microstructure $\mathrm{HSS}^{\mu1}_{6.3\%}$, but their effective stresses and maximum principal stresses are smaller in $\mathrm{HSS}^{\mu2}_{15\%}$. The higher reinforcement volume fraction together with the higher number of fractured particles at the reference strain cause the pore volume between the fragments of fractured particles to be significantly larger in arrangement $\mathrm{HSS}^{\mu2}_{15\%}$, where it shows a value of $f_v = (0.43 \pm 0.05)$ %, compare table 25.

Generally it can be stated that reinforcement of the present very stiff matrix with relatively soft and weak particles as exemplified by microstructure $\mathrm{HSS}^{\mu3}_{15\%}$ is not an attractive proposition.

4.2.3 Microstructures $\mathrm{HSS}^{\mu4}_{15\%}$ and $\mathrm{HSS}^{\mu5}_{15\%}$

These two microstructures were specifically designed to shed some light on the influence of particle size and material properties on particle fracture. In both microstructures the same geometrical arrangements are used (arrangements E and F, see figures 13 and 15), which contain 7 large and 8 small randomly positioned spherical particles, the volumes of which differ by a factor of 8. In $\mathrm{HSS}^{\mu4}_{15\%}$ the large particles are of the stiff and strong ("hard") type, carbide A, and the small ones are softer and weaker, carbide B, whereas in $\mathrm{HSS}^{\mu5}_{15\%}$ the relationship between particle size and material properties is reversed, i.e. large soft and small stiff carbides. For the corresponding material parameters refer to table 4.

Because the total volume fraction of the small particles of approximately 2 vol.% only amounts to about 13% of the total particle volume fraction, the overall Young's modulus of microstructure $\mathrm{HSS}^{\mu4}_{15\%}$ (13 vol.% large stiff particles) is considerably higher at 230.5 MPa than that of $\mathrm{HSS}^{\mu5}_{15\%}$ (2 vol.% small stiff particles), which reaches only 214.6 MPa, compare table 18. This relationship between the two microstructures is continued into the elastoplastic range in the absence of microscale damage, the overall stresses carried at an applied strain of $\varepsilon^{\mathrm{a}} = 0.032$ being 3.15 GPa ($\frac{\sigma^{\mathrm{a}}}{_0\sigma_{\mathrm{y}}^{(\mathrm{m})}} = 1.15$) for $\mathrm{HSS}^{\mu4}_{15\%}$ and 3.12 GPa ($\frac{\sigma^{\mathrm{a}}}{_0\sigma_{\mathrm{y}}^{(\mathrm{m})}} = 1.14$) for $\mathrm{HSS}^{\mu5}_{15\%}$, see table 26.

As expected the averages of the stresses in particles and matrix for given applied strains are higher in $\mathrm{HSS}^{\mu4}_{15\%}$ in both the elastic and elastoplastic ranges (damage free cases) on account of the higher overall loads carried by that microstructure, see tables 18 and 21. Due to the greater volume fraction of stiffer particles the plastic strains in the matrix are slightly larger for $\mathrm{HSS}^{\mu4}_{15\%}$ in the elastoplastic regime. A more detailed picture on the stress states of the carbides can be obtained from tables 19 and 22, where separate averages and

standard deviations of the microstresses for the large and the small carbides are given. In both the elastic and the (damage-free) elastoplastic regimes the stiffer particles are more highly loaded in both microstructures. However, whereas in the elastic case the maxima of the averages of σ_{eq}, σ_1 and σ_H are obtained in the large stiff particles of $HSS_{15\%}^{\mu4}$, in the damage-free elastoplastic case the highest von Mises and maximum principal stresses occur in the small stiff particles of $HSS_{15\%}^{\mu5}$. Interestingly, the standard deviations of the stresses in the small particles are much higher than in the large ones for all cases considered, i.e. the small carbides show a marked tendency towards intra-particle and inter-particle stress fluctuations.

When damage due to particle fracture is activated, qualitatively different stress-strain responses are predicted for the two microstructures, see figures 55 and 56. For $HSS_{15\%}^{\mu4}$ the lower strength of particles of type `carbide B` slightly outweighs their smaller size for the material parameters and the Weibull model used, so that their fracture probabilities are somewhat higher than (but of comparable magnitude to) those of the large particles consisting of the stronger material, `carbide A`, see figure 57. As a consequence the smaller particles tend to fail first in simulation runs using the `MCW` fracture activation model and fracture events that involve large particles also occur throughout the strain range considered, see figure 55 (note that this figure shows results from two runs in which applied strains up to $\varepsilon^a = 0.032$ were reached and from one run in which applied strains of $\varepsilon^a = 0.052$ were modeled, by which time all of the 15 carbides had failed). In contrast to the above behavior, the Weibull fracture probabilities of the large weak particles in microstructure $HSS_{15\%}^{\mu5}$ are much in excess of those of the small strong ones, see figure 58. The big particles' fracture probabilities increase at all positions within the unit cell and for all loading directions, leading to a high propensity for particle fracture to occur before large scale yielding and, after their cleavage, no noticeable reinforcement effect by the small particles is present on account of their low volume fraction. This leads to a considerable reduction in the maximum load carried by microstructure $HSS_{15\%}^{\mu5}$ compared to $HSS_{15\%}^{\mu4}$. A further consequence of the early failure of large particles in $HSS_{15\%}^{\mu5}$ is the highest pore volume fraction at an applied strain of $\varepsilon^a = 0.032$ of all microstructures considered, see table 25.

An assessment of the phase averages and standard deviations of the microscale stresses and strains listed in table 24 leads to analogous conclusions as obtained for microstructures $HSS_{15\%}^{\mu2}$ and $HSS_{15\%}^{\mu3}$, i.e. the stresses carried by the failed particles are significantly reduced whereas the surviving particles continue to carry loads comparable to those predicted for the damage-free case. Due to the large contribution of the large particles to the total volume fraction, the stress and strain averages predicted for $HSS_{15\%}^{\mu4}$ and $HSS_{15\%}^{\mu2}$ are of comparable

magnitudes (table 21) for the damage free case and at the overall strain of $\varepsilon^{\mathrm{a}} = 0.032$. The same is valid for the phase averages obtained for the microstructures $\mathrm{HSS}_{15\%}^{\mu 5}$ and $\mathrm{HSS}_{15\%}^{\mu 3}$. When particle cleavage is activated, microstructure $\mathrm{HSS}_{15\%}^{\mu 5}$ shows predictions for the microfields that are quite similar to those obtained with $\mathrm{HSS}_{15\%}^{\mu 3}$, the main difference being somewhat higher phase averaged stresses in the former case. Evidently, the behavior of both microstructures is dominated by the large weak carbides (the total volume fractions of which are quite similar in both cases), the small stiff particles playing only a minor role. When microstructures $\mathrm{HSS}_{15\%}^{\mu 2}$ and $\mathrm{HSS}_{15\%}^{\mu 4}$ are compared, the presence of the small weak particles has clear consequences on the microfields despite their low volume fraction, this being a consequence of their considerable tendency to fail.

4.2.4 Microstructures $\mathrm{HSS}_{15\%}^{\mu 6}$ and $\mathrm{HSS}_{15\%}^{\mu 7}$

Microstructures $\mathrm{HSS}_{15\%}^{\mu 6}$ and $\mathrm{HSS}_{15\%}^{\mu 7}$ make use of the same particle arrangements as models $\mathrm{HSS}_{15\%}^{\mu 4}$ and $\mathrm{HSS}_{15\%}^{\mu 5}$, i.e. there are 7 large and 8 small randomly positioned spherical particles, refer to arrangements E and F, which are displayed in figures 13 and 15. In model $\mathrm{HSS}_{15\%}^{\mu 6}$ all of these particles are treated as stiff and strong MC-like carbides, whereas in model $\mathrm{HSS}_{15\%}^{\mu 7}$ they correspond to softer and weaker M_6C-like carbides.

As expected both the predicted Young's modulus and the phase averaged microstresses are very similar to the results obtained for microstructures $\mathrm{HSS}_{15\%}^{\mu 2}$ and $\mathrm{HSS}_{15\%}^{\mu 3}$, which contain carbides of the same material properties at very similar total volume fractions, all of which are of identical size. The same tendency is present for the microscale stresses and strains evaluated for uniaxial tensile loading into the elastoplastic range without particle damage, see table 21. For the elastic range table 19 shows that very similar stresses are carried by the large and the small particles at a given overall strain. For the damage-free elastoplastic case, however, a trend can be discerned in table 22 for the equivalent and maximum tensile stresses to be higher in the smaller particles. The trend towards higher stress fluctuations in the smaller particles noted in section 4.2.2 is again evident.

In the present series of unit cell studies, for particles of the same material behavior but of different sizes the larger particles always had larger fracture probabilities, leading to their preferential failure in MCW analyses. This behavior leads to responses of the type shown in figure 59, where stress-strain diagrams predicted for model $\mathrm{HSS}_{15\%}^{\mu 6}$ are displayed (some hardly noticeable decreases in the overall stress due to the failure of small particles are marked by *A*). The reduction in the stress carried compared to the damage-free microstructure, the stress-strain behavior of which is indicated by a dashed curve, is evident.

In figures 60 to 64 some aspects of uniaxial loading sequences consisting of loading-unloading-reloading processes are studied for models $\mathrm{HSS}^{\mu6}_{15\%}$ and $\mathrm{HSS}^{\mu7}_{15\%}$. Figure 60 shows results from a single `MCW` simulation run together with predictions from a damage-free analysis, both pertaining to microstructure $\mathrm{HSS}^{\mu6}_{15\%}$. Whereas in the damage free case the elastic modulus obtained for unloading from an overall applied strain of $\varepsilon^{\mathrm{a}} = 0.032$ is equal to the "initial" Young's modulus, damage due to the fracture of nearly 50% of all particles gives rise to a reduction in the elastic stiffness from about 233 GPa to about 184 GPa. The behavior of the reloading curve in the latter case, which deviates from a linear response before the flow stress is reached, is an artifact of the incrementation algorithm and should be disregarded in interpreting the results. In figure 63 an ensemble average of results obtained with the `MCW` algorithm for microstructure $\mathrm{HSS}^{\mu7}_{15\%}$ is given together with a prediction for the corresponding damage-free case. Failure events of small particles are marked by *B*. Again, the elastic response of the unit cells in the presence of particle damage is much softer than for the damage-free material (Young's moduli of 169 GPa versus 212 GPa). It is worth noting that the volume fraction of the voids between the particle fragments remains below 1% in both cases, which is much too small for explaining the reduction in elastic stiffness in the spirit of continuum damage mechanics of homogeneous materials.

In figure 62 a prediction for the evolution of the volume fraction of the voids between the fragments of broken particles in the course of the loading-unloading-reloading sequence is presented for microstructure $\mathrm{HSS}^{\mu6}_{15\%}$, an analogous plot for model $\mathrm{HSS}^{\mu7}_{15\%}$ being given in figure 64. In both cases there is a rapid initial increase of the pore volume fraction once particles start to break, followed by a slower void growth as the particle fragments are pulled apart. Whereas the former behavior is thought to approximate the behavior of actual materials reasonably well, the behavior in the growth phase is a consequence of the modeling assumption that cracks are stopped quickly in the matrix. Unloading leads to a reduction of the void volume fractions, but total closure of the voids is far from being achieved by reducing the overall stress to approximately zero.

Figure 61 follows the evolution of the "instantaneous" Weibull fracture probabilities in the particles of microstructure $\mathrm{HSS}^{\mu6}_{15\%}$ through the above loading sequence. During the initial tensile loading section the fracture probabilities of the large particles can be seen to be much higher than those of the small particles, stress redistribution effects upon the failure of some particles being fairly prominent. Unloading leads to a rapid reduction of the maximum principal stresses in the particles and, consequently, of the Weibull fracture probabilities, whereas reloading causes them to rise again to their former level. The loop

in the fracture probabilities of the surviving particles, e.g. particle 13 represented by a solid blue curve, which figures prominently in the diagram, is due to local plasticity effects. Overall unloading reduces the fracture probability of particle 13 to zero at some point, i.e. no substantial tensile stresses are present in the particle. Further unloading may lead to compressive microstresses in the particles, but does no longer affect the fracture probabilities. Upon reloading the particle carries tensile stresses again and the fracture probabilities rise, giving rise to the loops in figure 61. Because the incrementation scheme used was optimized for numerical efficiency rather than for resolving details of the evolution of the Weibull fracture probabilities, some care has to be exercised in interpreting the latter. Note that while the principal stresses in the particles decrease linearly during the (elastic) unloading sequence, the Weibull fracture probabilities, which scale as $P_{\mathrm{fr},j} \sim -\exp \sigma_1^m$, do not, even though such a behavior might be read from the few data points present in the loading-unloading region of figure 61.

For an applied overall strain of $\varepsilon^{\mathrm{a}} = 0.032$ particle failure leads to a reduction in the predicted overall stress about 21% for microstructure $\mathrm{HSS}_{15\%}^{\mu 7}$ (and about 15% for $\mathrm{HSS}_{15\%}^{\mu 6}$), compared to the damage-free case, see table 26. As expected, microstructure $\mathrm{HSS}_{15\%}^{\mu 7}$ also shows a rather high volume fraction of pores due to particle failure. As a consequence, the equivalent plastic strains are a little bit smaller in the above microstructure than in $\mathrm{HSS}_{15\%}^{\mu 6}$, and the microstresses are somewhat lower.

In figure 65 the predicted distributions of the accumulated equivalent plastic strain $\varepsilon_{\mathrm{eq,p}}$ in the damage-free model $\mathrm{HSS}_{15\%}^{\mu 7}$ at an applied strain of $\varepsilon^{\mathrm{a}} = 0.032$ (corresponding to an overall stress of $\sigma^{\mathrm{a}} = 3.12\mathrm{GPa}$) are visualized in terms of isosurfaces. Blue surfaces represent equivalent plastic strains of $\varepsilon_{\mathrm{eq,p}} = 0.023$. For the top image additional isosurfaces are colored dark green, $\varepsilon_{\mathrm{eq,p}} = 0.046$, and light green, corresponding to $\varepsilon_{\mathrm{eq,p}} = 0.069$. In the bottom image the highest value displayed is $\varepsilon_{\mathrm{eq,p}} = 0.031$, represented by the light blue isosurface, and between these two limiting values extra isosurfaces are depicted, with distance values differing in steps of $\varepsilon_{\mathrm{eq,p}} = 0.002$. With these images the formation of contiguous regions of elevated plastic strains in the matrix between the particles can be seen, which are oriented roughly parallel with the applied loads and pass through the unit cell. This is a qualitatively similar behavior to the one previously discussed for MMCs, but the load transfer to the particles is different due to the different material properties involved.

4.2.5 Microstructures $\text{HSS}_{15\%}^{\mu 8}$ and $\text{HSS}_{15\%}^{\mu 9}$

The final two microstructures considered, $\text{HSS}_{15\%}^{\mu 8}$ and $\text{HSS}_{15\%}^{\mu 9}$, are again based on the same microgeometries, in which there are 15 randomly positioned equally sized spherical particles of a total volume fraction of 15% (figures 12 and 14, arrangements C and D). Out of these particles 7 are randomly selected to form group one, which is assigned the material properties of stiff and strong carbides (`carbide A`) for model $\text{HSS}_{15\%}^{\mu 8}$ (marked with (h) in tables 20 and 23), the other 8 particles being softer and weaker (`carbide B`, marked with (w) in the tables). In microstructure $\text{HSS}_{15\%}^{\mu 9}$ the same sets of particles are given interchanged material properties, so that there are 7 vol.% of softer ((w)-designation in tables) and 8 vol.% of harder particles (marked by (h)).

The above assignments of material properties to the particles lead to predictions of a slightly smaller Young's modulus in model $\text{HSS}_{15\%}^{\mu 9}$, compare table 18. The homogenized uniaxial stress-strain response of the damage-free unit cells continues to be very similar in the elastoplastic range, see table 21, and there are only minor differences in the phase averages of the stresses and strains. The average stresses are higher in the stiffer particles both in the elastic (table 20) and the elastoplastic (table 23) regimes, the differences being more pronounced in the former case (interestingly, even though the total volume fractions of hard and soft particles are not the same for those microstructures the microscale stress averages are very similar for the elastoplastic case; even the standard deviations are the same and arrangement effects do not seem to be evident in the damage-free case, see tables). The data show that the effects of the particle stiffness tend to be more pronounced for the von Mises than for the hydrostatic stress contributions. In addition a tendency for a higher variability of the stresses in the stiffer particles can be discerned.

The results obtained when considering particle cleavage are illustrated in the stress-strain relations obtained for both microstructures, figure 66. For $\text{HSS}_{15\%}^{\mu 9}$ the overall stress at a strain of $\varepsilon^\text{a} = 0.032$ is reduced to $\sigma^\text{a} = 2.65\text{GPa}$ ($\frac{\sigma^\text{a}}{_0\sigma_\text{y}^{(\text{m})}} = 0.96$), the corresponding value for $\text{HSS}_{15\%}^{\mu 8}$ being 2.66GPa ($\frac{\sigma^\text{a}}{_0\sigma_\text{y}^{(\text{m})}} = 0.97$), see table 26.

Three snapshots of the distributions of the equivalent plastic strains in the matrix and of the maximum principal stresses in the particles are depicted in figures 68 to 70 for a typical `MCW`-triggered simulation run using microstructure $\text{HSS}_{15\%}^{\mu 9}$ (the corresponding stress-strain relation is shown in figure 67). The states correspond to applied strains of $\varepsilon_A^\text{a} = 0.010$ (where all particles remain intact), of $\varepsilon_B^\text{a} = 0.013$ (where the first nine particles have fractured), and of $\varepsilon_C^\text{a} = 0.032$ (the maximum applied strain considered

here), respectively.

At the lowest load level, the maximum principal stresses are consistently higher in the stiffer particles (yellow color coding) than in the softer ones (light green and dark green color coding) and a clear correlation between particle material and maximum principal stresses in the particles is evident. A first region with equivalent plastic strains in excess of $\varepsilon_{\text{eq,p}}^{(m)} = 0.0017$ can be seen to form between particles 2 and 14, both of which are of the stiffer type (particle set (h), refer to table 11). The irregular stress distributions on the face of particle 14 are an artifact of the mesh and constraint conditions used.

In figure 69, which pertains to a somewhat higher applied strain in which nine of the particles have failed (just one of the soft particles remains intact and three of the stiffer particles have also failed), such a clear distinction between stiffer and softer particles can no longer be made. Note that in those particles which happen to be sectioned by a face of the unit cell failure can be easily recognized by the low levels of the maximum principal stress in the interior (blue regions); as noted in figure 31 for the MMC model the zone close to the interface continues to carry considerable loads in fractured particles. In the matrix considerable regions with significant levels of plastic strains are evident. It is worth noting that the region where yielding was evident at a lower strain in figure 68 has grown noticeably (as evidenced by the blue isosurface of $\varepsilon_{\text{eq,p}}^{(m)} = 0.034$), and large scale but incomplete yielding has occured, forming a contiguous plastified region in the matrix (compare with the results shown for the damage-free MMC models in section 4.1.2). While the present results are too limited in scope to allow definite statements, it appears probable that this behavior is a consequence of the failure of some particles, which leads to high plastic strains in the matrix regions adjoining the crack tip (note that the cracks are assumed to be stopped in the matrix close to the particle). These trends are even more pronounced in figure 70, which shows the situation predicted for a considerably higher applied strain (predominantly yielded matrix, isosurfaces illustrating lower values of the equivalent plastic strain are not displayed).

4.3   General Discussion

In the preceding sections results on the mechanical behavior of two groups of particle reinforced ductile matrix composites were reported, special emphasis being put on the fracture of the reinforcing particles. Cube shaped unit cells were used, in which a number of spherical particles are dispersed, which represent SiC reinforcements in AA2618/SiC$_p$-T4 MMCs or primary carbides in high speed tool steels. A number of different microgeometries of this type were considered and, in the latter case, a number of variations in the carbides' material properties were studied.

As is well known from the literature, models of the above type give very good agreement with analytical estimates and bounds in the elastic range on the basis of the actual phase volume fractions in the discretized unit cell models. The material parameters of the constituents of the two groups differ in that the elastic contrast between the phases, i.e. the elastic stiffness mismatch between matrix and reinforcements, is about $\frac{E^{(\mathrm{p})}}{E^{(\mathrm{m})}} = 6.3$ for the MMC and lies between $\frac{E^{(\mathrm{p})}}{E^{(\mathrm{m})}} = 1.1$ and 2.1 for the HSS. Much higher contrasts in terms of instantaneous stiffnesses, of course, are present under conditions of large scale yielding in the matrix. As a consequence of the different degrees of material inhomogeneity in the two materials in the damage free case, the differences between the phase averaged stress levels in particles and matrix are generally more pronounced in the results obtained for AA2618/SiC$_p$-T4 than in those pertaining to HSS, compare tables 6 to 21. The absolute levels of the phase stresses, of course, are much higher in the high speed steel for a given macroscopic strain state. The more pronounced inhomogeneity of the AA2618/SiC$_p$-T4 MMCs also gives rise to a clear tendency towards higher standard deviations of the stresses in the reinforcement at the volume fractions considered, both interparticle and intraparticle stress fluctuations being increased.

The considerations of microscale damage concentrated on the brittle fracture of the reinforcing particle, whereas ductile damage of the matrix and decohesion at the interface between particles and matrix were not considered in depth in the models. The comparison of the relations of the characteristic strengths of the reinforcements, σ_0, to the matrix yield strengths, $^0\sigma_{\mathrm{y}}^{(\mathrm{m})}$, shows a significant difference in the investigated particle reinforced composites. Due to the much lower yield stress ($\frac{\sigma_0}{^0\sigma_{\mathrm{y}}^{(\mathrm{m})}} = 5.43$) of the AA2618-T4 matrix of the SiC/Al MMC the present Weibull fracture concept predicts that particles in this material have a low probability of failing before matrix yielding sets in (Eckschlager *et al.* [2001a]; Eckschlager and Böhm [2002]). In contrast, particle fracture events were found to be much more likely in the HSS ($\frac{\sigma_0}{^0\sigma_{\mathrm{y}}^{(\mathrm{m})}} = 1.33$), especially when weak (e.g. M$_7$C$_3$, M$_6$C,

$\frac{\sigma_0}{0\sigma_{\mathrm{y}}^{(\mathrm{m})}} = 0.65$) carbides are present. For materials of the latter type, in some simulation runs all particles failed at applied uniaxial tensile strains of less than $\varepsilon^{\mathrm{a}} = 0.032$, leading to decrease in the overall stress of up to 21% compared to the damage free case. In the SiC/Al MMC the number of failed particles at the maximum applied strain considered, $\varepsilon^{\mathrm{a}} = 0.22$, remained limited, but the loss in the macroscale stress carried by the material nevertheless reached up to 15%, the more marked concentration of the stresses in the particles of the MMC giving rise to a higher (relative) reduction in the overall stress per failed particle. Generally, these results reflect the much higher ductility of SiC/Al MMCs compared to high speed tool steels. It should be noted, however, that the above reductions in overall stress underestimate those occurring in actual materials, where ductile damage of the matrix and interfacial decohesion also contribute to the degradation of the overall material behavior.

In assessing the results obtained for the fracture behavior of carbides in HSS, where a number of combinations of relative particle size and of material property data sets for the carbides were considered, some special features of the microgeometries used must be taken into account. In the phase arrangements $\mathrm{HSS}_{15\%}^{\mu 2}$ to $\mathrm{HSS}_{15\%}^{\mu 9}$ a nominal particle volume fraction of 15% was attained from 15 spherical particles randomly positioned in the unit cell. Accordingly, in geometries with two particle sizes the small particles have about 23% and the larger about 184% each of the volume of each carbide in an arrangement with equally sized particles. Within the present Weibull framework these larger particles are the most liable ones to break for a given local load level. Even when this bias is accounted for, however, arrangements of equally sized strong particles ($\mathrm{HSS}_{15\%}^{\mu 2}$) tended to give the most favorable behavior, both the overall stress at the maximum strain and the number of fractured particles (which, of course, are focal points for the initiation and evolution of interface and matrix damage) remaining limited. Among materials that contain both strong and weak carbides, the best behavior tends to be obtained when the weaker particles are smaller, so that the fracture probabilities of both types of carbides are roughly comparable ($\mathrm{HSS}_{15\%}^{\mu 4}$). Within the present modeling approach the presence of large weak particles is always detrimental, many of them tending to fail early in the loading process, leading to a considerable level of damage even at relatively moderate applied loads.

Finally some interesting aspects of the microscale behavior of ductile matrices reinforced by spheres were found. Whereas in two-dimensional models the plastic strains in the matrix tend to concentrate in band-like regions angled at about 45° to the loading direction, a qualitatively different pattern of the microstrains was consistently predicted by the three-dimensional unit cells, in which contiguous regions of elevated plastic strain (which may

also enclose some particles) pass through the unit cell roughly aligned with the applied load. Also it was interesting to notice that even though the load carrying capability of broken particles is severely curtailed, they are nevertheless subject to rather high local shear stresses.

Chapter 5

Conclusions

Finite Element based three-dimensional multi-inclusion unit cell models were discussed, which allow studying the successive failure of a number of particulates due to brittle cleavage in particle reinforced ductile matrix materials such as MMCs and HSSs. The fracture of any given particle was controlled either deterministically via a Weibull-based Rankine fracture model or by a Monte-Carlo extension of the Weibull particle failure concept. Particle failure was assumed to take place instantaneously along a predefined fracture surface and was implemented via a node release technique. This modeling strategy allows to account for stress redistribution effects upon the failure of any particle in three-dimensional microgeometries. Results from computational runs on a number of simplified particle arrangements were presented as proof of concept.

To keep the complexity of the model at a reasonable level and to allow to concentrate directly on the effects of particle fracture, two central assumptions were made in the models. One of them is the use of periodic phase arrangements which is implicit with unit cell approaches and which automatically leads to periodic distributions of microscale damage. The other lies in neglecting ductile damage in the matrix and interfacial decohesion between particles and matrix, two damage mechanisms which in actual materials interact and compete with particle fracture.

Among the microgeometries used, randomly pruned cubic arrangements (section 3.1.1) are rather regular, but phase arrangements based on random sequential adsorption algorithms (section 3.1.2) allow realistic descriptions of statistically isotropic microgeometries, even though the number of particles per unit cell had to be limited to 15 on account of computational requirements. Both a Rankine type algorithm and a fully statistical cleavage

model for the particles implemented by triggering cleavage by Monte-Carlo-type procedures based on the Weibull fracture probabilities of each inclusion, were implemented. Performing a number of runs of the latter type for a given microgeometry and evaluating ensemble averaged stress vs. strain diagrams reduces the effect of each individual particle failure event on the predicted overall response, leading to more realistic results. The microscale stress and strain fields in the unit cells were evaluated by the Finite Element method, which also provided a convenient platform for implementing the particle fracture model. The use of a continuum mechanical description essentially implies that all physical mechanisms acting on smaller length scale, such as the interaction of dislocations with small dispersoids in the matrix, are considered to be subsumed in the constitutive descriptions of the constituents.

The investigations are intensively discussed in section 4.1 regarding the MMC SiC/AA2618-T4, where microgeometries with equally sized particles of different total particle volume fraction as well as microgeometries with bidispersely sized particles are treated, and in section 4.2 for the HSS, where a number of variations of reinforcement material properties and particle sizes are presented. General trends are summarized in section 4.3. As is well known, for the damage-free case due to the higher stiffness of the particles compared to the matrix a reinforcing effect results because of the increased load carried by the particles. With the Weibull based models used in the present work a clear size dependence of the brittle fracture of the particles is found: bigger particles have a higher probability of failing and, in addition, give rise to larger flaws in the material upon failure. This influence becomes more significant, when the stiffness mismatch between matrix and reinforcement phase is higher (for MMCs compare sections 4.1.2 with 4.1.3, for HSS microgeometries $HSS_{15\%}^{\mu2}$ with $HSS_{15\%}^{\mu6}$, or $HSS_{15\%}^{\mu3}$ with $HSS_{15\%}^{\mu7}$, refer to section 4.2). Experiments on similar materials, albeit at higher total particle volume fraction, support a size effect in which the composite yield stress decreases with increasing particle size, see Kouzeli *et al.* [2001]. If two reinforcement phases are present, the effect on the particle failure probability strongly depends on their respective material properties. For example, a combination of large strong particles with weaker smaller ones may have the consequence that the fracture probabilities of small and big particles may lie in the same range up to the first particle failure, see the results in section 4.2.3.

The main practical difficulty with the present modeling approach lies in its high computational costs, so that improvements of the numerical efficiency of the algorithms are clearly of interest. For improved realism it may be worthwhile not to use predefined fracture planes, but to generate appropriate fracture surfaces before failure, so influences of the

stress state at the particles in question on their orientation and position can be accounted for.

Future work is planned, on the one hand, to include modeling of the other failure modes of the composite. On the other hand, it is important to study phase arrangements that contain higher numbers of particles to obtain more realistic descriptions of actual materials. Other long term goals are to account for more general particle shapes and for the presence specific cleavage planes in monocrystalline particles. Furthermore, the influence of thermal residual stresses on the failure of PRDMCs is of considerable interest.

Tables

Table 1: Chemical composition of AA2618-T4 (following the **I**nternational **A**lloy **D**esignation **S**ystem (IADS)), which is used as matrix material in modeling MMCs in the present work (Polmear [1995]).

grade	Si	Fe	Cu	Mg	Zn	Ti	Ni
Al2618	0.10–0.25	0.9–1.3	1.9–2.7	1.3–1.8	0.10	0.04–0.10	0.9–1.2
T4	solution treatment, quenching and natural ageing						

Table 2: Chemical composition of a typical representative of a conventionally produced high speed steel S 6-5-2-5 (Böhler S705), its primary metallic carbides, and its martensitic–austenitic steel matrix (as–hardened) and of a powder metallurgically produced HSS (S390 Isomatrix). Data (in wt.%) estimated by Böhler (compare Antretter [1998]; Plankensteiner [2000]).

grade		C	Cr	W	Mo	V	Co	Fe
S 6-5-2-5		0.92	4.2	6.1	4.9	1.9	5.1	*balance*
	MC	14.0	4.0	21.0	12.0	45.0	—	4.0
	M_2C	6.0	8.0	40.0	28.0	12.0	—	6.0
	M_6C	2.0	4.0	35.0	20.0	3.0	—	36.0
	Matrix	0.64	4.2	2.7	2.8	1.1	5.1	*balance*
S390 Isomatrix		1.6	4.8	10.5	2.0	5.0	8.0	*balance*

Table 3: Material parameters used for modeling AA2618/SiC$_p$-T4 MMCs (modified Ludwik hardening law) and elastic reinforcements (SiC, compare LLorca and González [1998]; LLorca and Poza [1995]).

	E [GPa]	ν [1]	${}^0\sigma_{\mathrm{y}}^{(\mathrm{m})}$ [MPa]	h [MPa]	n [1]	m [1]	σ_0 [GPa]	V_0 [1]	ε_0 [1]
Al2618-T4 matrix	70	0.30	184	722.7	0.49	—	—	—	0.2
reinforcement	450	0.17	—	—	—	3.0	1.0	0.01	–

Table 4: Material parameters used for modeling HSS (modified Ludwik hardening law) and elastic carbidic inclusions.

	E [GPa]	ν [1]	${}^0\sigma_{\mathrm{y}}^{(\mathrm{m})}$ [GPa]	h [GPa]	n [1]	m [1]	σ_0 [GPa]	V_0 [1]	ε_0 [1]
HSS matrix (Plankensteiner [2000])	210	0.30	2.75	1.5	0.5	—	—	—	0.1 (Lippmann [1995])
Carbides A (Plankensteiner [2000])	450	0.25	—	—	—	5.0	3.66	0.01	—
Carbides B	225	0.25	—	—	—	5.0	1.80	0.01	—

Table 5: Analytical predictions for overall and microscale elastic responses of Al2618-T4 reinforced by SiC (15 particles) subjected to a uniaxial tensile strain of $\varepsilon^{\mathrm{a}} = 0.0005$. The Mori-Tanaka method (MTM) was used for evaluating lower (LB) and upper bounds (UB), with the former corresponding to the standard Mori-Tanaka estimates (note that phase averaged stresses are estimates, not bounds). For constituent material properties used see table 3.

		E^* [GPa]	ν^* [$\times 10^{-1}$]	$\sigma_{\mathrm{eq}}^{(\mathrm{m})}$ [MPa]	$\sigma_{1}^{(\mathrm{m})}$ [MPa]	$\sigma_{\mathrm{H}}^{(\mathrm{m})}$ [MPa]	$\sigma_{\mathrm{eq}}^{(\mathrm{p})}$ [MPa]	$\sigma_{1}^{(\mathrm{p})}$ [MPa]	$\sigma_{\mathrm{H}}^{(\mathrm{p})}$ [MPa]
LB	6.3 vol.%	76.9	2.94	36.56	36.88	12.51	66.54	61.80	17.45
UB		84.39	2.90						
LB	15.0 vol.%	87.58	2.87	38.99	39.78	13.78	70.96	66.53	19.22
UB		105.51	2.79						

Table 6: Numerical predictions for overall and microscale elastic responses of Al2618-T4 reinforced by SiC (15 particles) subjected to a uniaxial tensile strain of $\varepsilon^{\mathrm{a}} = 0.0005$. Particles are uniformly sized (arrangement `A`, arrangement `B`, arrangement `C`) or bidispersely sized (arrangement `E`). Microstresses are given as phase averages $\pm$ standard deviations. For the constituent material properties used see table 3.

$\mathrm{vol.\%}/_{\mathrm{arr.}}$	E^* [GPa]	ν^* [$\times 10^{-1}$]	$\sigma_{\mathrm{eq}}^{(\mathrm{m})}$ [MPa]	$\sigma_{1}^{(\mathrm{m})}$ [MPa]	$\sigma_{\mathrm{H}}^{(\mathrm{m})}$ [MPa]	$\sigma_{\mathrm{eq}}^{(\mathrm{p})}$ [MPa]	$\sigma_{1}^{(\mathrm{p})}$ [MPa]	$\sigma_{\mathrm{H}}^{(\mathrm{p})}$ [MPa]
$^{6.3}/_{\mathrm{A}}$	76.78	2.95/2.93	36.4 ± 4.0	36.7 ± 5.5	12.5 ± 3.1	68.1 ± 4.6	62.5 ± 4.3	17.2 ± 1.7
$^{6.3}/_{\mathrm{B}}$	76.78	2.94/2.94	36.4 ± 4.1	36.7 ± 5.5	12.5 ± 3.1	68.0 ± 4.7	62.5 ± 4.3	17.2 ± 1.9
$^{15.0}/_{\mathrm{C}}$	87.41	2.85/2.87	39.7 ± 6.9	39.9 ± 8.7	13.7 ± 4.5	72.3 ± 7.3	67.6 ± 6.8	19.4 ± 2.7
$^{15.0}/_{\mathrm{E}}$	86.75	2.87/2.87	39.7 ± 6.5	39.9 ± 8.3	13.7 ± 4.4	70.8 ± 4.6	66.0 ± 4.2	18.9 ± 1.9

Table 7: Numerical predictions for the microscale elastoplastic responses of Al2618-T4 reinforced by SiC (15 particles) subjected to a uniaxial tensile strain of $\varepsilon^{\mathrm{a}} = 0.22$ (predominantly yielded matrix, for corresponding homogenized stresses see table 10), particle failure being suppressed. Particles are uniformly sized (arrangement A, arrangement B, arrangement C) or bidispersely sized (arrangement E). For the constituent material properties used see table 3.

vol.% / arr.	$\varepsilon_{\mathrm{eq,p}}^{(\mathrm{m})}$ $[\times 10^{-1}]$	$\sigma_{\mathrm{eq}}^{(\mathrm{m})}$ [GPa]	$\sigma_{1}^{(\mathrm{m})}$ [GPa]	$\sigma_{\mathrm{H}}^{(\mathrm{m})}$ [GPa]	$\sigma_{\mathrm{eq}}^{(\mathrm{p})}$ [GPa]	$\sigma_{1}^{(\mathrm{p})}$ [GPa]	$\sigma_{\mathrm{H}}^{(\mathrm{p})}$ [GPa]
$6.3/$A	2.06 ± 0.47	0.51 ± 0.04	0.52 ± 0.21	0.19 ± 0.21	1.34 ± 0.33	0.99 ± 0.20	0.13 ± 0.16
$6.3/$B	2.06 ± 0.46	0.51 ± 0.04	0.52 ± 0.21	0.19 ± 0.20	1.33 ± 0.35	0.98 ± 0.21	0.12 ± 0.16
$15.0/$C	2.39 ± 0.81	0.54 ± 0.06	0.55 ± 0.19	0.21 ± 0.18	1.16 ± 0.14	0.93 ± 0.11	0.16 ± 0.07
$15.0/$E	2.39 ± 0.70	0.54 ± 0.05	0.55 ± 0.22	0.21 ± 0.20	1.17 ± 0.15	0.92 ± 0.11	0.15 ± 0.09

Table 8: Numerical predictions for the microscale elastoplastic responses of Al2618-T4 reinforced by SiC (15 particles) subjected to a uniaxial tensile strain of $\varepsilon^{\mathrm{a}} = 0.22$ (predominantly yielded matrix, for corresponding homogenized stresses see table 10) and after the cleavage of some particles during the loading process. Particles are uniformly sized (arrangement A, arrangement B, arrangement C) or bidispersely sized (arrangement E). For the constituent material properties used see table 3. Note that the overall stresses carried by the material are somewhat lower than in table 7.

vol.% / arr.	$\varepsilon_{\mathrm{eq,p}}^{(\mathrm{m})}$ $[\times 10^{-1}]$	$\sigma_{\mathrm{eq}}^{(\mathrm{m})}$ [GPa]	$\sigma_{1}^{(\mathrm{m})}$ [GPa]	$\sigma_{\mathrm{H}}^{(\mathrm{m})}$ [GPa]	$\sigma_{\mathrm{eq}}^{(\mathrm{p})}$ [GPa]	$\sigma_{1}^{(\mathrm{p})}$ [GPa]	$\sigma_{\mathrm{H}}^{(\mathrm{p})}$ [GPa]
$6.3/$A	2.05 ± 0.44	0.51 ± 0.04	0.51 ± 0.19	0.18 ± 0.19	1.09 ± 0.38	0.73 ± 0.40	0.03 ± 0.03
$6.3/$B	2.04 ± 0.48	0.51 ± 0.04	0.51 ± 0.21	0.18 ± 0.20	1.16 ± 0.47	0.78 ± 0.44	0.03 ± 0.03
$15.0/$C	2.31 ± 0.96	0.53 ± 0.06	0.54 ± 0.22	0.20 ± 0.21	1.12 ± 0.35	0.82 ± 0.35	0.10 ± 0.24
$15.0/$E	2.28 ± 0.69	0.53 ± 0.06	0.54 ± 0.25	0.20 ± 0.24	0.96 ± 0.44	0.64 ± 0.42	0.03 ± 0.26

Table 9: Continuation of table 8: Numerical predictions for the microscale elastoplastic responses of the remaining intact SiC reinforcements (Al2618-T4 reinforced by SiC (15 particles)) subjected to a uniaxial tensile strain of $\varepsilon^{\mathrm{a}} = 0.22$ (predominantly yielded matrix, for corresponding homogenized stresses see table 10) and after the cleavage of some particles during the loading process. Additionally, for this overall strain the evaluated average overall pore volume fraction due to particle cleavage is given. Particles are uniformly sized (arrangement A, arrangement B, arrangement C) or bidispersely sized (arrangement E).

vol.% $/$ arr.	$\sigma_{\mathrm{eq}}^{(intact)}$ [GPa]	$\sigma_1^{(intact)}$ [GPa]	$\sigma_{\mathrm{H}}^{(intact)}$ [GPa]	f_v [%]
$^{6.3}/_{\mathrm{A}}$	1.12 ± 0.26	0.93 ± 0.18	0.14 ± 0.15	0.43 ± 0.20
$^{6.3}/_{\mathrm{B}}$	1.19 ± 0.45	0.81 ± 0.41	0.05 ± 0.28	0.64 ± 0.15
$^{15.0}/_{\mathrm{C}}$	1.17 ± 0.14	0.91 ± 0.11	0.15 ± 0.09	1.00 ± 0.14
$^{15.0}/_{\mathrm{E}}$	1.13 ± 0.19	0.86 ± 0.18	0.12 ± 0.10	1.18 ± 0.32

Table 10: Predicted overall stresses at an overall uniaxial tensile strain of $\varepsilon^{\mathrm{a}} = 0.22$ for AA2618/SiC$_p$-T4 (predominantly yielded matrix). Values are given, first, for the case when no particle failure is present, and, second, for analyses where particle failure is activated (averages of at least two simulations). See table 3 for the material properties used.

vol.% $/$ arr.	$\sigma_{(\text{failure suppressed})}^{\mathrm{a}}$ [GPa]	$\dfrac{\sigma_{(\text{failure suppressed})}^{\mathrm{a}}}{^0\sigma_{\mathrm{y}}^{(\mathrm{m})}}$ [1]	$\sigma_{(\text{failure activated})}^{\mathrm{a}}$ [GPa]	$\dfrac{\sigma_{(\text{failure activated})}^{\mathrm{a}}}{^0\sigma_{\mathrm{y}}^{(\mathrm{m})}}$ [1]
$^{6.3}/_{\mathrm{A}}$	0.547	2.98	0.518 ± 0.005	2.82
$^{6.3}/_{\mathrm{B}}$	0.546	2.97	0.526 ± 0.008	2.86
$^{15.0}/_{\mathrm{C}}$	0.596	3.24	0.565 ± 0.009	3.07
$^{15.0}/_{\mathrm{E}}$	0.593	3.23	0.521 ± 0.039	2.83

Table 11: List of the variations of constituents and microgeometry (equally sized particles, particles of two different sizes) considered in modeling HSS. The unit cells and phase arrangments are presented in section 3; nominal volume fraction data are given in volume percent. For designations of inclusions see figures 11 for the models marked by [a], figures 12 and 14 for the models marked by [b] and figures 13 and 15 for the models marked by [c], respectively. In the "inclusions" column the carbides are additionally marked with (b), representing big inclusions, and with (s), representing small inclusions, for the case of bidispersely sized inclusion models. For microstructures $\mathrm{HSS}^{\mu 8}_{15\%}$ and $\mathrm{HSS}^{\mu 9}_{15\%}$ the designations name certain inclusion sets of certain material properties, namely (h) for hard and strong particles, and (w) for weak and soft, respectively. For material data refer to table 4.

micro-	matrix elements	inclusions[a),b)]	
structure – unit cell (`arr.`)	material – vol.%	material – vol.%	material – vol.%
$\mathrm{HSS}^{\mu 1}_{6.3\%}$– `RPC`^{eq} (`A,B`)[a)]	HSS – 93.7%	carbide A – 6.3%	
$\mathrm{HSS}^{\mu 2}_{15\%}$– `RSA`^{eq} (`C,D`)[b)]	HSS – 85.0%	carbide A – 15.0%	
$\mathrm{HSS}^{\mu 3}_{15\%}$– `RSA`^{eq} (`C,D`)[b)]	HSS – 85.0%	carbide B – 15.0%	
$\mathrm{HSS}^{\mu 4}_{15\%}$– `RSA`^{bi} (`E,F`)[c)]	HSS – 85.0%	carbide A – 13.0% (b)	carbide B – 2.0% (s)
$\mathrm{HSS}^{\mu 5}_{15\%}$– `RSA`^{bi} (`E,F`)[c)]	HSS – 85.0%	carbide B – 13.0% (b)	carbide A – 2.0% (s)
$\mathrm{HSS}^{\mu 6}_{15\%}$– `RSA`^{bi} (`E,F`)[c)]	HSS – 85.0%	carbide A – 13.0% (b)	carbide A – 2.0% (s)
$\mathrm{HSS}^{\mu 7}_{15\%}$– `RSA`^{bi} (`E,F`)[c)]	HSS – 85.0%	carbide B – 13.0% (b)	carbide B – 2.0% (s)
$\mathrm{HSS}^{\mu 8}_{15\%}$– `RSA`^{eq} (`C,D`)[b)]	HSS – 85.0%	carbide A – 7.0% (h)	carbide B – 8.0% (w)
$\mathrm{HSS}^{\mu 9}_{15\%}$– `RSA`^{eq} (`C,D`)[b)]	HSS – 85.0%	carbide B – 7.0% (w)	carbide A – 8.0% (h)

Table 12: Microstructure $\text{HSS}^{\mu 1}_{6.3\%}$: Analytical predictions for overall and microscale elastic responses of HSSs ($\xi = 6.3$ vol.% nominal) subjected to a uniaxial tensile strain of $\varepsilon^{\text{a}} = 0.0005$. The Mori-Tanaka method (MTM) was used for evaluating lower (LB) and upper bounds (UB), with the former corresponding to the standard Mori-Tanaka estimates (note that phase averaged stresses are estimates, not bounds). The particles are spheres of type `carbide A` (see table 4 for constituent material properties).

	E^*	ν^*	$\sigma_{\text{eq}}^{(\text{m})}$	$\sigma_1^{(\text{m})}$	$\sigma_{\text{H}}^{(\text{m})}$	$\sigma_{\text{eq}}^{(\text{p})}$	$\sigma_1^{(\text{p})}$	$\sigma_{\text{H}}^{(\text{p})}$
	[GPa]	[$\times 10^{-1}$]	[MPa]	[MPa]	[MPa]	[MPa]	[MPa]	[MPa]
LB	219.98	2.969	107.25	107.73	36.23	150.79	143.60	43.07
UB	221.44	2.963						

Table 13: Microstructure $\text{HSS}^{\mu 1}_{6.3\%}$: Numerical predictions for overall and microscale elastic responses of HSSs ($\xi = 6.3$ vol.% nominal, 15 particles, arrangements `A` and `B`) subjected to a uniaxial tensile strain of $\varepsilon^{\text{a}} = 0.0005$. Carbides are uniformly sized spheres of type `carbide A` (see table 4 for constituent material properties).

arr.	E^*	ν^*	$\sigma_{\text{eq}}^{(\text{m})}$	$\sigma_1^{(\text{m})}$	$\sigma_{\text{H}}^{(\text{m})}$	$\sigma_{\text{eq}}^{(\text{p})}$	$\sigma_1^{(\text{p})}$	$\sigma_{\text{H}}^{(\text{p})}$
	[GPa]	[$\times 10^{-1}$]	[MPa]	[MPa]	[MPa]	[MPa]	[MPa]	[MPa]
A	219.71	$^{2.972}/_{2.967}$	106.7 ± 5.7	107.3 ± 7.7	36.2 ± 4.4	152.0 ± 4.7	144.0 ± 4.2	42.7 ± 1.7
B	219.71	$^{2.971}/_{2.967}$	106.7 ± 5.8	107.2 ± 7.9	36.2 ± 4.3	151.9 ± 4.6	143.9 ± 4.3	42.7 ± 2.0

Table 14: Microstructure $\text{HSS}^{\mu 1}_{6.3\%}$: Numerical predictions for the microscale elastoplastic responses of HSSs ($\xi = 6.3$ vol.% nominal, 15 particles, arrangements A and B) subjected to a uniaxial tensile strain of $\varepsilon^{\text{a}} = 0.032$ (predominantly yielded matrix, for corresponding homogenized stresses see table 26). The uniformly sized particles are of type `carbide A`, see table 4, and particle cleavage was suppressed.

arr.	$\varepsilon^{(m)}_{eq,p}$ $[\times 10^{-2}]$	$\sigma^{(m)}_{eq}$ [MPa]	$\sigma^{(m)}_{1}$ [MPa]	$\sigma^{(m)}_{H}$ [MPa]	$\sigma^{(p)}_{eq}$ [MPa]	$\sigma^{(p)}_{1}$ [MPa]	$\sigma^{(p)}_{H}$ [MPa]
A	1.87 ± 0.49	2.95 ± 0.03	2.97 ± 0.31	1.02 ± 0.29	5.04 ± 0.30	4.18 ± 0.26	0.83 ± 0.13
B	1.87 ± 0.47	2.95 ± 0.03	2.97 ± 0.31	1.02 ± 0.29	5.02 ± 0.31	4.15 ± 0.26	0.81 ± 0.14

Table 15: Microstructure $\text{HSS}^{\mu 1}_{6.3\%}$: Unit cell predictions for the microscale elastoplastic responses of HSSs ($\xi = 6.3$ vol.% nominal, 15 particles of type `carbide A`, see table 4, arrangements A and B) subjected to a uniaxial tensile strain of $\varepsilon^{\text{a}} = 0.032$ (for corresponding homogenized stresses see table 26), a number of particles having failed.

arr.	$\varepsilon^{(m)}_{eq,p}$ $[\times 10^{-2}]$	$\sigma^{(m)}_{eq}$ [GPa]	$\sigma^{(m)}_{1}$ [GPa]	$\sigma^{(m)}_{H}$ [GPa]	$\sigma^{(p)}_{eq}$ [GPa]	$\sigma^{(p)}_{1}$ [GPa]	$\sigma^{(p)}_{H}$ [GPa]
A	1.80 ± 1.04	2.92 ± 0.06	2.94 ± 0.39	1.00 ± 0.36	4.08 ± 1.09	3.03 ± 1.47	0.34 ± 0.93
B	1.83 ± 0.82	2.95 ± 0.05	2.95 ± 0.35	1.01 ± 0.32	4.58 ± 0.92	3.65 ± 1.23	0.61 ± 0.74

Table 16: Continuation of table 15: Microscale responses averaged over all intact particles after tensile loading of HSSs ($\xi = 6.3$ vol.% nominal, arrangments A and B) up to a uniaxial strain of $\varepsilon^{\text{a}} = 0.032$, a number of particles having failed (for corresponding homogenized stresses see table 26). Additionally, for this overall strain the evaluated average overall pore volume fraction caused by particle cleavage is given.

arrangement	$\sigma^{(intact)}_{eq}$ [GPa]	$\sigma^{(intact)}_{1}$ [GPa]	$\sigma^{(intact)}_{H}$ [GPa]	f_v [%]
A	4.59 ± 0.71	3.77 ± 0.89	0.72 ± 0.51	0.19 ± 0.02
B	4.96 ± 0.30	4.18 ± 0.30	0.88 ± 0.18	0.09 ± 0.01

Table 17: Analytical predictions for overall and microscale elastic responses of HSSs ($\xi = 0.15$ nominal) subjected to an uniaxial tensile strain of $\varepsilon^{\mathrm{a}} = 0.0005$. For microstructures $\mathrm{HSS}^{\mu 2}_{15\%}$ and $\mathrm{HSS}^{\mu 3}_{15\%}$ the MT-method has been used to evaluate lower (LB) and upper (UB) Hashin Shtrikman-type bounds, with the standard MT-estimates corresponding to the former (note that phase averaged stresses are estimates, not bounds). For the other microstructures the standard MT-estimates are given. In the three-phase cases the reinforcement stresses are given separately. For the microstructures with equal sized spheres the superscripts (h), for hard and strong, and (w), for weak and soft, are added. For the microstructures with bidispersely sized spheres superscript (b) marks the values evaluated for the big particles and (s) the ones computed for the small particles. For the two-phase HSSs the stress values are given as phase averages, superscript (p). Material data and designations follow table 11.

	micro-structure	E^* [GPa]	ν^* [$\times 10^{-1}$]	$\sigma_{\mathrm{eq}}^{(\mathrm{m})}$ [MPa]	$\sigma_1^{(\mathrm{m})}$ [MPa]	$\sigma_{\mathrm{H}}^{(\mathrm{m})}$ [MPa]	$\sigma_{\mathrm{eq}}^{(\mathrm{p})}$ [MPa]	$\sigma_1^{(\mathrm{p})}$ [MPa]	$\sigma_{\mathrm{H}}^{(\mathrm{p})}$ [MPa]
LB	$\mathrm{HSS}^{\mu 2}_{15\%}$	234.53	2.928	110.54	111.70	38.03	155.41	148.795	45.19
UB		237.85	2.913						
LB	$\mathrm{HSS}^{\mu 3}_{15\%}$	212.28	2.930	105.25	105.87	35.70	111.23	107.72	33.57
UB		212.32	2.930						
							$\sigma_{\mathrm{eq}}^{(\mathrm{b})}/\sigma_{\mathrm{eq}}^{(\mathrm{s})}$	$\sigma_1^{(\mathrm{b})}/\sigma_1^{(\mathrm{s})}$	$\sigma_{\mathrm{H}}^{(\mathrm{b})}/\sigma_{\mathrm{H}}^{(\mathrm{s})}$
	$\mathrm{HSS}^{\mu 4}_{15\%}$	231.44	2.928	109.78	110.89	37.69	154.38/116.03	147.72/112.80	44.81/35.44
	$\mathrm{HSS}^{\mu 5}_{15\%}$	215.13	2.930	105.92	106.61	35.999	148.93/111.94	142.08/108.48	42.79/33.85
							$\sigma_{\mathrm{eq}}^{(\mathrm{h})}/\sigma_{\mathrm{eq}}^{(\mathrm{w})}$	$\sigma_1^{(\mathrm{h})}/\sigma_1^{(\mathrm{w})}$	$\sigma_{\mathrm{H}}^{(\mathrm{h})}/\sigma_{\mathrm{H}}^{(\mathrm{w})}$
	$\mathrm{HSS}^{\mu 8}_{15\%}$	222.39	2.929	107.65	108.52	36.76	151.35/113.76	144.59/110.40	43.69/34.56
	$\mathrm{HSS}^{\mu 9}_{15\%}$	223.87	2.928	108.00	108.90	36.91	151.85/114.13	145.11/110.79	43.87/34.71

Table 18: Numerical predictions for overall and microscale elastic responses of HSSs ($\xi = 0.15$ nominal, 15 particles) subjected to a uniaxial tensile strain of $\varepsilon^{\mathrm{a}} = 0.0005$. Designations follow table 11.

micro-structure	E^*	ν^*	$\sigma_{\mathrm{eq}}^{(\mathrm{m})}$	$\sigma_1^{(\mathrm{m})}$	$\sigma_{\mathrm{H}}^{(\mathrm{m})}$	$\sigma_{\mathrm{eq}}^{(\mathrm{p})}$	$\sigma_1^{(\mathrm{p})}$	$\sigma_{\mathrm{H}}^{(\mathrm{p})}$
	[GPa]	[$\times 10^{-1}$]	[MPa]	[MPa]	[MPa]	[MPa]	[MPa]	[MPa]
$\mathrm{HSS}_{15\%}^{\mu 2}$	234.00	2.927	110.8 ± 9.5	111.6 ± 12.0	37.9 ± 6.3	156.9 ± 8.2	149.8 ± 8.6	45.2 ± 4.1
$\mathrm{HSS}_{15\%}^{\mu 3}$	212.08	2.930	105.2 ± 0.8	105.8 ± 1.1	35.7 ± 0.8	111.2 ± 4.3	107.5 ± 4.9	33.4 ± 2.5
$\mathrm{HSS}_{15\%}^{\mu 4}$	230.47	2.931	110.3 ± 8.4	110.9 ± 10.5	37.6 ± 5.5	148.1 ± 12.7	141.9 ± 12.2	43.2 ± 4.2
$\mathrm{HSS}_{15\%}^{\mu 5}$	214.58	2.931	105.9 ± 3.5	106.5 ± 4.5	35.9 ± 2.4	116.1 ± 12.7	112.2 ± 11.8	34.8 ± 3.6
$\mathrm{HSS}_{15\%}^{\mu 6}$	233.31	2.929	110.9 ± 9.2	111.7 ± 11.6	37.9 ± 6.0	154.4 ± 6.1	147.6 ± 6.6	44.7 ± 3.3
$\mathrm{HSS}_{15\%}^{\mu 7}$	212.08	2.930	105.2 ± 1.5	105.8 ± 1.8	35.7 ± 1.1	110.9 ± 3.1	107.3 ± 3.9	33.4 ± 2.1
$\mathrm{HSS}_{15\%}^{\mu 8}$	221.91	2.929	107.8 ± 6.2	108.5 ± 7.9	36.7 ± 4.1	131.4 ± 18.6	126.2 ± 17.4	38.6 ± 5.5
$\mathrm{HSS}_{15\%}^{\mu 9}$	223.41	2.977	108.1 ± 6.7	108.8 ± 8.5	36.8 ± 4.4	134.8 ± 19.3	129.4 ± 18.2	39.6 ± 5.7

Table 19: Continuation A of table 18: Numerical predictions for the microscale elastic responses of HSSs subjected to a uniaxial tensile strain of $\varepsilon^{\mathrm{a}} = 0.0005$. Average stresses are given for big particles, (b), and small particles, (s), for unit cells containing bidispersely sized particles. For designations and corresponding material data refer to table 11.

micro-structure	$\sigma_{\mathrm{eq}}^{(\mathrm{b})}$	$\sigma_1^{(\mathrm{b})}$	$\sigma_{\mathrm{H}}^{(\mathrm{b})}$	$\sigma_{\mathrm{eq}}^{(\mathrm{s})}$	$\sigma_1^{(\mathrm{s})}$	$\sigma_{\mathrm{H}}^{(\mathrm{s})}$
	[MPa]	[MPa]	[MPa]	[MPa]	[MPa]	[MPa]
$\mathrm{HSS}_{15\%}^{\mu 4}$	152.5 ± 3.8	146.1 ± 3.3	44.5 ± 1.5	117.2 ± 10.6	112.6 ± 12.5	34.6 ± 6.3
$\mathrm{HSS}_{15\%}^{\mu 5}$	111.7 ± 1.0	108.2 ± 0.9	33.8 ± 0.3	147.7 ± 12.9	140.1 ± 15.6	41.7 ± 7.2
$\mathrm{HSS}_{15\%}^{\mu 6}$	153.9 ± 3.5	147.4 ± 2.9	44.8 ± 1.4	157.6 ± 14.4	148.9 ± 16.9	43.9 ± 8.6
$\mathrm{HSS}_{15\%}^{\mu 7}$	111.0 ± 0.4	107.5 ± 0.3	33.5 ± 0.1	110.3 ± 8.7	106.0 ± 11.2	32.6 ± 5.8

Table 20: Continuation B of table 18: Numerical predictions for the microscale elastic responses of HSSs subjected to a uniaxial tensile strain of $\varepsilon^{\mathrm{a}} = 0.0005$. Average stresses are given for hard and strong particles, (h), and weak and soft particles, (w). For designations and corresponding material data refer to table 11.

micro-structure	$\sigma_{\mathrm{eq}}^{(\mathrm{h})}$ [MPa]	$\sigma_1^{(\mathrm{h})}$ [MPa]	$\sigma_{\mathrm{H}}^{(\mathrm{h})}$ [MPa]	$\sigma_{\mathrm{eq}}^{(\mathrm{w})}$ [MPa]	$\sigma_1^{(\mathrm{w})}$ [MPa]	$\sigma_{\mathrm{H}}^{(\mathrm{w})}$ [MPa]
$\mathrm{HSS}_{15\%}^{\mu 8}$	150.3 ± 6.3	143.6 ± 7.1	43.4 ± 3.6	114.9 ± 5.6	111.0 ± 5.7	34.5 ± 2.7
$\mathrm{HSS}_{15\%}^{\mu 9}$	151.8 ± 6.8	145.1 ± 7.4	43.9 ± 3.7	115.4 ± 6.2	111.5 ± 6.5	34.6 ± 3.0

Table 21: Unit cell predictions for the microscale elastoplastic responses of HSSs ($\xi = 15.0\%$, 15 particles) subjected to a uniaxial tensile strain of $\varepsilon^{\mathrm{a}} = 0.032$ (for corresponding homogenized stresses see table 26), particle cleavage being suppressed. The spherical carbides are uniformly sized spheres, models $\mathrm{HSS}_{15\%}^{\mu 2}$, $\mathrm{HSS}_{15\%}^{\mu 3}$, $\mathrm{HSS}_{15\%}^{\mu 8}$ and $\mathrm{HSS}_{15\%}^{\mu 9}$, and bidispersely sized spheres, models $\mathrm{HSS}_{15\%}^{\mu 4}$, $\mathrm{HSS}_{15\%}^{\mu 5}$, $\mathrm{HSS}_{15\%}^{\mu 6}$ and $\mathrm{HSS}_{15\%}^{\mu 7}$, respectively. For definition of the microstructures see table 11.

micro-structure	$\varepsilon_{\mathrm{eq,p}}^{(\mathrm{m})}$ [$\times 10^{-2}$]	$\sigma_{\mathrm{eq}}^{(\mathrm{m})}$ [GPa]	$\sigma_1^{(\mathrm{m})}$ [GPa]	$\sigma_{\mathrm{H}}^{(\mathrm{m})}$ [GPa]	$\sigma_{\mathrm{eq}}^{(\mathrm{p})}$ [GPa]	$\sigma_1^{(\mathrm{p})}$ [GPa]	$\sigma_{\mathrm{H}}^{(\mathrm{p})}$ [GPa]
$\mathrm{HSS}_{15\%}^{\mu 2}$	2.17 ± 1.05	2.97 ± 0.05	3.02 ± 0.42	1.08 ± 0.39	4.86 ± 0.33	4.17 ± 0.34	0.90 ± 0.25
$\mathrm{HSS}_{15\%}^{\mu 3}$	1.99 ± 0.60	2.96 ± 0.03	3.02 ± 0.29	1.07 ± 0.27	4.39 ± 0.22	3.81 ± 0.24	0.88 ± 0.15
$\mathrm{HSS}_{15\%}^{\mu 4}$	2.14 ± 0.78	2.97 ± 0.04	3.02 ± 0.40	1.08 ± 0.37	4.79 ± 0.26	4.07 ± 0.26	0.88 ± 0.18
$\mathrm{HSS}_{15\%}^{\mu 5}$	2.01 ± 0.53	2.96 ± 0.03	3.01 ± 0.30	1.07 ± 0.28	4.43 ± 0.29	3.84 ± 0.24	0.89 ± 0.12
$\mathrm{HSS}_{15\%}^{\mu 6}$	2.17 ± 0.82	2.97 ± 0.04	3.02 ± 0.42	1.08 ± 0.39	4.87 ± 0.26	4.11 ± 0.26	0.88 ± 0.19
$\mathrm{HSS}_{15\%}^{\mu 7}$	1.99 ± 0.50	2.96 ± 0.03	3.02 ± 0.29	1.07 ± 0.28	4.38 ± 0.18	3.79 ± 0.19	0.87 ± 0.12
$\mathrm{HSS}_{15\%}^{\mu 8}$	2.08 ± 0.82	2.96 ± 36.9	3.02 ± 0.36	1.08 ± 0.33	4.61 ± 0.33	3.96 ± 0.31	0.89 ± 0.20
$\mathrm{HSS}_{15\%}^{\mu 9}$	2.09 ± 0.86	2.96 ± 0.04	3.02 ± 0.36	1.06 ± 0.34	4.65 ± 0.36	3.99 ± 0.33	0.89 ± 0.21

Table 22: Continuation A of table 21: Unit cell predictions for the microscale elastoplastic responses of HSSs subjected to a uniaxial tensile strain of $\varepsilon^{\mathrm{a}} = 0.032$ (for corresponding homogenized stresses see table 26), particle failure being suppressed. Average stresses are given for big particles, (b), and small particles, (s), for unit cells containing bidispersely sized particles. For designations and corresponding material data refer to table 11.

micro-structure	$\sigma_{\mathrm{eq}}^{(\mathrm{b})}$ [GPa]	$\sigma_{1}^{(\mathrm{b})}$ [GPa]	$\sigma_{\mathrm{H}}^{(\mathrm{b})}$ [GPa]	$\sigma_{\mathrm{eq}}^{(\mathrm{s})}$ [GPa]	$\sigma_{1}^{(\mathrm{s})}$ [GPa]	$\sigma_{\mathrm{H}}^{(\mathrm{s})}$ [GPa]
$\mathrm{HSS}_{15\%}^{\mu 4}$	4.83 ± 0.19	4.09 ± 0.19	0.88 ± 0.16	4.54 ± 0.43	3.85 ± 0.48	0.85 ± 0.28
$\mathrm{HSS}_{15\%}^{\mu 5}$	4.35 ± 0.13	3.80 ± 0.12	0.90 ± 0.08	4.94 ± 0.54	4.10 ± 0.55	0.83 ± 0.23
$\mathrm{HSS}_{15\%}^{\mu 6}$	4.84 ± 0.19	4.11 ± 0.19	0.89 ± 0.16	5.06 ± 0.50	4.17 ± 0.55	0.82 ± 0.31
$\mathrm{HSS}_{15\%}^{\mu 7}$	4.37 ± 0.12	3.79 ± 0.12	0.88 ± 0.09	4.48 ± 0.38	3.81 ± 0.45	0.83 ± 0.24

Table 23: Continuation B of table 21: Unit cell predictions for the microscale elastoplastic responses of HSSs subjected to a uniaxial tensile strain of $\varepsilon^{\mathrm{a}} = 0.032$ (for corresponding homogenized stresses see table 26), particle failure being suppressed. Average stresses are given for hard and strong particles, (h), and soft and weak particles, (w). For designations and corresponding material data refer to table 11.

micro-structure	$\sigma_{\mathrm{eq}}^{(\mathrm{h})}$ [GPa]	$\sigma_{1}^{(\mathrm{h})}$ [GPa]	$\sigma_{\mathrm{H}}^{(\mathrm{h})}$ [GPa]	$\sigma_{\mathrm{eq}}^{(\mathrm{w})}$ [GPa]	$\sigma_{1}^{(\mathrm{w})}$ [GPa]	$\sigma_{\mathrm{H}}^{(\mathrm{w})}$ [GPa]
$\mathrm{HSS}_{15\%}^{\mu 8}$	4.82 ± 0.30	4.09 ± 0.31	0.88 ± 0.23	4.43 ± 0.24	3.84 ± 0.26	0.89 ± 0.17
$\mathrm{HSS}_{15\%}^{\mu 9}$	4.84 ± 0.31	4.13 ± 0.31	0.91 ± 0.24	4.43 ± 0.26	3.82 ± 0.28	0.88 ± 0.17

Table 24: Predicted responses at the microscale for HSSs ($\xi = 15.0\%$, 15 particles) subjected to a tensile load up to a uniaxial strain of $\varepsilon^{\mathrm{a}} = 0.032$ (for corresponding homogenized stresses see table 26), particle fracture being activated. The spherical carbides are uniformly sized spheres (models $\mathrm{HSS}_{15\%}^{\mu2}$, $\mathrm{HSS}_{15\%}^{\mu3}$, $\mathrm{HSS}_{15\%}^{\mu8}$ and $\mathrm{HSS}_{15\%}^{\mu9}$) and bidispersely sized spheres (models $\mathrm{HSS}_{15\%}^{\mu4}$, $\mathrm{HSS}_{15\%}^{\mu5}$, $\mathrm{HSS}_{15\%}^{\mu6}$ and $\mathrm{HSS}_{15\%}^{\mu7}$), respectively. Designations of microstructures follow table 11.

micro-structure	$\varepsilon_{\mathrm{eq,p}}^{(\mathrm{m})}$ $[\times 10^{-2}]$	$\sigma_{\mathrm{eq}}^{(\mathrm{m})}$ [GPa]	$\sigma_{1}^{(\mathrm{m})}$ [GPa]	$\sigma_{\mathrm{H}}^{(\mathrm{m})}$ [GPa]	$\sigma_{\mathrm{eq}}^{(\mathrm{p})}$ [GPa]	$\sigma_{1}^{(\mathrm{p})}$ [GPa]	$\sigma_{\mathrm{H}}^{(\mathrm{p})}$ [GPa]
$\mathrm{HSS}_{15\%}^{\mu2}$	1.92 ± 1.70	2.92 ± 0.16	2.94 ± 0.52	1.05 ± 0.46	3.80 ± 1.08	2.83 ± 1.48	0.35 ± 0.92
$\mathrm{HSS}_{15\%}^{\mu3}$	1.57 ± 1.84	2.90 ± 0.15	2.90 ± 0.55	1.03 ± 0.49	2.39 ± 0.80	1.35 ± 1.06	-1.85 ± 0.77
$\mathrm{HSS}_{15\%}^{\mu4}$	1.70 ± 1.55	2.91 ± 0.15	2.91 ± 0.61	1.03 ± 0.55	3.19 ± 1.19	2.10 ± 0.49	0.04 ± 0.96
$\mathrm{HSS}_{15\%}^{\mu5}$	1.58 ± 1.44	2.90 ± 0.14	2.91 ± 0.58	1.03 ± 0.52	2.56 ± 0.98	1.49 ± 1.24	-0.17 ± 0.79
$\mathrm{HSS}_{15\%}^{\mu6}$	1.67 ± 1.59	2.90 ± 0.16	2.90 ± 0.61	1.03 ± 0.55	3.03 ± 1.07	1.86 ± 1.40	-0.09 ± 0.96
$\mathrm{HSS}_{15\%}^{\mu7}$	1.51 ± 1.60	2.87 ± 0.20	2.85 ± 0.62	1.01 ± 0.54	2.22 ± 0.74	1.17 ± 0.99	-0.25 ± 0.74
$\mathrm{HSS}_{15\%}^{\mu8}$	1.71 ± 1.85	2.91 ± 0.14	2.91 ± 0.56	1.03 ± 0.51	3.03 ± 1.15	2.05 ± 1.44	0.09 ± 0.85
$\mathrm{HSS}_{15\%}^{\mu9}$	1.72 ± 1.89	2.92 ± 0.14	2.92 ± 0.57	1.04 ± 0.52	3.03 ± 1.13	2.05 ± 1.39	0.08 ± 0.87

Table 25: Continuation of table 24: Microscale elastoplastic responses of the surviving intact particles after uniaxial tensile global straining to $\varepsilon^{\mathrm{a}} = 0.032$ (for corresponding homogenized stresses see table 26) of HSS (volume fraction $\xi = 15.0$ vol.%). Additionally, for this overall strain the evaluated average overall pore volume fraction caused by particle failure is given.

micro-structure	$\sigma_{\mathrm{eq}}^{(intact)}$ [GPa]	$\sigma_{1}^{(intact)}$ [GPa]	$\sigma_{\mathrm{H}}^{(intact)}$ [GPa]	f_v [%]
$\mathrm{HSS}_{15\%}^{\mu2}$	4.59 ± 0.39	3.94 ± 0.44	0.91 ± 0.28	0.43 ± 0.05
$\mathrm{HSS}_{15\%}^{\mu3}$	all failed	all failed	all failed	0.74 ± 0.02
$\mathrm{HSS}_{15\%}^{\mu4}$	4.64 ± 0.36	3.93 ± 0.41	0.86 ± 0.28	0.70 ± 0.08
$\mathrm{HSS}_{15\%}^{\mu5}$	4.55 ± 0.65	3.89 ± 0.55	0.90 ± 0.31	0.97 ± 0.32
$\mathrm{HSS}_{15\%}^{\mu6}$	4.51 ± 0.35	3.76 ± 0.42	0.80 ± 0.27	0.58 ± 0.18
$\mathrm{HSS}_{15\%}^{\mu7}$	3.46 ± 0.22	3.03 ± 0.26	0.75 ± 0.27	0.82 ± 0.01
$\mathrm{HSS}_{15\%}^{\mu8}$	4.51 ± 0.37	3.81 ± 0.38	0.85 ± 0.29	0.61 ± 0.02
$\mathrm{HSS}_{15\%}^{\mu9}$	4.30 ± 0.55	3.58 ± 0.45	0.73 ± 0.25	0.62 ± 0.02

Table 26: Summary of the predicted overall stresses under overall uniaxial tensile strain of $\varepsilon^{\mathrm{a}} = 0.032$ of all modeled HSS microstructures (reinforcement volume fraction and unit cell model are given). Values are given, first, for the case where particle failure was suppressed, and, second, where particles were allowed to fail during the loading (data involving particle fracture are averages from at least two simulation runs, the corresponding standard deviations being also given). For the definitions of the microstructures see table 11.

$\mathrm{vol.\%}/_{\mathbf{arr.}}$	*micro- structure*	$\sigma^{\mathrm{a}}_{\text{(failure suppressed)}}$	$\dfrac{\sigma^{\mathrm{a}}_{\text{(failure suppressed)}}}{_{0}\sigma^{(\mathrm{m})}_{\mathrm{y}}}$	$\sigma^{\mathrm{a}}_{\text{(failure activated)}}$	$\dfrac{\sigma^{\mathrm{a}}_{\text{(failure activated)}}}{_{0}\sigma^{(\mathrm{m})}_{\mathrm{y}}}$
		[GPa]	[1]	[GPa]	[1]
$^{6.3}/_{\mathbf{A}}$	$\mathrm{HSS}^{\mu 1}_{6.3\%}$	3.04	1.11	2.90 ± 0.03	1.05
$^{6.3}/_{\mathbf{B}}$	$\mathrm{HSS}^{\mu 1}_{6.3\%}$	3.04	1.11	2.98 ± 0.01	1.08
$^{15.0}/_{\mathbf{C}}$	$\mathrm{HSS}^{\mu 2}_{15\%}$	3.16	1.15	2.81 ± 0.02	1.02
$^{15.0}/_{\mathbf{C}}$	$\mathrm{HSS}^{\mu 3}_{15\%}$	3.13	1.14	2.55 ± 0.02	0.93
$^{15.0}/_{\mathbf{E}}$	$\mathrm{HSS}^{\mu 4}_{15\%}$	3.15	1.15	2.55 ± 0.15	0.93
$^{15.0}/_{\mathbf{E}}$	$\mathrm{HSS}^{\mu 5}_{15\%}$	3.12	1.14	2.53 ± 0.03	0.92
$^{15.0}/_{\mathbf{E}}$	$\mathrm{HSS}^{\mu 6}_{15\%}$	3.16	1.15	2.68 ± 0.12	0.98
$^{15.0}/_{\mathbf{E}}$	$\mathrm{HSS}^{\mu 7}_{15\%}$	3.12	1.14	2.47 ± 0.22	0.90
$^{15.0}/_{\mathbf{C}}$	$\mathrm{HSS}^{\mu 8}_{15\%}$	3.14	1.14	2.66 ± 0.01	0.97
$^{15.0}/_{\mathbf{C}}$	$\mathrm{HSS}^{\mu 9}_{15\%}$	3.15	1.15	2.65 ± 0.03	0.96

Figures
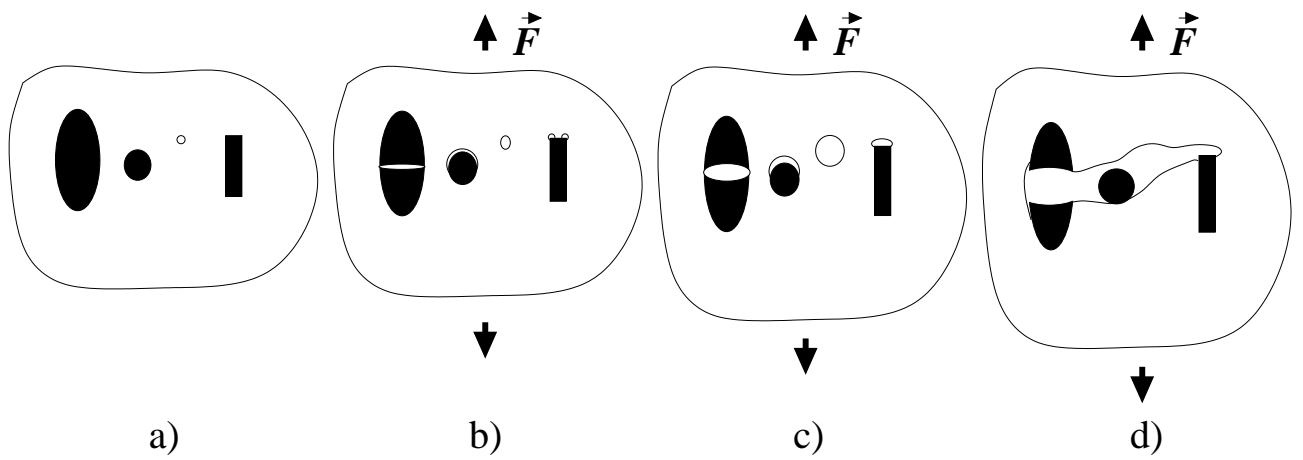
Figure 1: Beginning with initial damage (a) creation of additional pores and pore growth occur (b). Further increasing the load (c) results in coalescence of pores and microcracks (d).
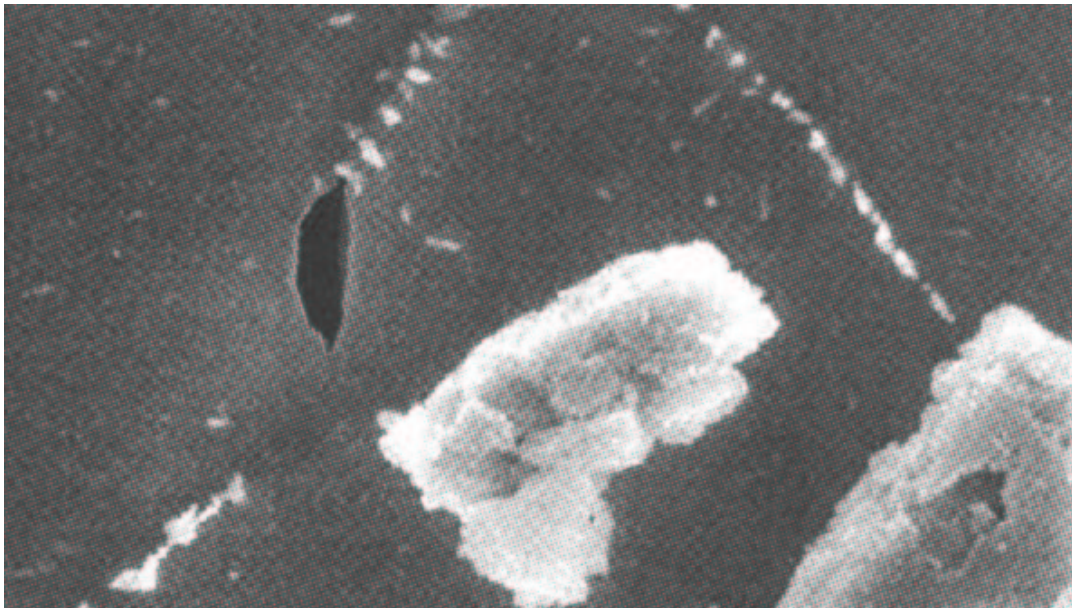
Figure 2: Damage of AA6061/Al$_2$O$_3$/10p caused by pore growth within the matrix, from Pandorf [2000].
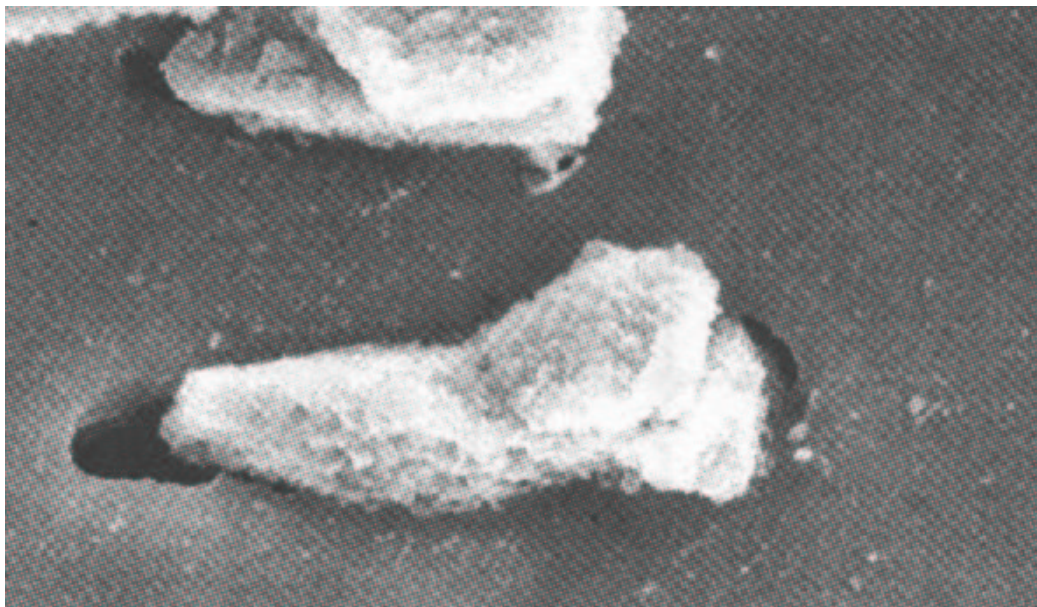
Figure 3: Damage of AA6061/Al$_2$O$_3$/10p caused by debonding at elongated Al$_2$O$_3$-particles, from Pandorf [2000].
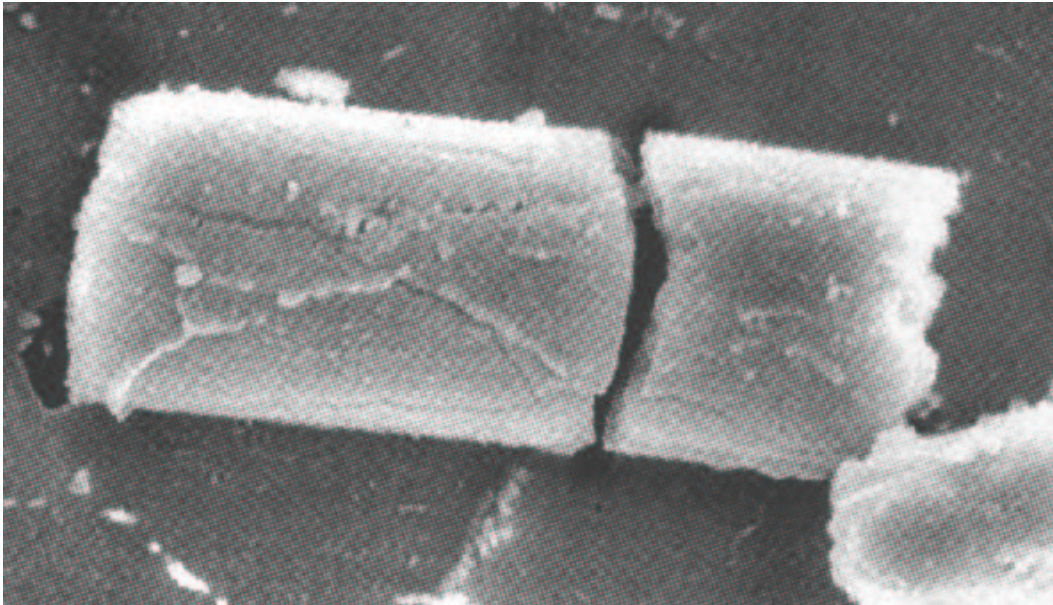
Figure 4: Damage of AA6061/Al$_2$O$_3$/10p caused by broken Al$_2$O$_3$-particles (at elevated temperatures, from Pandorf [2000]).
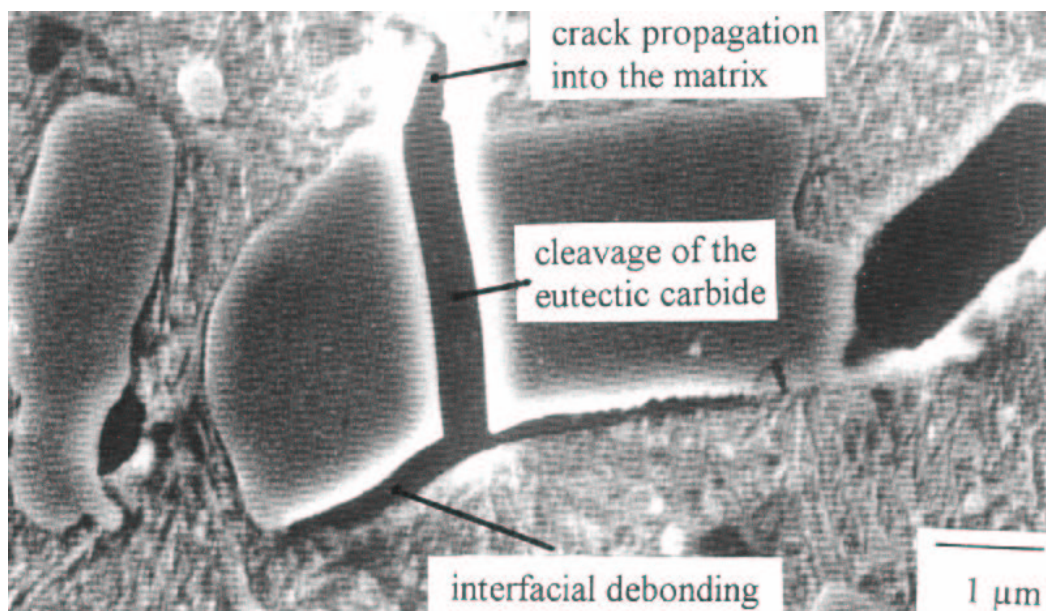
Figure 5: Particle cleavage initiates interfacial and matrix failure (microcrack propagation after carbide cleavage in steel SAE-D3, from Gross-Weege [1996]).
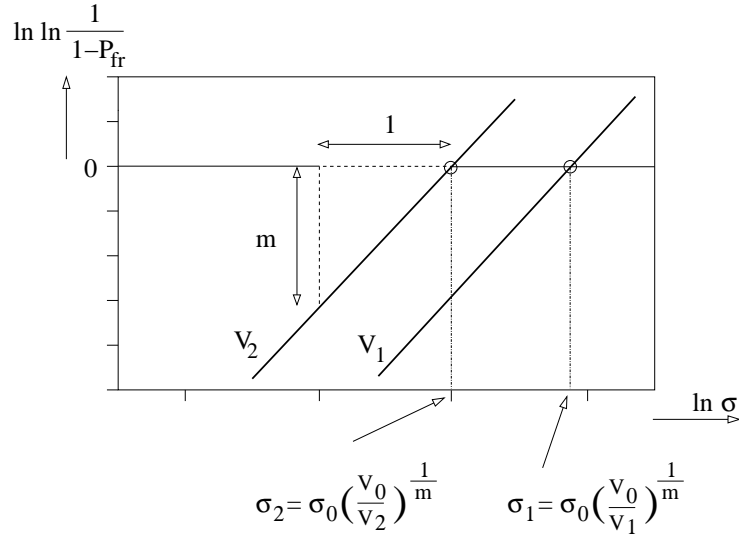
Figure 6: Weibull fracture probability distribution: the logarithmic risk of fracture $\ln n(\sigma) = \ln\left(\ln\frac{1}{1-P_{\mathrm{fr}}}\right)$ as function of the applied stress $\ln\sigma$. The solid curves represent samples with same m but different volumes $V_2 > V_1$: the curves with the same slope m move towards lower stress of fracture for increasing specimen volumes.
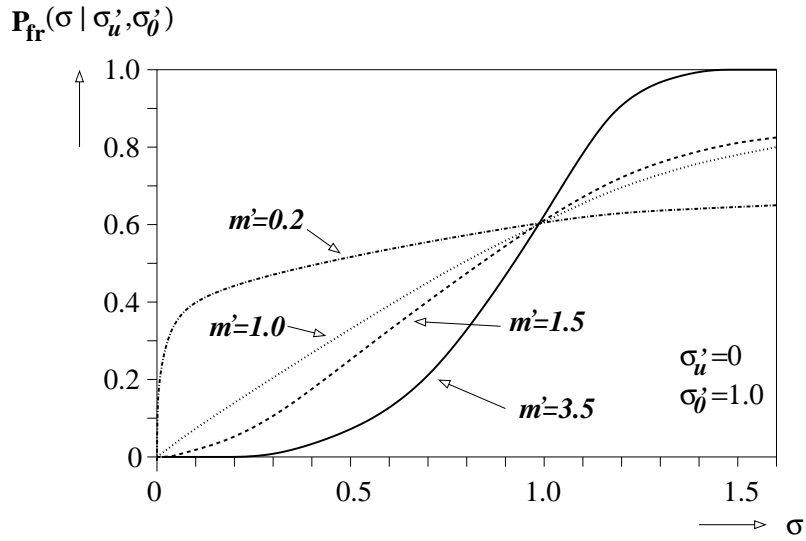
Figure 7: The standardized Weibull distribution function $P_{\mathrm{fr}} = P_{\mathrm{fr}}(\sigma|\sigma'_u = 0, \sigma'_0 = 1, m')$ (two parametric) for different shape parameters m (Weibull parameter), see also eqn. (B.2).
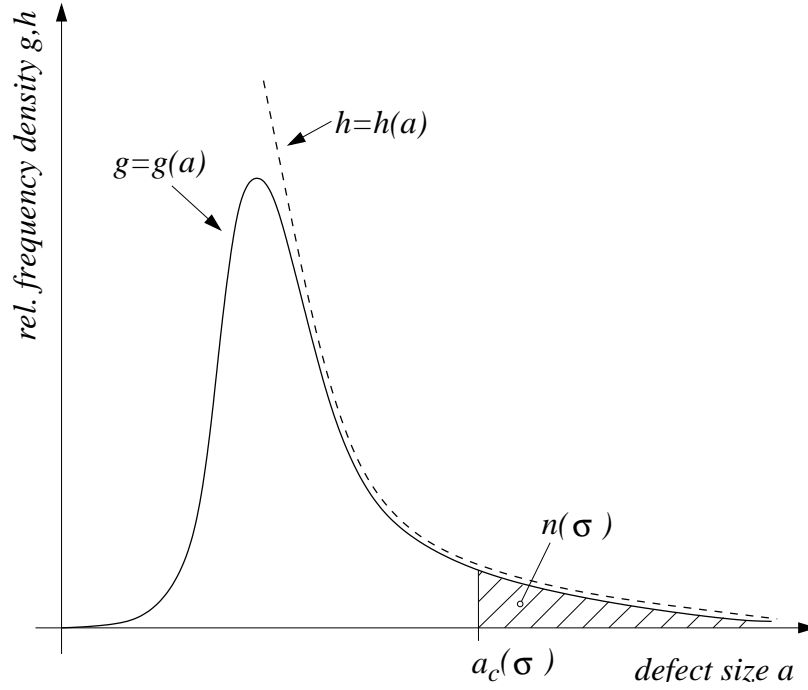
Figure 8: Schematic diagram of the relative frequency density per volume, g, of the defect size a in a brittle material. The function $g = g(a)$ is approximated by an inverse power law $h = h(a)$ in the interesting part of the curve. The shaded area represents the density of critical defects $n(\sigma)$, corresponding to the probability of failure per volume unit.
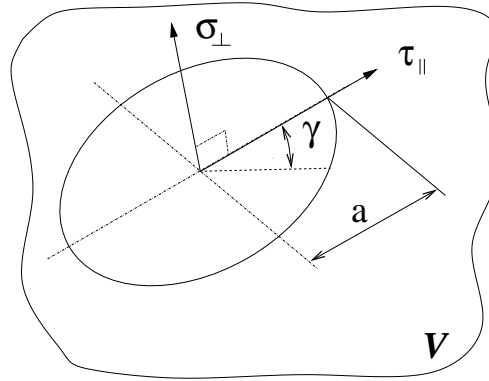
Figure 9: Schematic crack model of a circular crack in a 3D medium. $\sigma_\perp$ represents the normal stress vector acting on the crack plane, $\tau_\parallel$ is the in-plane shear stress, respectively. The angle γ describes the position of a point on the crack front contour of a crack with the length $2a$.
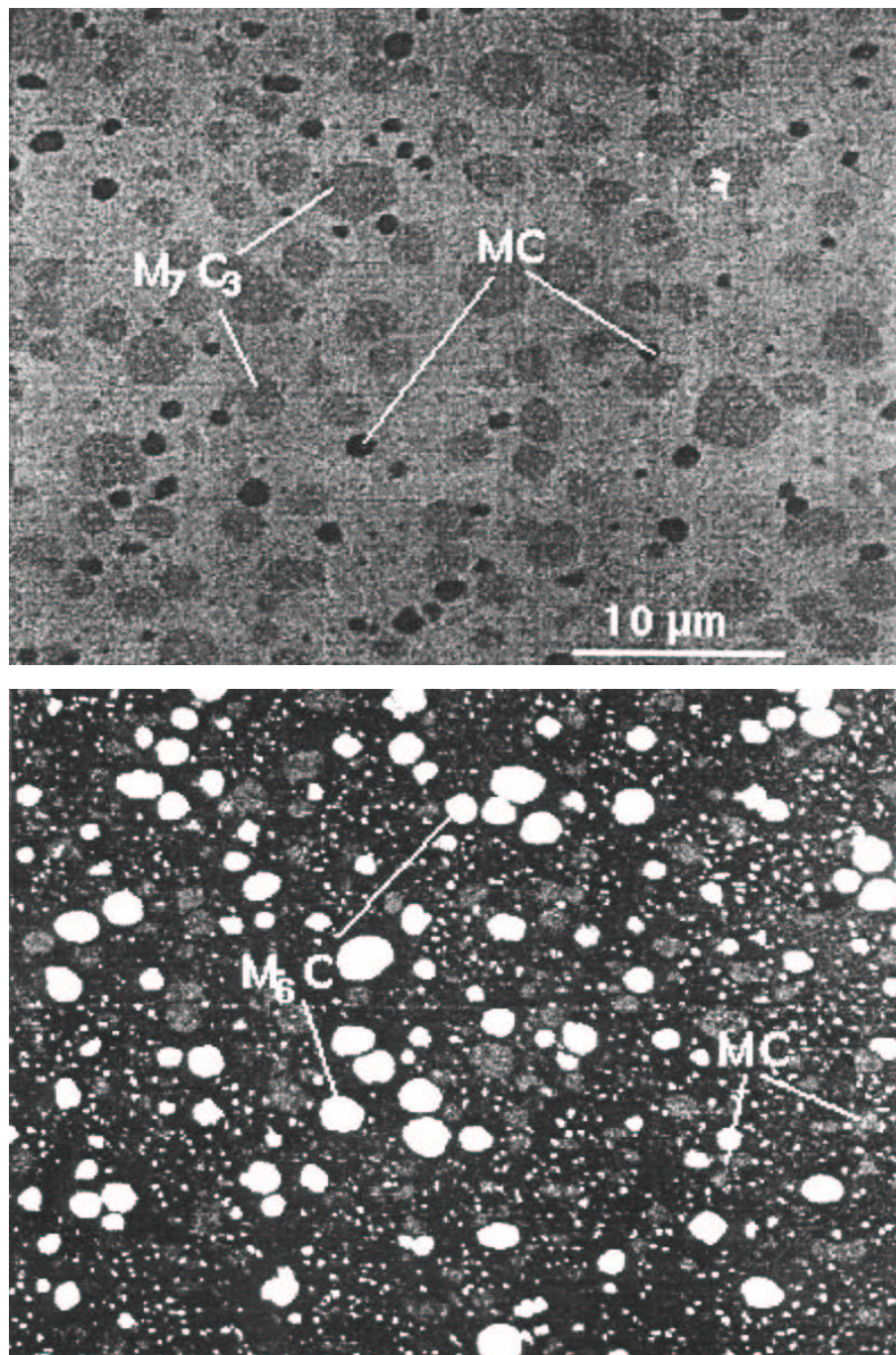
Figure 10: Two micrographs of the same scale of two powder metallurgically produced HSSs, the top image corresponding to the K190 Isomatrix and the bottom one to the S390 Isomatrix HSS (images and designations by Böhler), obtained by a **S**canning **E**lectron **M**icroscopy (SEM).
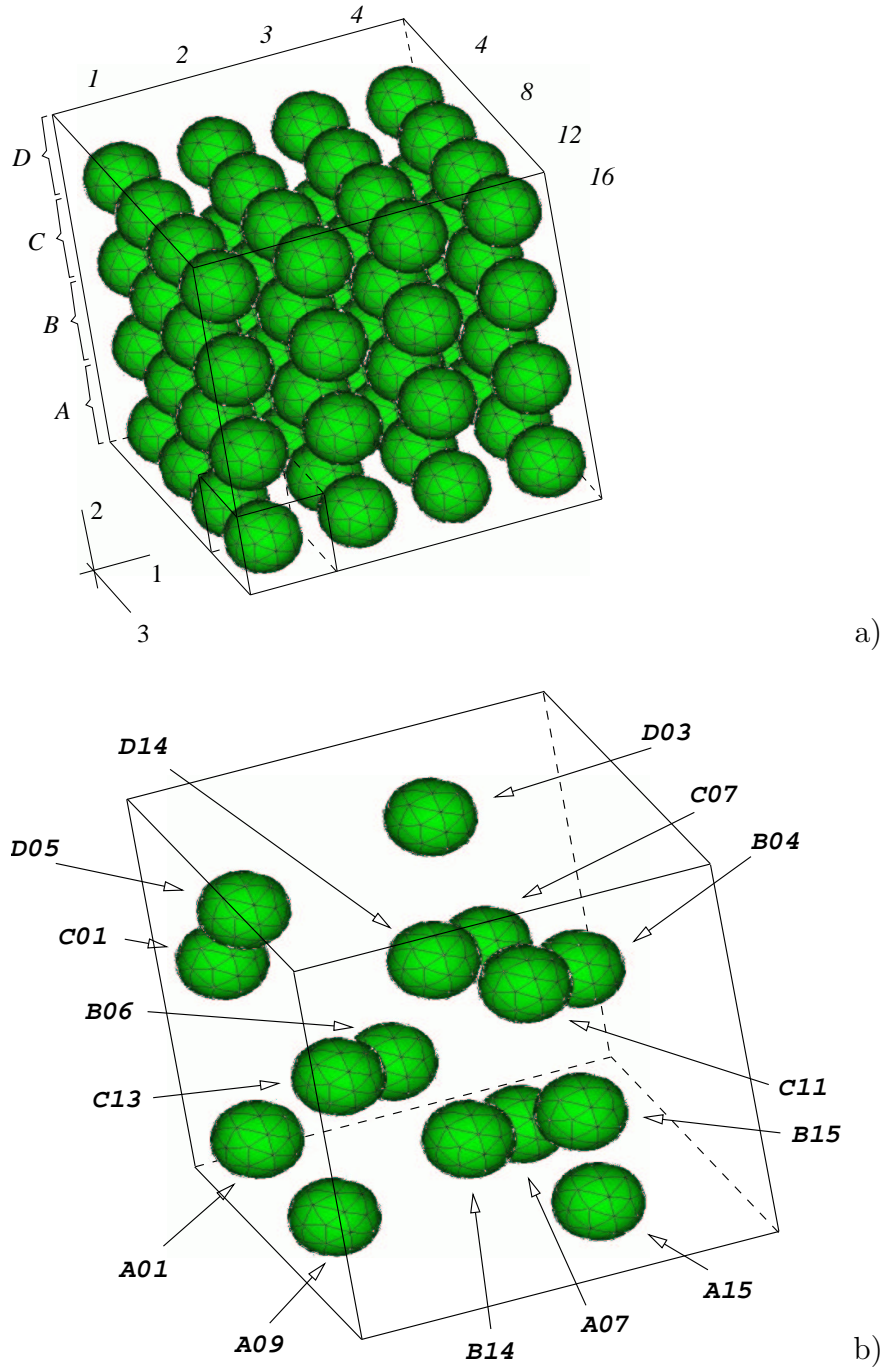
Figure 11: a) Unit cell with edge length of $l_{1,2,3} = 1.00$ containing 64 particles of diameter $d = 0.2$ in a simple cubic arrangement ($\xi = 26.9$ vol.%). b) RPC-model with 15 spheres chosen to have carbide material properties (for volume fraction $\xi = 6.3$ vol.%), embedded in the elastoplastic matrix (model A, matrix elements are not displayed).
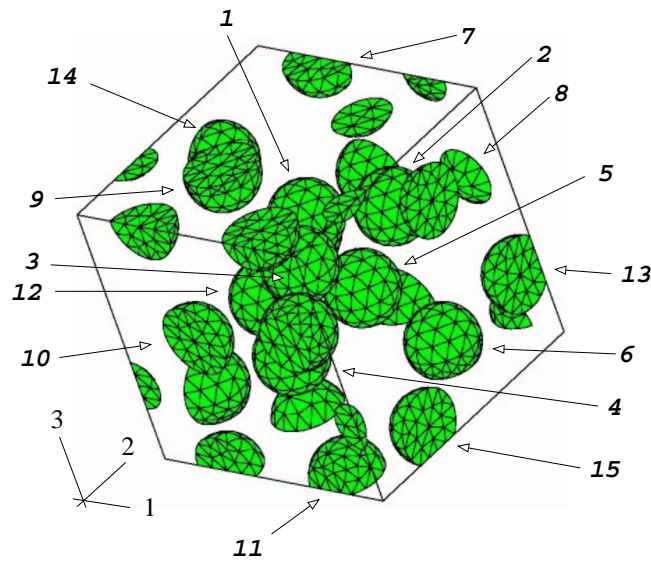
Figure 12: Unit cell C with 15 spherical particles of identical size in a random arrangement (nominal particle volume fraction $\xi = 15$ vol.%, arrangement obtained by RSA-method; particle numbers are given for later reference).
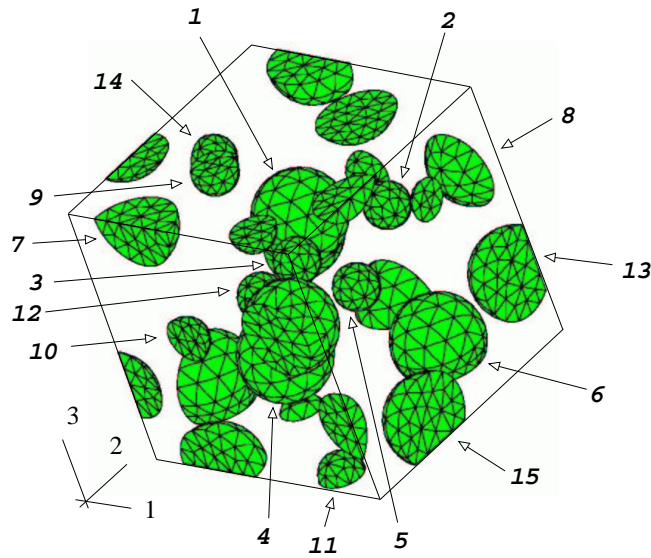
Figure 13: Unit cell E with 15 spherical particles of two different sizes, $r_1 = 2r_2$ in a random arrangement (nominal particle volume fraction $\xi = 15$ vol.%, arrangement obtained by RSA-method; particle numbers are given for later reference).
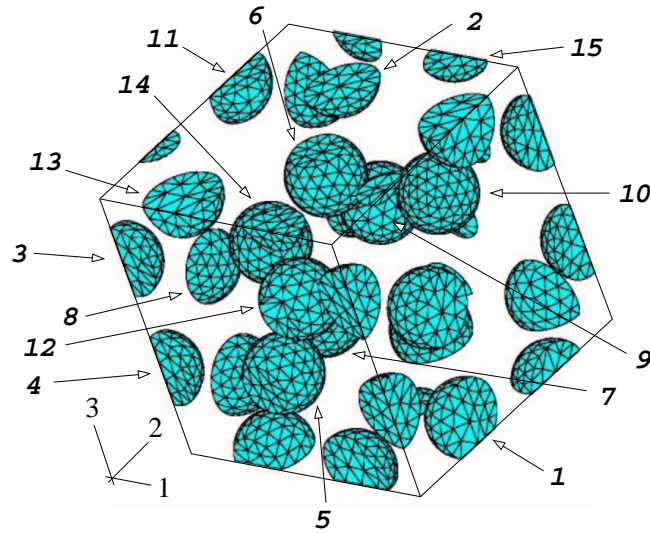
Figure 14: Unit cell D with 15 spherical particles of identical size in a random arrangement (nominal particle volume fraction $\xi = 15$ vol.%, arrangement obtained by RSA-method; particle numbers are given for later reference).
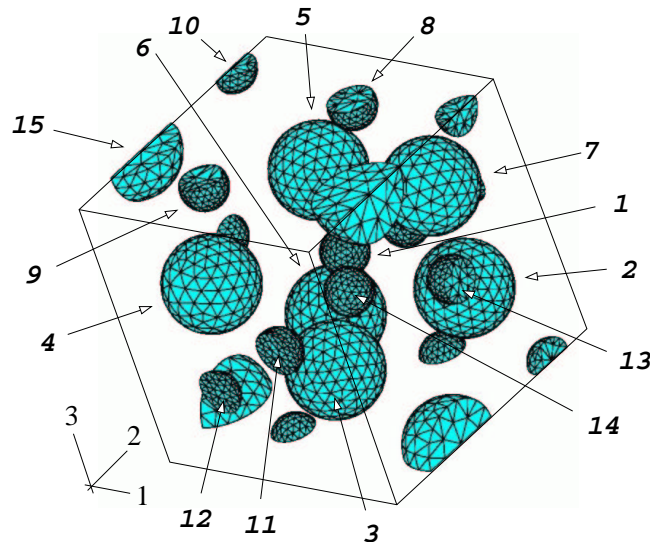
Figure 15: Unit cell F with 15 spherical particles of two different sizes, $r_1 = 2r_2$ in a random arrangement (nominal particle volume fraction $\xi = 15$ vol.%, arrangement obtained by RSA-method; particle numbers are given for later reference).
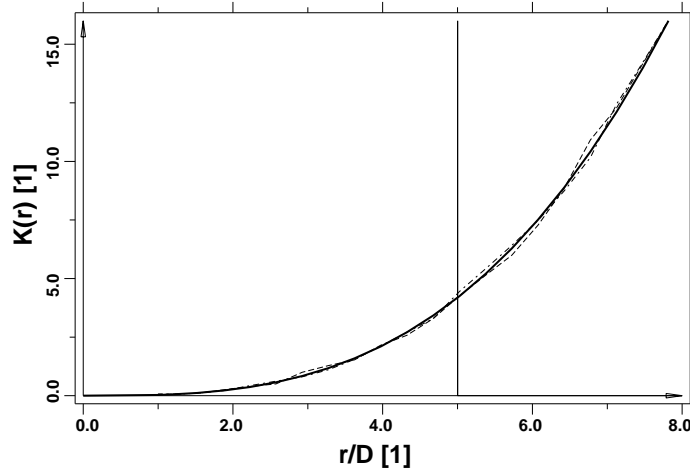
Figure 16: Second-order intensity function, $K(r)$, vs. non dimensional radius, $\frac{r}{D}$, for an RPC (dashed) and an RSA (dash-dotted) unit cell. The volume fraction was chosen as $\xi = 6.3$ vol.% and 15 particles are arranged within one unit cell ($D = 0.2$). For comparison the second-order intensity function of a Poisson arrangement (solid) is shown.
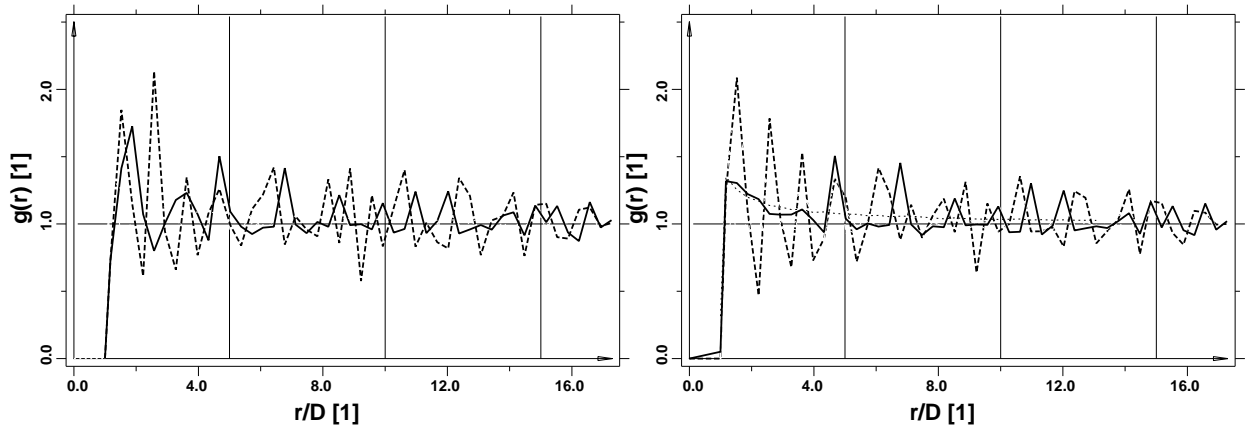
Figure 17: Pair distribution functions, $g(r)$, vs. non dimensional radius, $\frac{r}{D}$: The left diagram gives examples for one RPC (dashed) and one RSA (solid) arrangement of 15 inclusions in a unit cell (volume fraction $\xi = 6.3$ vol.%). The right diagram shows the averages of $g(r)$ of five RPC (dashed) and five RSA (solid) arrangements (15 inclusions arranged within a unit cell, volume fraction of $\xi = 6.3$ vol.%) and an example RSA arrangement of 5000 particles (dotted).
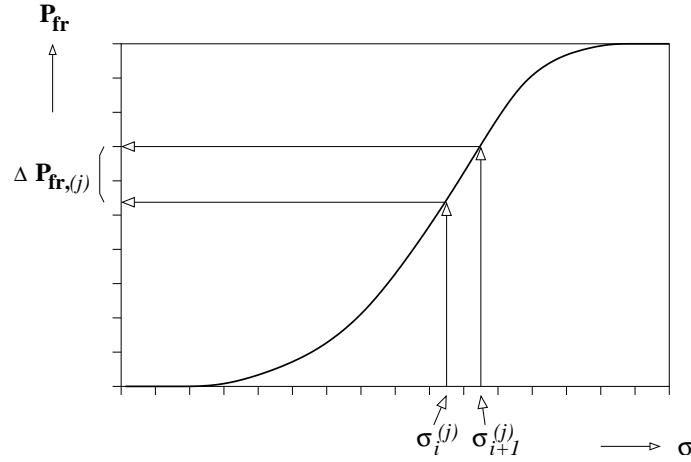
Figure 18: Schematic depiction of the difference in fracture probablities, $\Delta P_{\mathrm{fr},j}$, for particle j evaluated from a stress measure at the increments i and $i+1$.
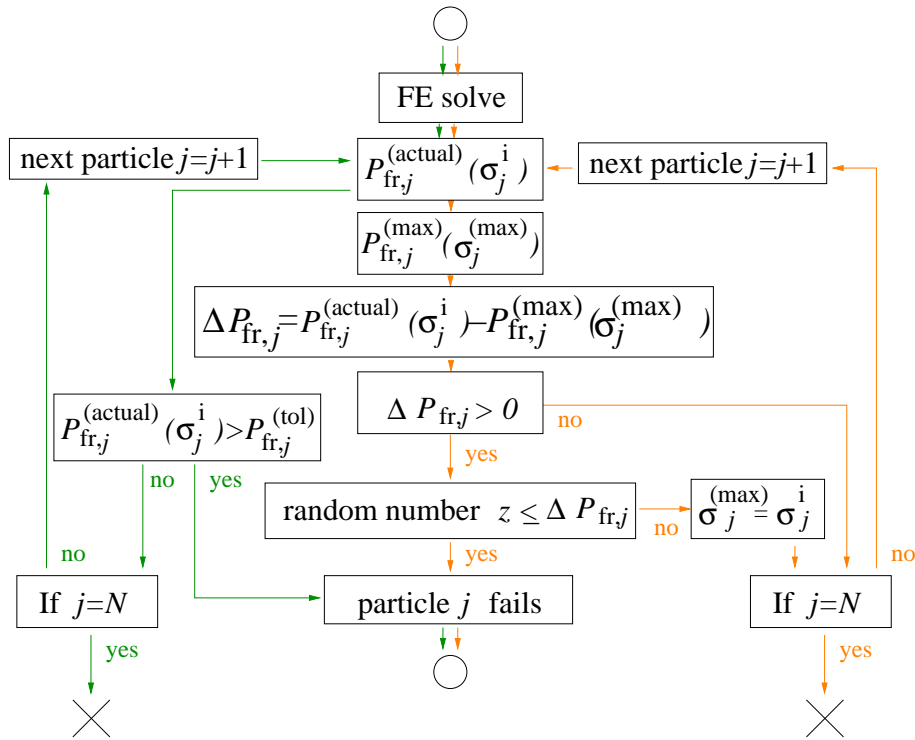
Figure 19: Flowchart of the two particle crack activation procedures used within this work. The green path represents the **W**eibull **R**ankine model (`WR`-model), where the actual particle fracture probability is directly compared with a tolerance $P_{\mathrm{fr},j}^{(\mathrm{tol})}$ and the red path shows the procedure described in section 3.3.2, using the **M**onte **C**arlo **W**eibull (`MCW`) model. N particles are modeled, the number of the particle being actively considered is j.
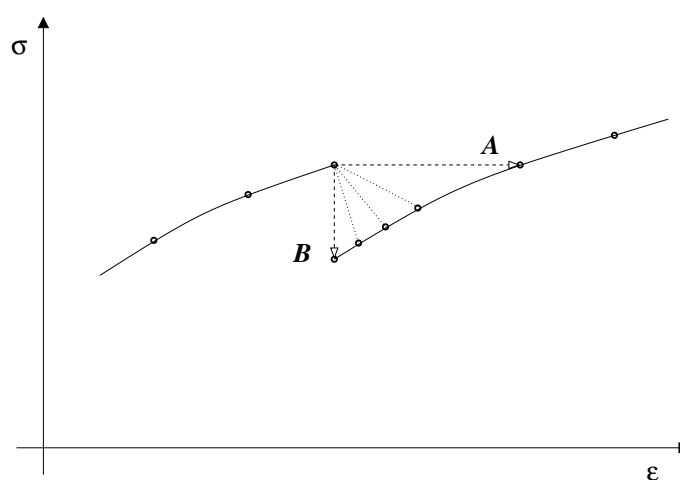
Figure 20: Effects on the resulting overall stress-strain behavior of three different incrementation strategies following the fracture of a particle. Searching for equilibrium at a constant overall stress in load controlled simulations, *A*, searching for equilibrium at a constant strain in displacement controlled simulations, *B* and using the ABAQUS auto incrementation algorithm in displacement controlled analyses (other solutions).
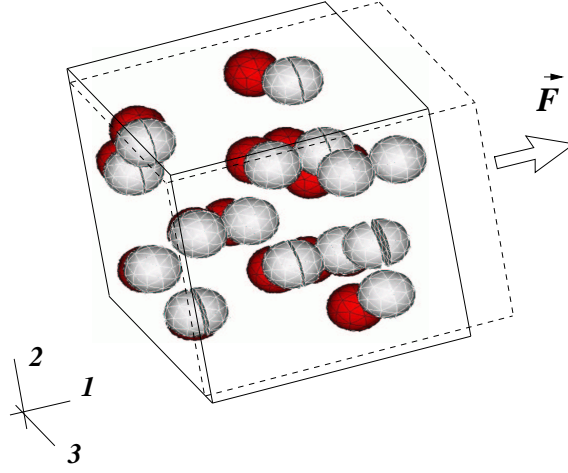
Figure 21: AA2618/SiC$_{6.3\mathrm{p}}^{eq}$-T4–`A/WR` ($P_{\mathrm{fr},j}^{(\mathrm{tol},2)} = 0.632$): Undeformed as well as deformed unit cell model (arrangement `A`) of an MMC with 15 spherical particles of identical size and shape and total volume fraction $\xi = 6.3$ vol.% after 7 particles have failed by cleavage under a tensile overall strain in the 1-direction of $\varepsilon^{\mathrm{a}} = 0.22$, $\sigma^{\mathrm{a}} = 515.9$ MPa (dark shade and solid lines mark initial state, light shade and dotted lines mark deformed state).
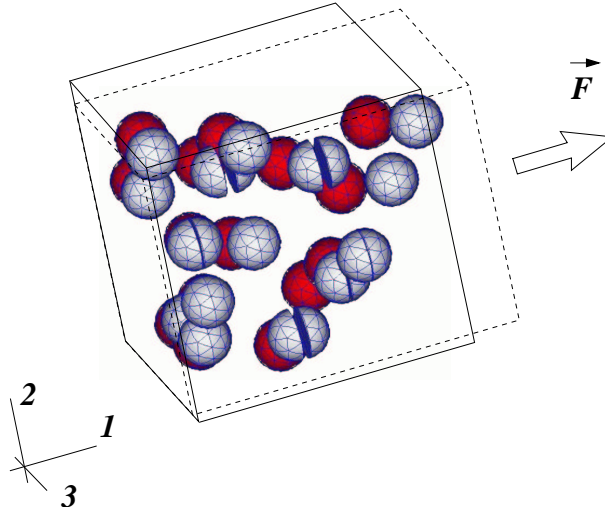
Figure 22: AA2618/SiC$_{6.3\mathrm{p}}^{eq}$-T4–`B/MCW`: Undeformed as well as deformed unit cell model (arrangement `B`) of an MMC with 15 spherical particles of identical size and shape and total volume fraction $\xi = 6.3$ vol.% after 6 particles have failed by cleavage under a tensile overall strain in the 1-direction of $\varepsilon^{\mathrm{a}} = 0.22$, $\sigma^{\mathrm{a}} = 520.3$ MPa (dark shade and solid lines mark initial state, light shade and dotted lines mark deformed state).
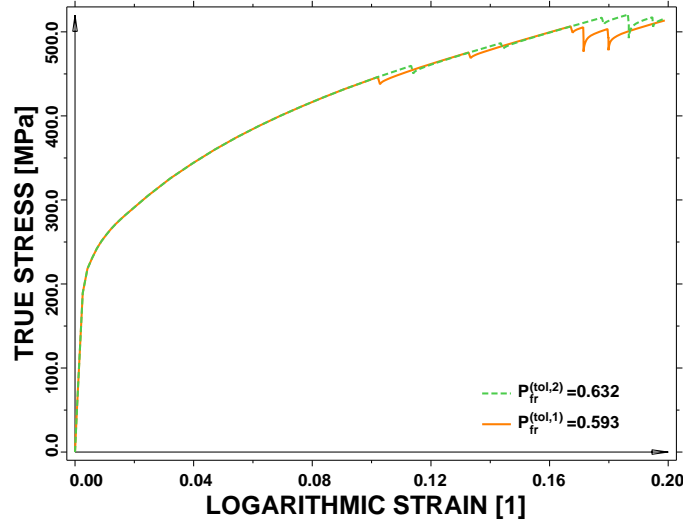
Figure 23: AA2618/SiC$_{6.3\mathrm{p}}^{eq}$-T4–`A`/`WR`: Overall uniaxial tensile stress-strain curves predicted by the 15-particle unit cell model (arrangement shown in figure 11b) using Weibull fracture probabilities of $P_{\mathrm{fr},j}^{(\mathrm{tol},1)} = 0.593$ (orange) and $P_{\mathrm{fr},j}^{(\mathrm{tol},2)} = 0.632$ (green) to trigger particle cracking. Figure 21 shows the particle states at the end of the simulation run represented by the orange stress-strain curve.
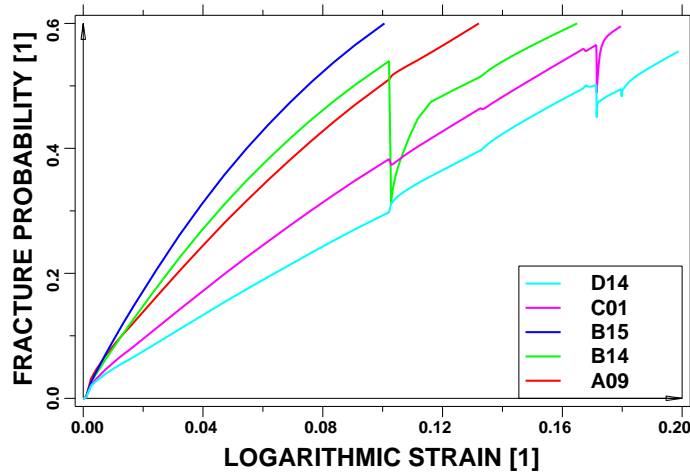
Figure 24: AA2618/SiC$_{6.3\mathrm{p}}^{eq}$-T4–`A`/`WR`: Predicted evolution of Weibull fracture probabilities (particle failure activated by the use of the `WR`-method at a particles' Weibull fracture probability of $P_{\mathrm{fr},j}^{(\mathrm{tol},1)} = 0.593$) under uniaxial tensile loading for selected particles within the arrangement `A` (numbering of the particles follow figure 11).
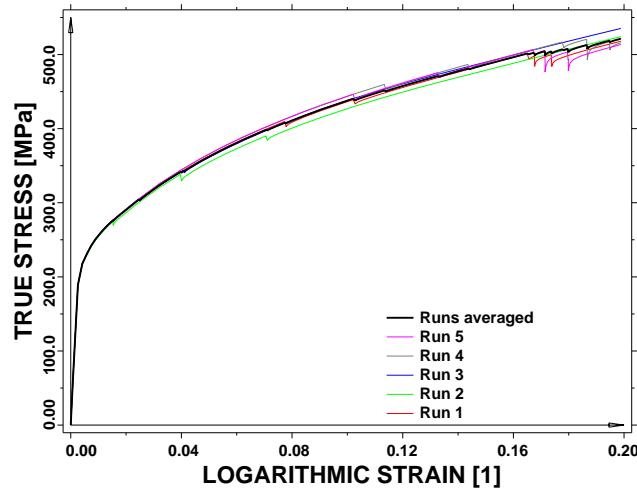
Figure 25: AA2618/SiC$^{eq}_{6.3p}$-T4–`A`/`MCW`: Predicted stress-strain curves obtained by individual runs using the `MCW`-method and phase arrangement `A` under unidirectional tensile loading in 1-direction. The ensemble average is shown by the black solid curve.
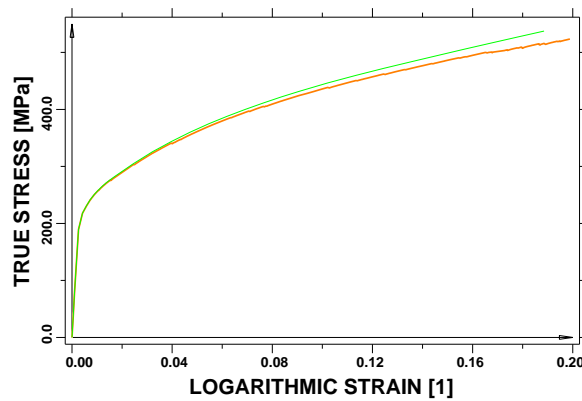
Figure 26: AA2618/SiC$^{eq}_{6.3p}$-T4–`A`/`MCW`: Predicted unidirectional tensile stress-strain behavior without particle damage (green) compared to response accounting for particle damage (orange), obtained by ensemble averaging 5 runs with arrangement `A` (compare figure 25) and five runs with arrangement `B`.
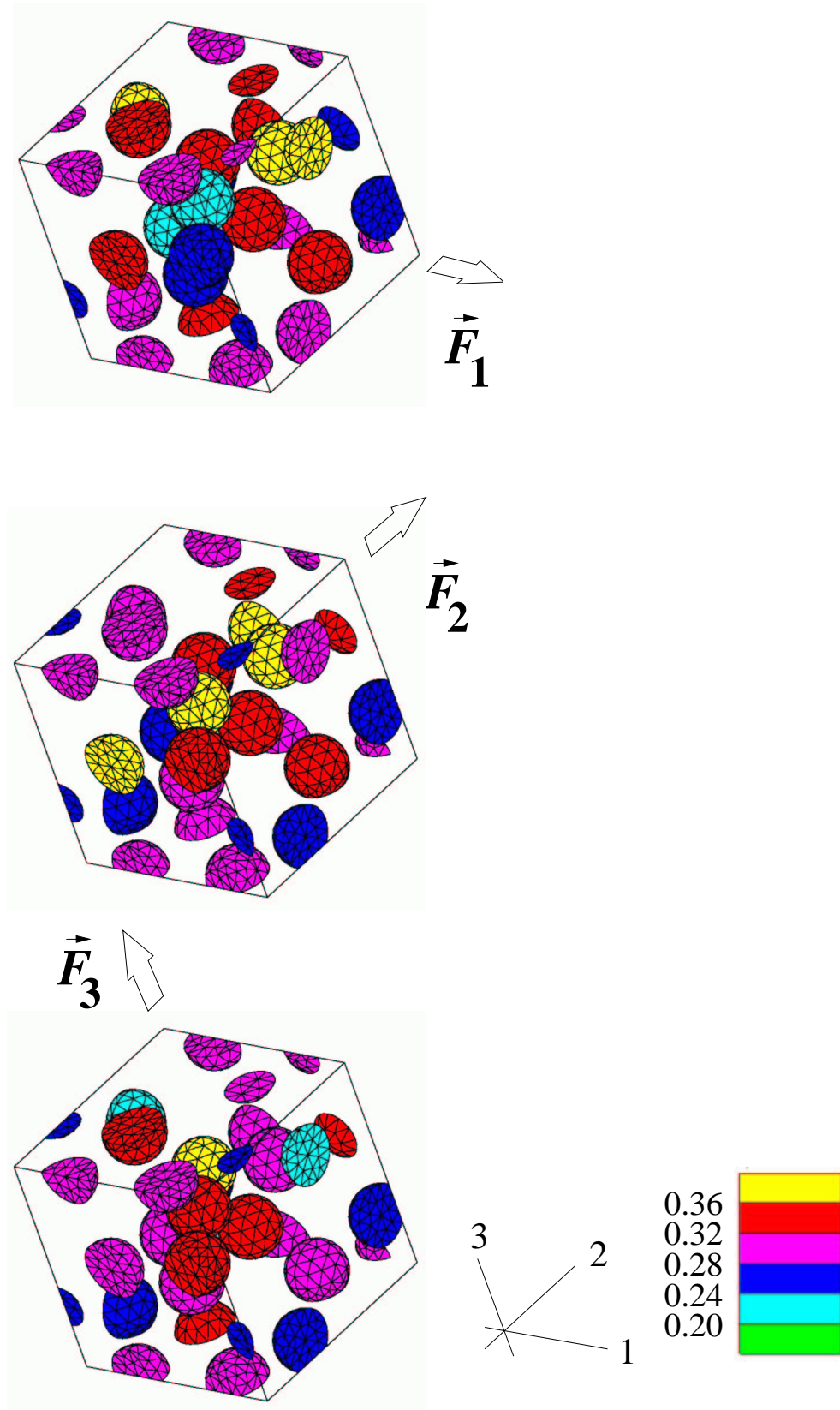
Figure 27: AA2618/SiC$^{eq}_{15p}$-T4–C: Comparison of particles' Weibull fracture probabilities due to uniaxial tensile loading in 1-, 2- and 3-directions of unit cell C. The applied strain is $\varepsilon^{a} = 0.095$ ($\sigma^{a} = 466.4$ MPa) in all three cases, and particle failure is not activated.
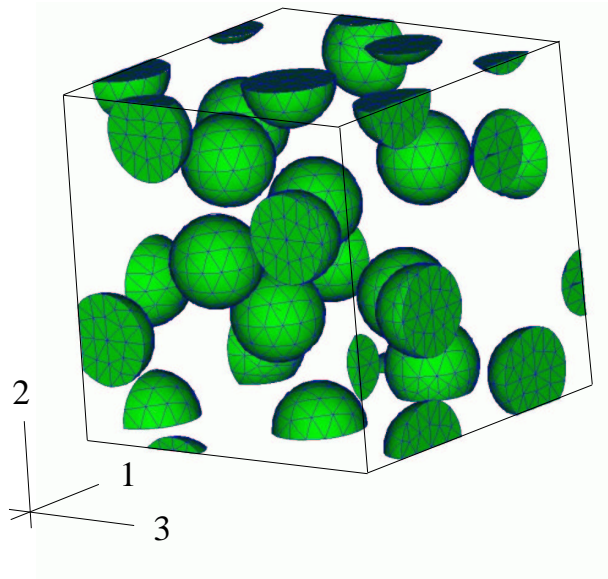
Figure 28: AA2618/SiC$_{15p}^{eq}$-T4–C/MCW: Particles in unit cell model C ($\xi = 15\%$) in unde-formed state, compare with figure 12 for designations of particles.
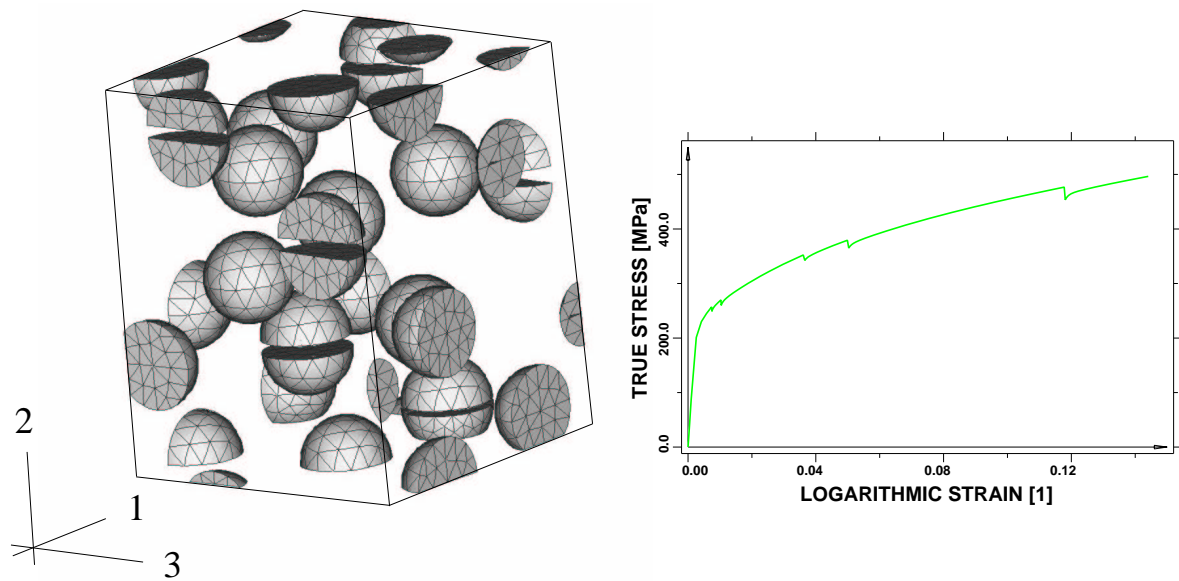
Figure 29: AA2618/SiC$_{15p}^{eq}$-T4–C/MCW: Predicted state of particles in the unit cell subjected to uniaxial tensile loading in 2-direction (applied global strain $\varepsilon^a = 0.155$, correponding to an overall stress of $\sigma^a = 496.5$ MPa) and the overall stress-strain relation obtained for this simulation. Five particles have undergone failure due to brittle fracture.
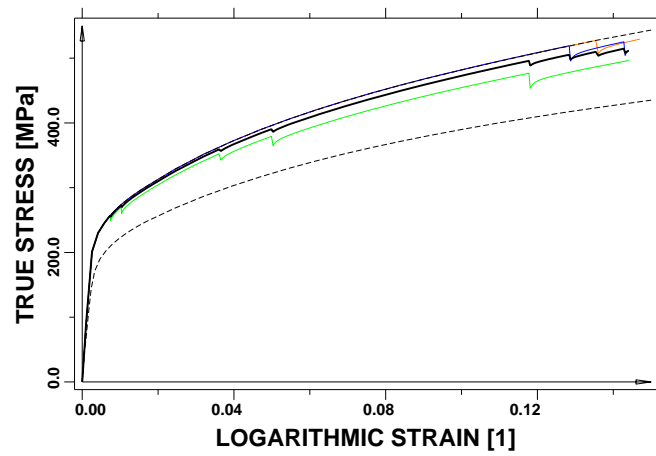
Figure 30: AA2618/SiC$_{15p}^{eq}$-T4–`C`/`MCW`: Predicted stress-strain relations and averaged stress-strain relation (solid black curve) for three different `MCW`-triggered runs of arrangement `C` loaded in 2-direction. In addition, two limiting behaviors are shown, the upper one corresponding to the case of no particle failure and the lower one to the case where all particles are cracked from the onset (dashed black curves). The end of the green curve corresponds to the particle state shown in figure 29.
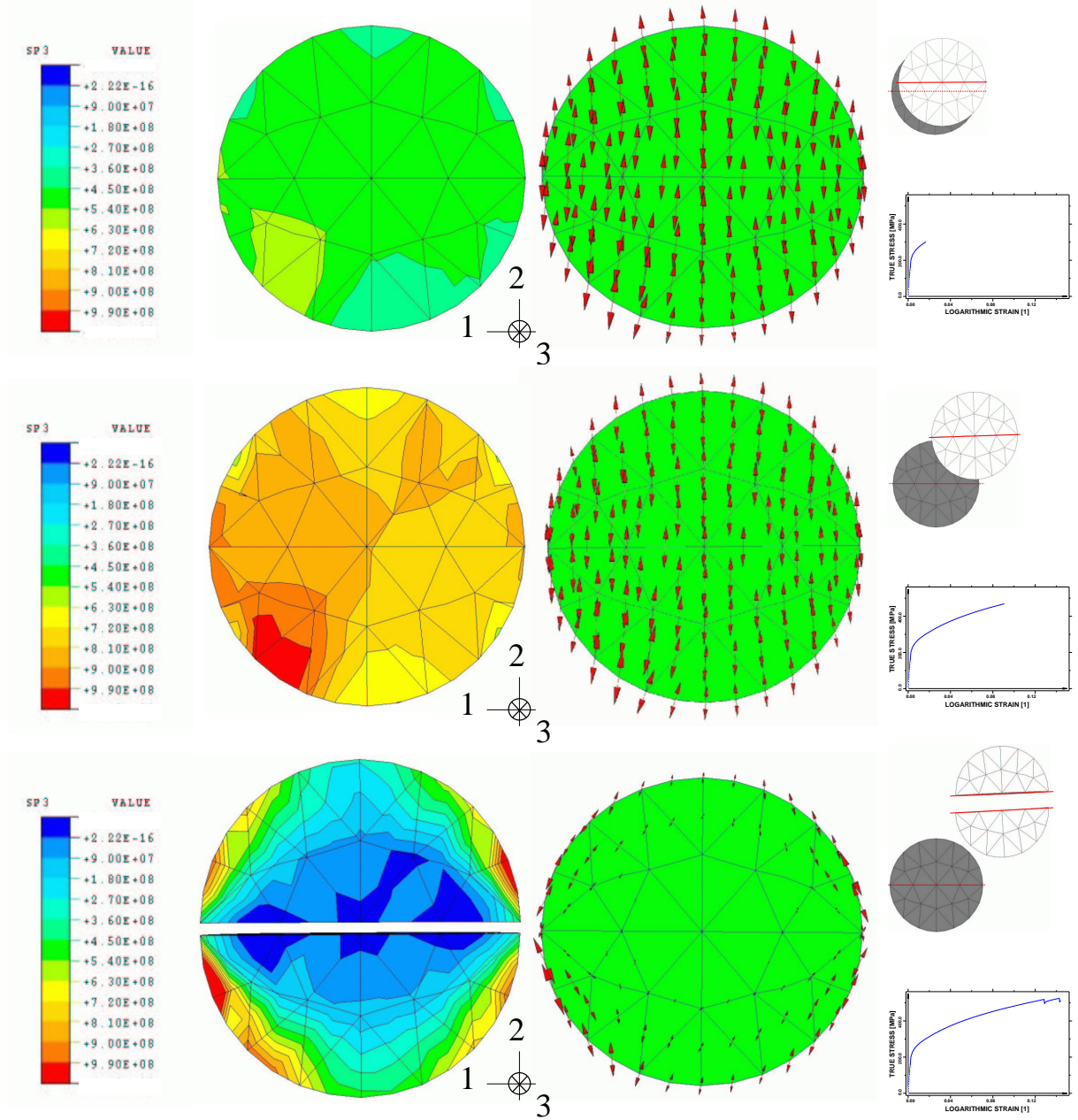
Figure 31: AA2618/SiC$_{15p}^{eq}$-T4–C/MCW: Sections through particle 3 (compare figure 12) at three states corresponding to increasing loads in global 2-direction. The maximum principal stresses are visualized by a contour plot (left) and a vector plot (center). In the right column the corresponding stress-strain curves and a sequence of the relative movements of the particle (magnification=5) with respect to the grey marked initial positions are given. The top and the center images correspond to applied strains of $\varepsilon^a = 0.017$, $\sigma^a = 301.8$ MPa, (top) and $\varepsilon^a = 0.095$, $\sigma^a = 468.8$ MPa, (center), respectively, at which the particle is intact. The bottom figure shows the final situation at a global strain of $\varepsilon^a = 0.155$, $\sigma^a = 512.3$ MPa, where the particle has failed (and the closely neighboring particle 2, too).
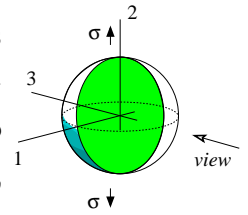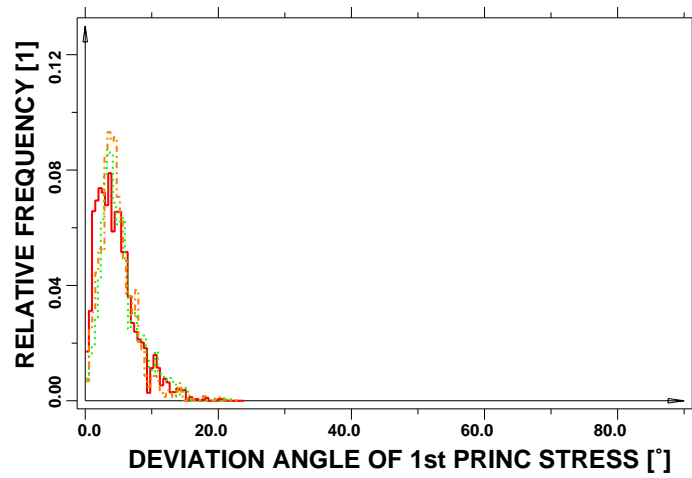
Figure 32: AA2618/SiC$_{15p}^{eq}$-T4–C/MCW: Orientation distributions of the maximum principal stresses for the closely neighboring particles 3 (red-solid), 8 (green-dashed) and 4 (orange-dotted) within arrangement C before any particle failure ($\varepsilon^a = 0.095$, $\sigma^a = 468.8$ MPa). Compare figure 12 for particle numbering.
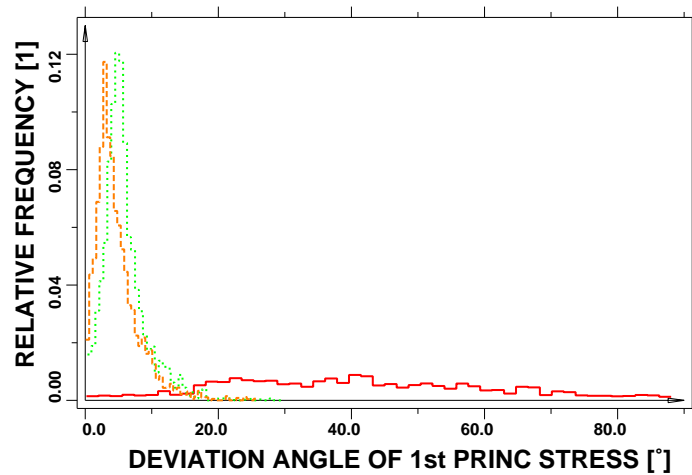
Figure 33: AA2618/SiC$_{15p}^{eq}$-T4–C/MCW: Predicted orientation distributions of the maximum principal stresses for the closely neighboring particles 3 (red-solid), 8 (green-dashed) and 4 (orange-dotted) after the failure of particles 3 and 2, the overall applied strain being $\varepsilon^a = 0.155$, and the predicted overall stress $\sigma^a = 512.3$ MPa. For particle numbering refer to figure 12.
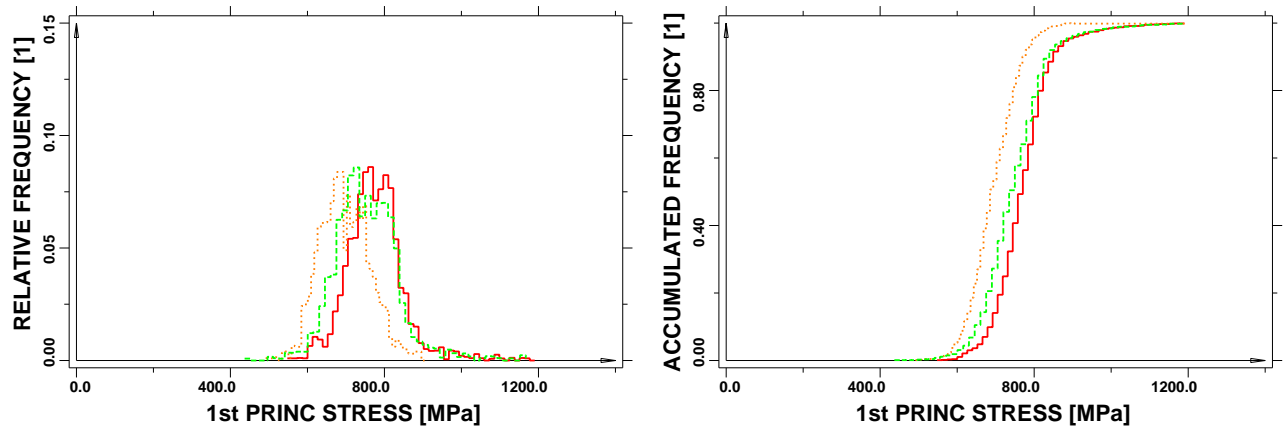
Figure 34: AA2618/SiC$_{15p}^{eq}$-T4–C/MCW: Predicted distributions of the magnitudes of the maximum principal stresses for the closely neighboring particles 3 (red-solid), 8 (green-dashed) and 4 (orange-dotted) before the failure of particle 3, ($\varepsilon^a = 0.095$, $\sigma^a = 468.8$ MPa). Compare figure 12 for particle numbering.
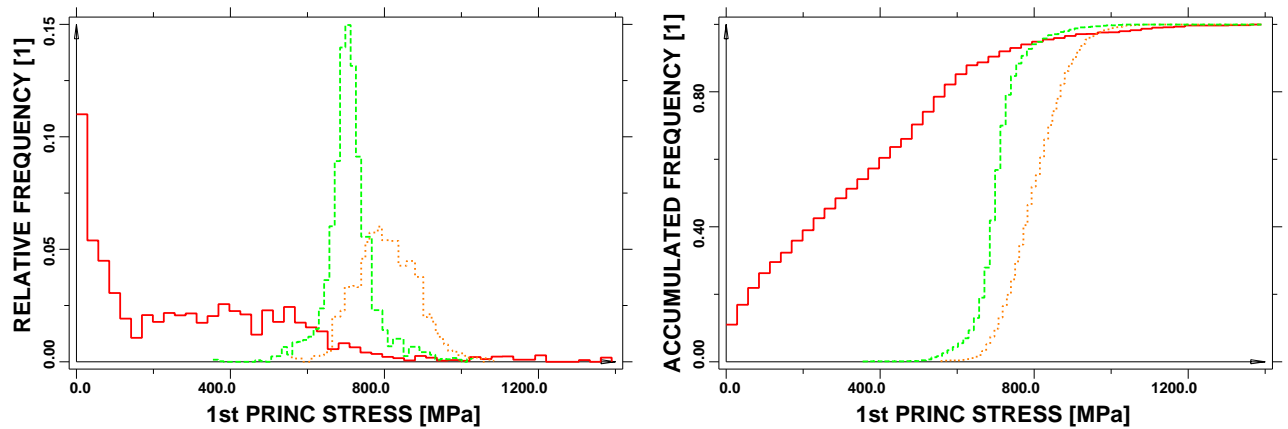
Figure 35: AA2618/SiC$_{15p}^{eq}$-T4–C/MCW: Predicted distributions of the magnitudes of the maximum principal stresses for the closely neighboring particles 3 (red-solid), 8 (green-dashed) and 4 (orange-dotted) after the failure of particle 3 ($\varepsilon^a = 0.155$, $\sigma^a = 512.3$ MPa). Compare figure 12 for particle numbering.
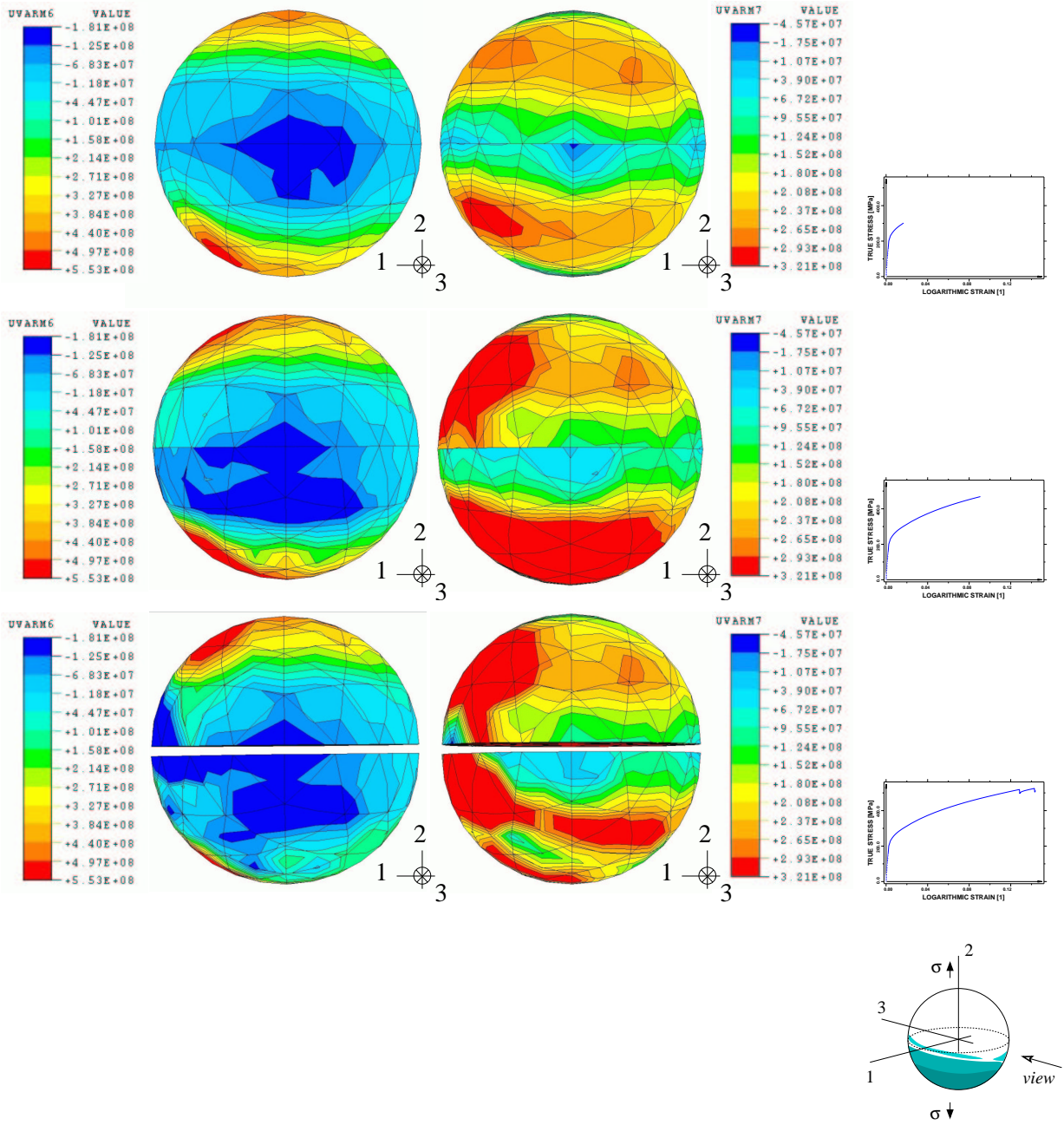
Figure 36: AA2618/SiC$_{15p}^{eq}$-T4–C/MCW: Predicted interfacial tractions for particle 3 before failure (top: $\varepsilon^a = 0.017$, $\sigma^a = 301.8$ MPa, center: $\varepsilon^a = 0.095$, $\sigma^a = 468.8$ MPa) and after failure (bottom: $\varepsilon^a = 0.155$, $\sigma^a = 512.3$ MPa). Global load applied in 2-direction. Contour plots are given for the normal component (left, with corresponding legend) and for the magnitude of the tangential components (right, with corresponding legend).
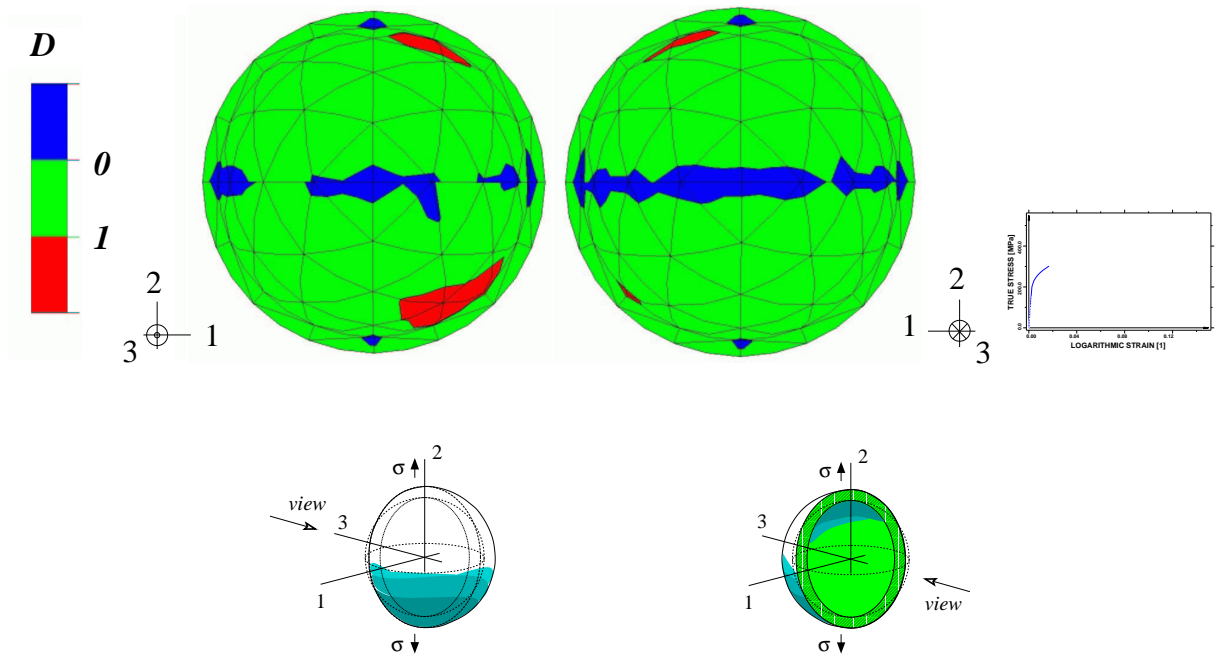
Figure 37: AA2618/SiC$_{15p}^{eq}$-T4–C/MCW: Predicted ductile damage indicator in matrix regions close to the interface of particle 3. The particle is removed, so that two halves of the resulting hole in the surrounding matrix regions are visible (consider the view orientations). Regions with $D > 1$ are expected to be subjected to ductile failure. Applied overall tensile strain in 2-direction $\varepsilon^{a} = 0.017$ (corresponding overall stress $\sigma^{a} = 301.8$ MPa).
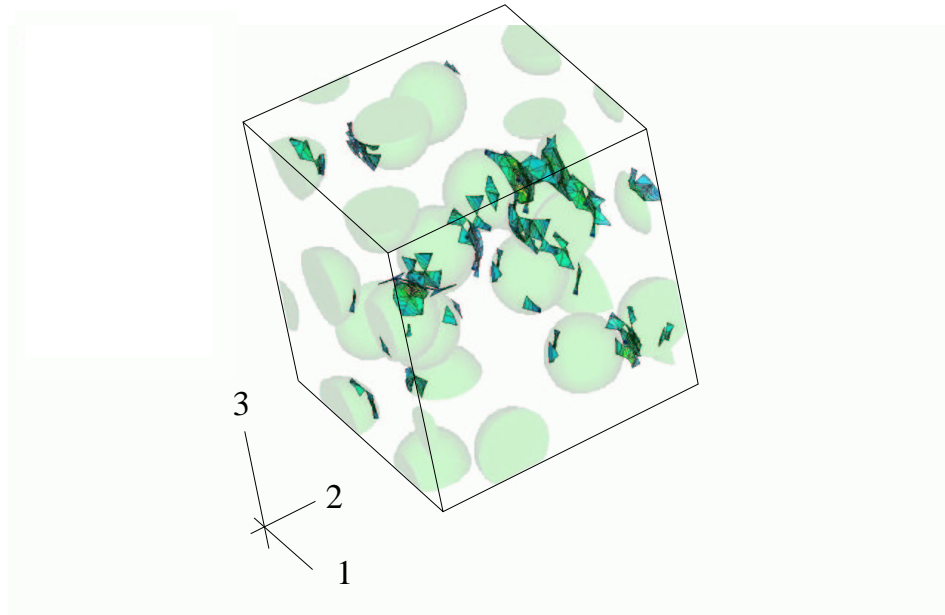
Figure 38: AA2618/SiC$_{15p}^{eq}$-T4–C/MCW: Model loaded in 2-direction at a global strain of $\varepsilon^{a} = 0.017$ ($\sigma^{a} = 301.8$ MPa) and where all particles are still intact. The elements within the model where in at least one integration point the damage indicator is $D \geq 0.90$ (thus assumed to be close to ductile failure) are shown.
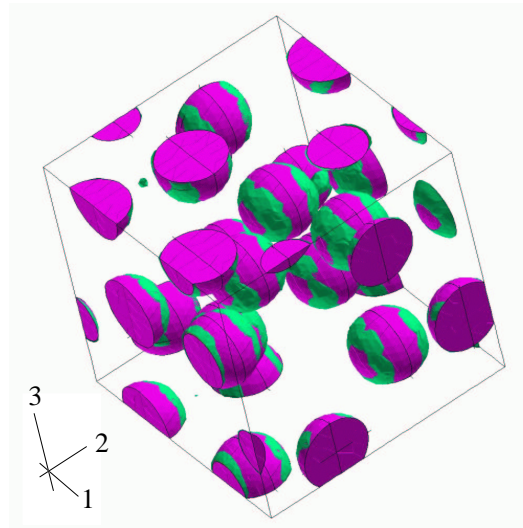
Figure 39: AA2618/SiC$_{15p}^{eq}$-T4–C/MCW: Model loaded in 2-direction at a global strain of $\varepsilon^{a} = 0.017$ ($\sigma^{a} = 301.8$ MPa) and where all particles are still intact. Isosurfaces of equivalent plastic strain $\varepsilon_{eq,p} = 0.053$, green surfaces (the maximum value in the model evaluated as $\varepsilon_{eq,p} = 0.165$). Note that particles are shown in magenta.
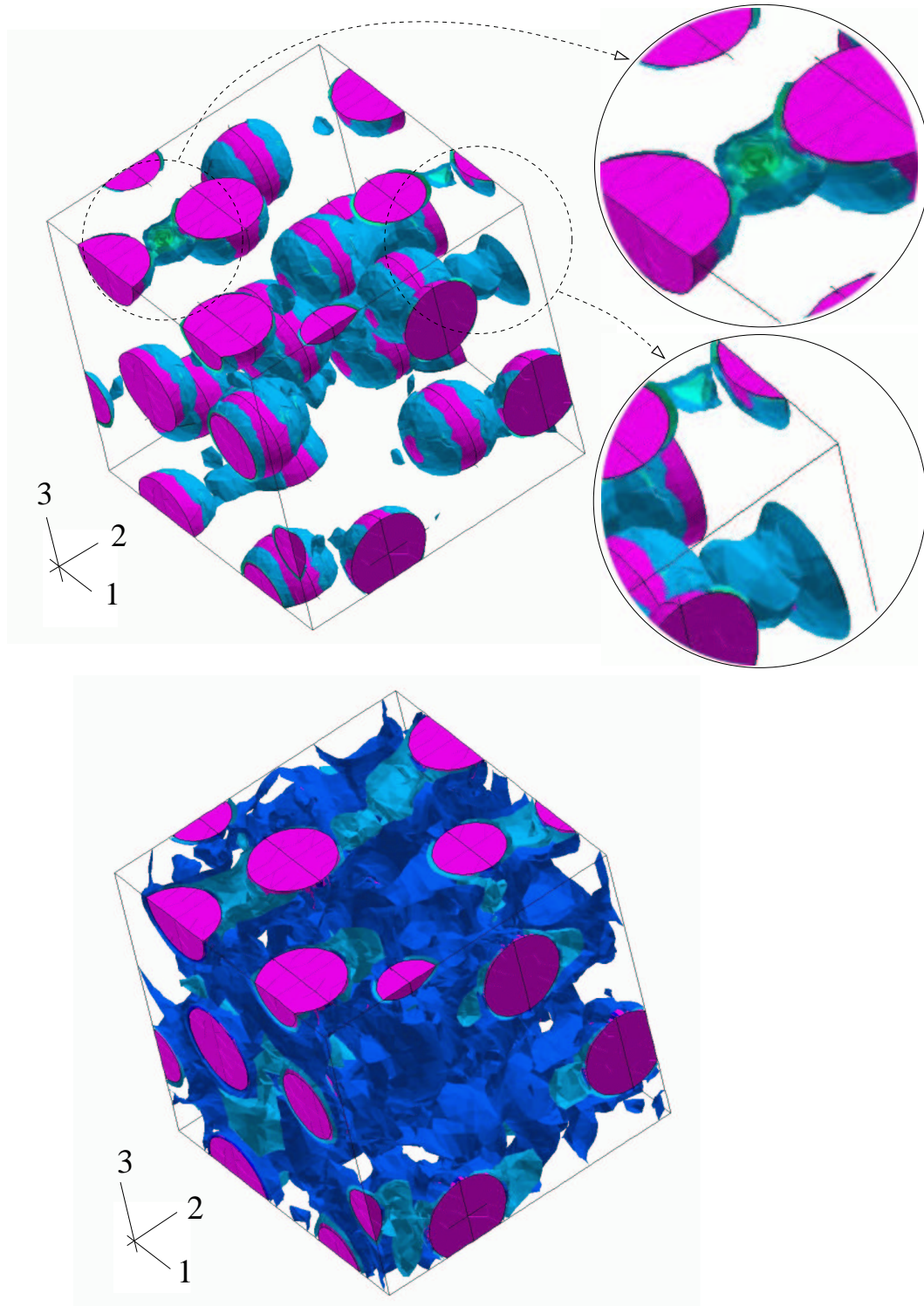
Figure 40: AA2618/SiC$_{15p}^{eq}$-T4–C/MCW: Model loaded in 2-direction at a global strain of $\varepsilon^{a} = 0.017$ ($\sigma^{a} = 301.8$ MPa) and where all particles are still intact. Series of five isosurfaces of the equivalent plastic strain running from $\varepsilon_{eq,p} = 0.031$ (light blue) to $\varepsilon_{eq,p} = 0.053$ (light green, corresponding to figure 39) in the upper plot and from $\varepsilon_{eq,p} = 0.0006$ (dark blue) to $\varepsilon_{eq,p} = 0.031$ (light blue) in the lower plot.
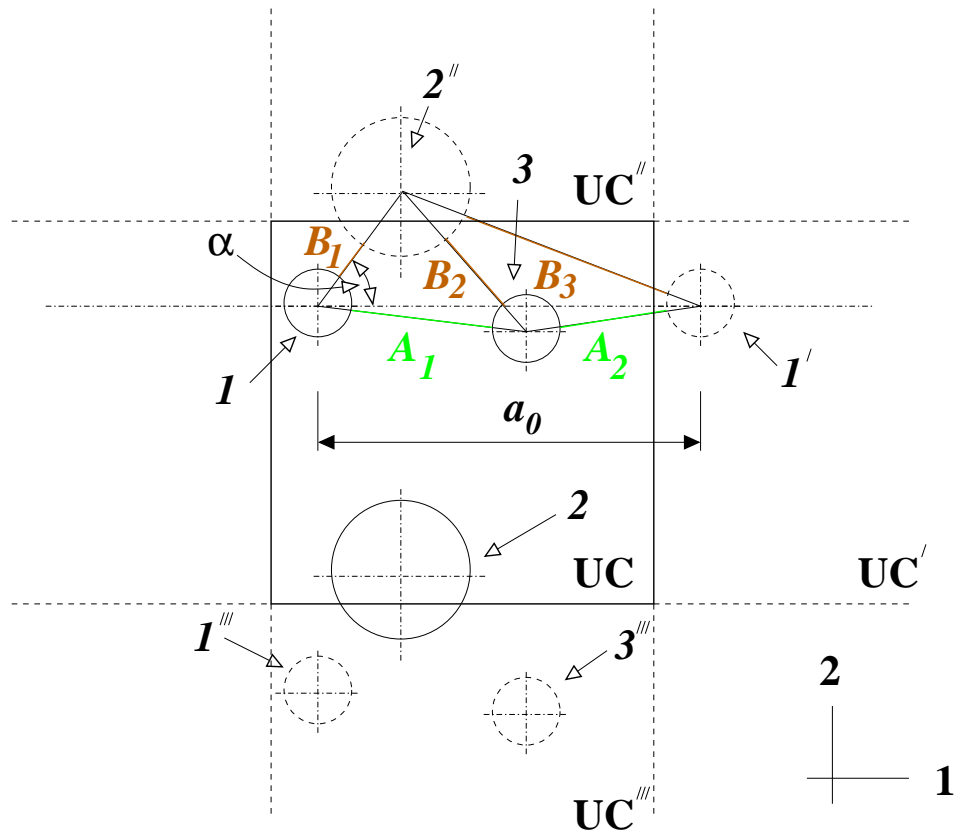
Figure 41: Schematic image (for periodically arranged unit cells UC of length a_0 in two dimensions) explaining the particle distance evaluation as described in the text.
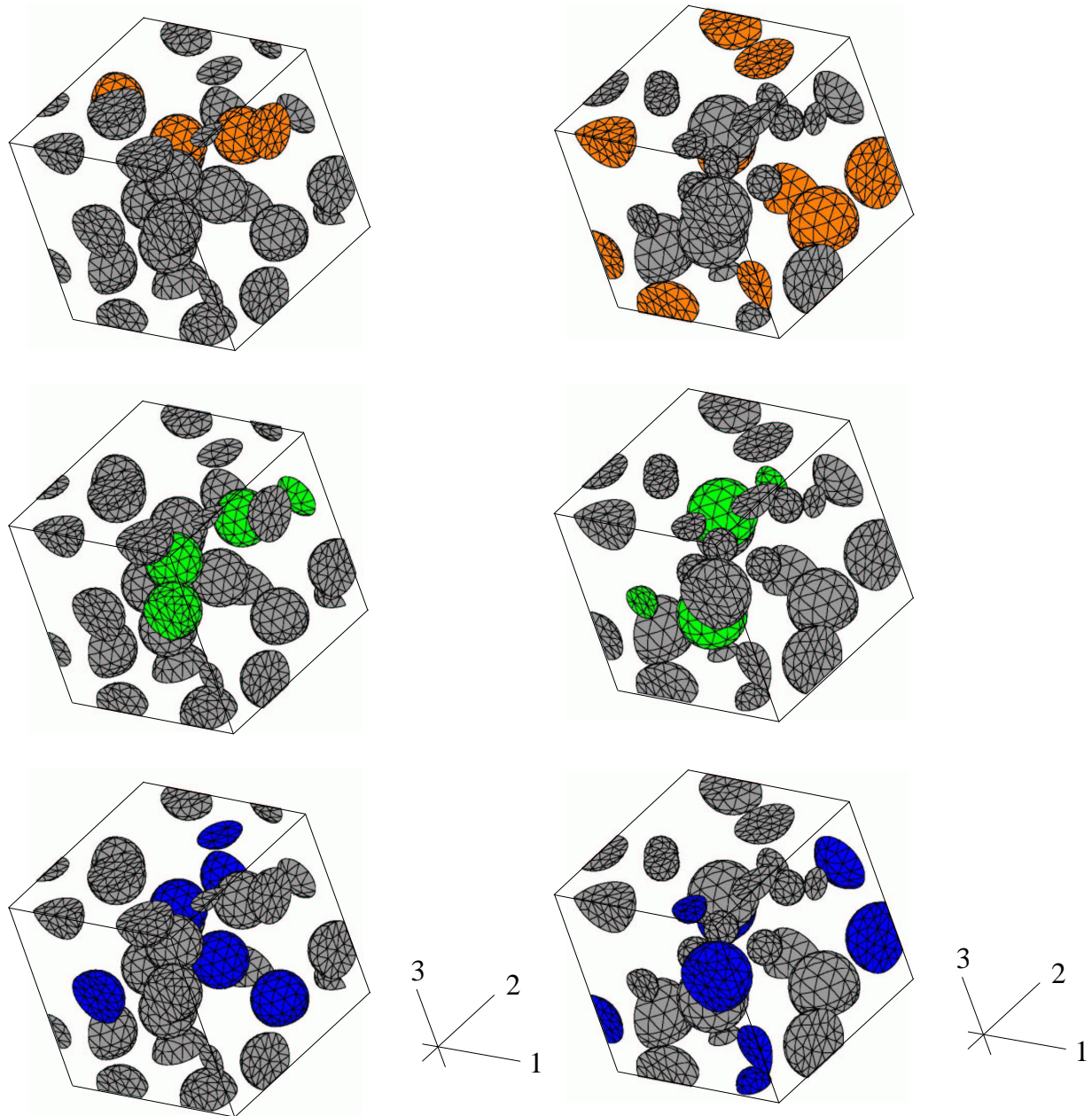
Figure 42: Shortest interparticle distances for unit cell `C` (left column) and for unit cell `E` (right column). The inclusions, lying on the "string" of smallest length, with respect to the overall loading direction, are colored: orange color corresponds to loading in 1-direction (top), green color corresponds to loading in 2-direction (center) and blue to loading in 3-direction (bottom), respectively. For further discussions see text.
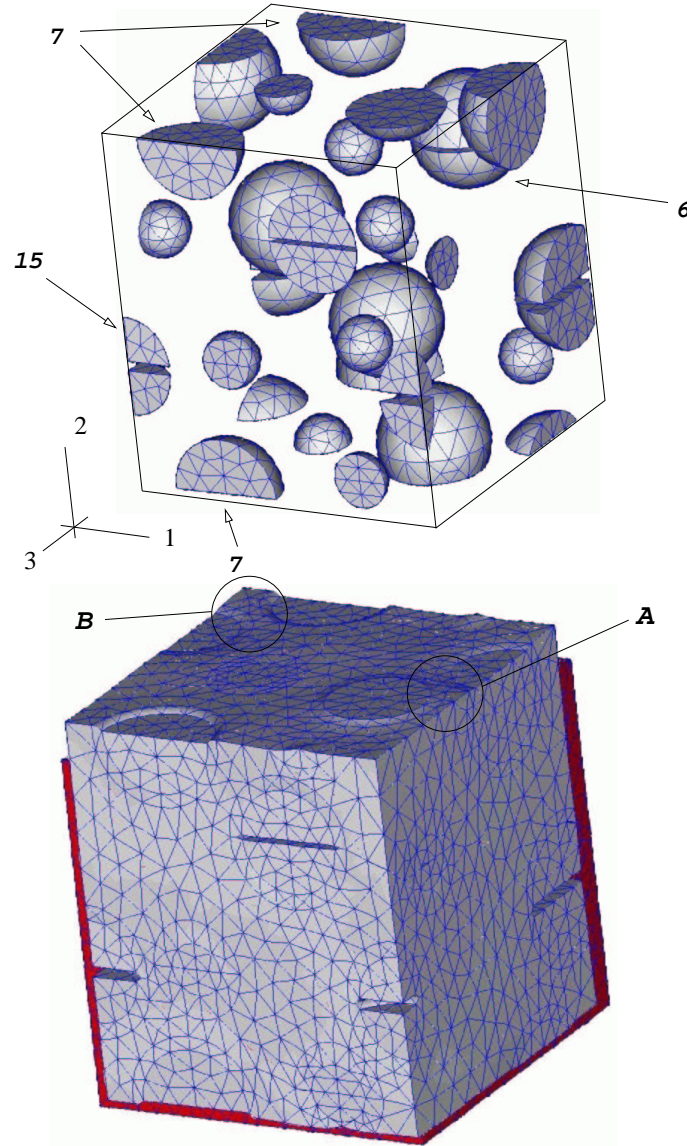
Figure 43: AA2618/SiC$_{15p}^{bi}$-T4–E/MCW: Particles in unit cell arrangement E after global uniaxial tensile loading in 2-direction to an overall strain of $\varepsilon^{a} = 0.095$ ($\sigma^{a} = 468.8$ MPa); for the corresponding stress-strain relation see figure 47, green curve. Particles 6, 7 and 15 have failed during the load history. Note that in this unit cell model particle 7 happens to be positioned such that the fracture surface is identical with a face of the unit cell.
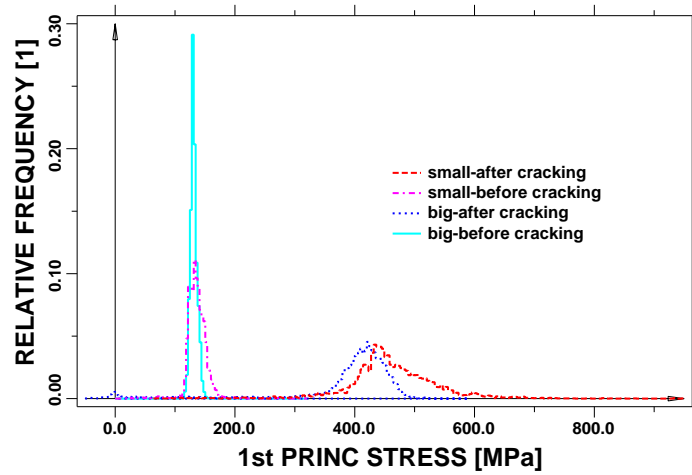
Figure 44: AA2618/SiC$_{15p}^{bi}$-T4–`E`/`MCW`: Predicted relative frequencies of the maximum principal stresses within the particles of model `E` in the elastic range (global strain in 2-direction $\varepsilon^{\mathrm{a}} = 0.001$ ($\sigma^{\mathrm{a}} = 86.7$ MPa)) and after (global strain in 2-direction $\varepsilon^{\mathrm{a}} = 0.017$ ($\sigma^{\mathrm{a}} = 288.2$ MPa)) the failure of some particles. The green curve in figure 47 shows the corresponding stress-strain behavior.
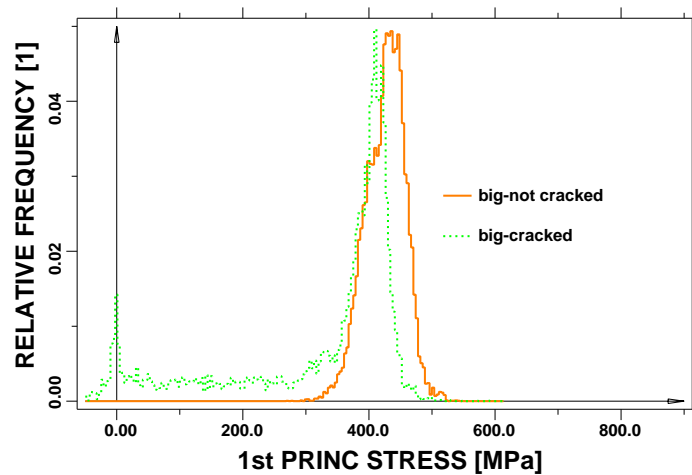
Figure 45: AA2618/SiC$_{15p}^{bi}$-T4–`E`/`MCW`: Predicted relative frequencies of maximum principal stresses within the failed and within the intact big particles of the model at an overall tensile strain in 2-direction of $\varepsilon^{\mathrm{a}} = 0.017$ ($\sigma^{\mathrm{a}} = 288.2$ MPa), see also figure 44.
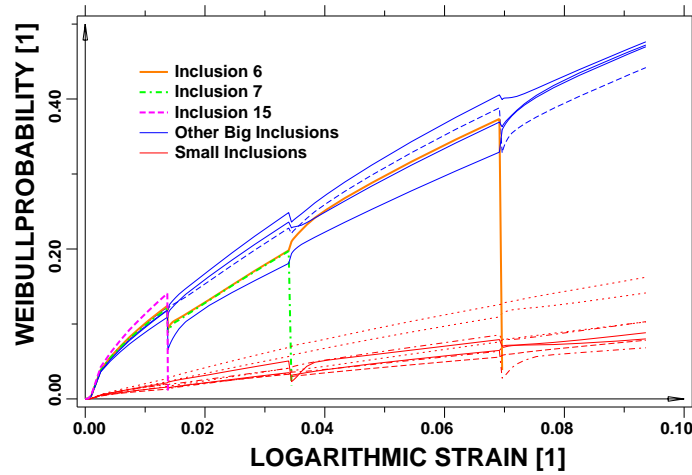
Figure 46: AA2618/SiC$_{15p}^{bi}$-T4–`E`/`MCW`: Predicted evolution of the Weibull fracture probabilities of the 15 particles in the model for applied tensile strains up to $\varepsilon^a = 0.095$ ($\sigma^a = 430.1$ MPa). Inclusions `6`, `7` and `15` (for designations see figure 43) fail during the loading process, the stress-strain diagram of which is shown as a green line in figure 47.
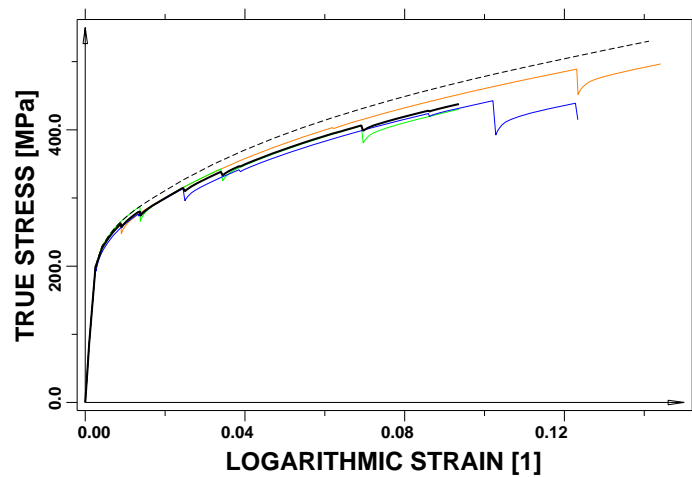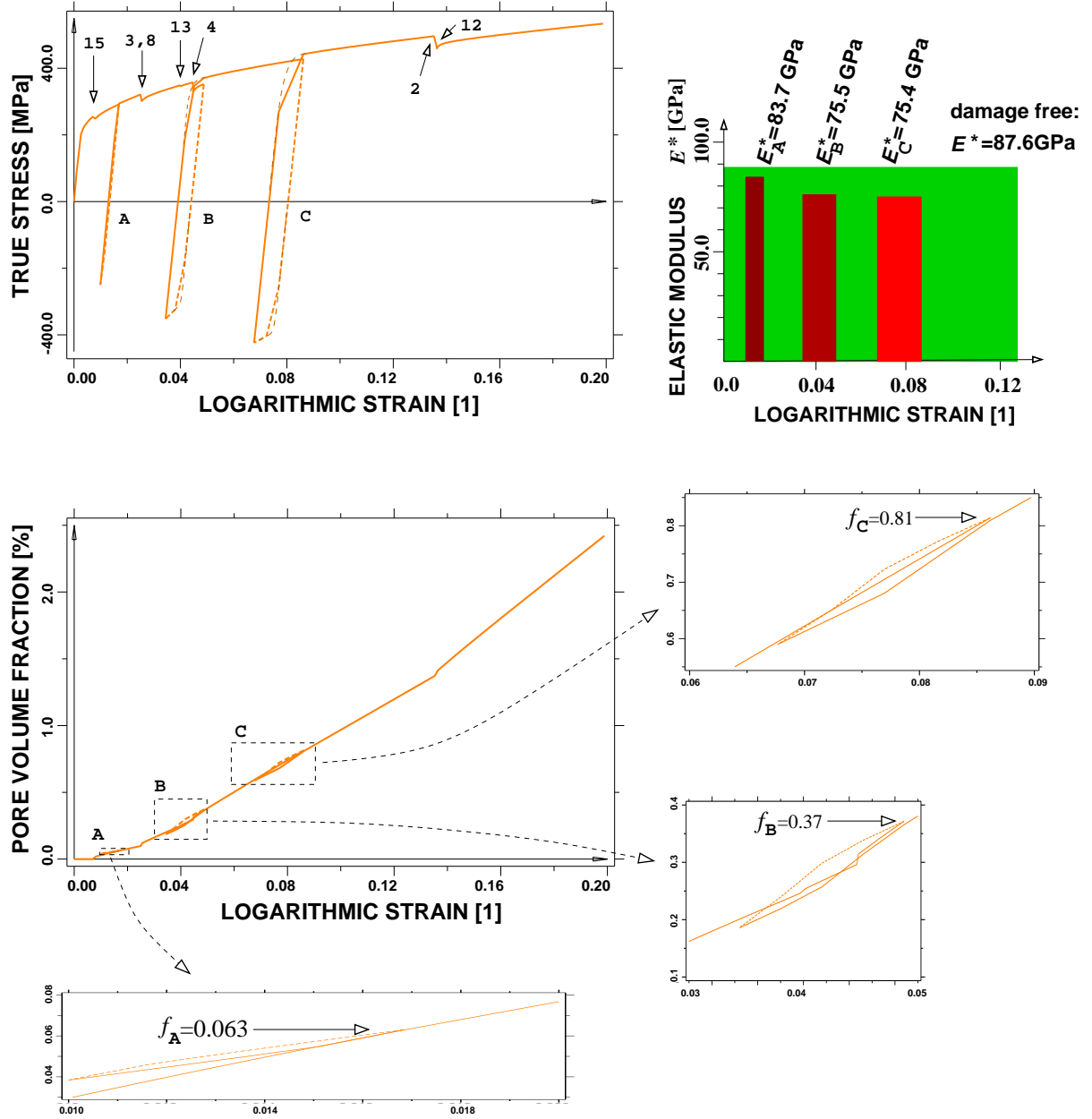

Figure 47: AA2618/SiC$_{15p}^{bi}$-T4–`E`/`MCW`: Stress-strain relations predicted with unit cell `E` for uniaxial tensile loading in 1-direction (orange), in 2-direction (green) and in 3-direction (blue). The averaged curve is shown in black and the damage-free curve is displayed as a dashed line.
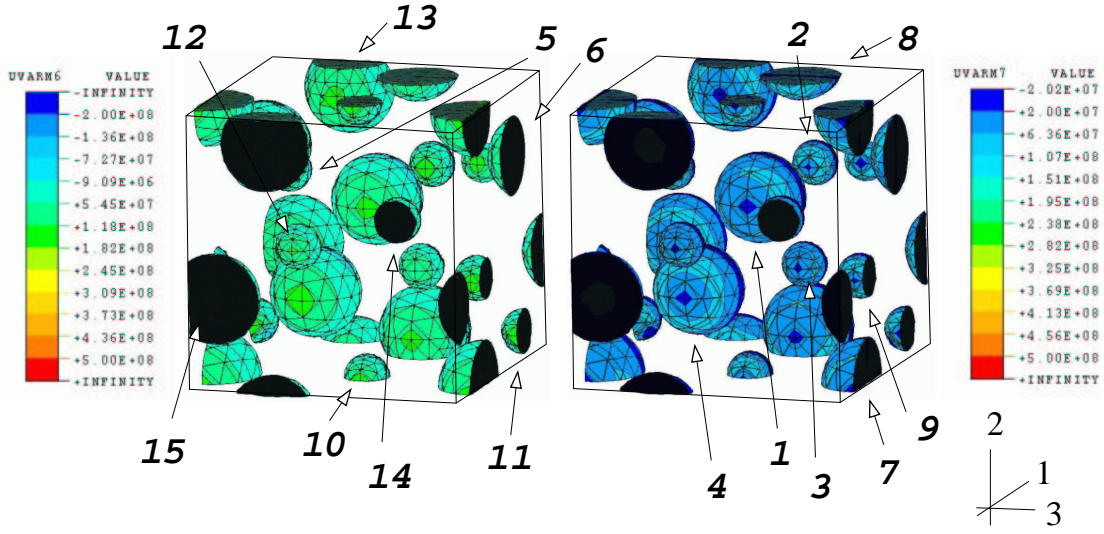
Figure 48: AA2618/SiC$_{15p}^{bi}$-T4–E/MCW: Predicted normal components (left) and magnitudes of the tangential components (right) of the interfacial tractions at the particle surfaces at an applied strain in 1-direction of $\varepsilon^{\mathrm{a}} = 0.001$, $\sigma^{\mathrm{a}} = 86.6$ MPa. The situation corresponds to the elastic range.
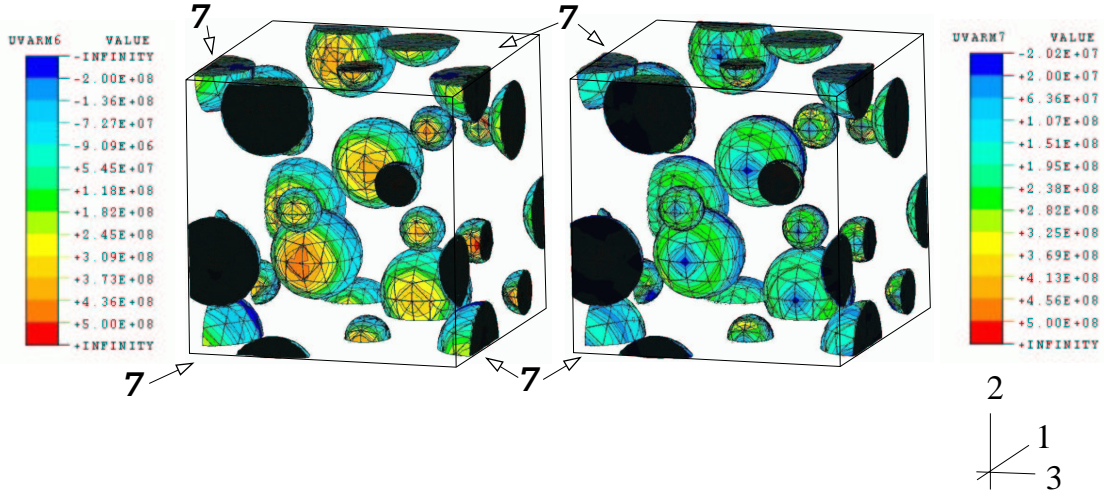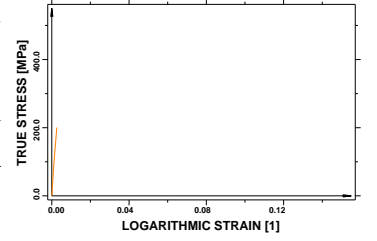
Figure 49: AA2618/SiC$_{15p}^{bi}$-T4–E/MCW: Predicted normal components (left) and magnitudes of the tangential components (right) of the interfacial tractions at the particle surfaces at an applied strain in 1-direction of $\varepsilon^{\mathrm{a}} = 0.017$, $\sigma^{\mathrm{a}} = 289.8$ MPa. At this point particle 7 has just failed and there is some matrix yielding.
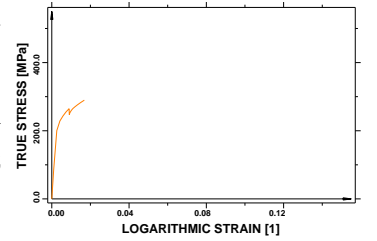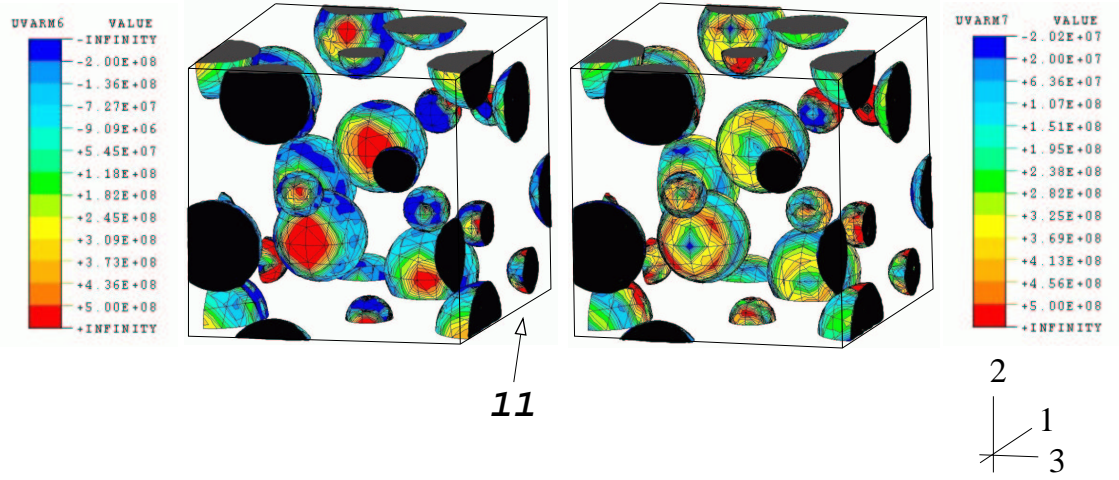
Figure 50: AA2618/SiC$^{bi}_{15p}$-T4–E/MCW: Predicted normal components (left) and magnitudes of the tangential components (right) of the interfacial tractions at the particle surfaces at an applied strain in 1-direction of $\varepsilon^a = 0.095$, $\sigma^a = 447.9$ MPa. At this point particle 11, a small inclusion, has just failed and there is large scale matrix yielding.
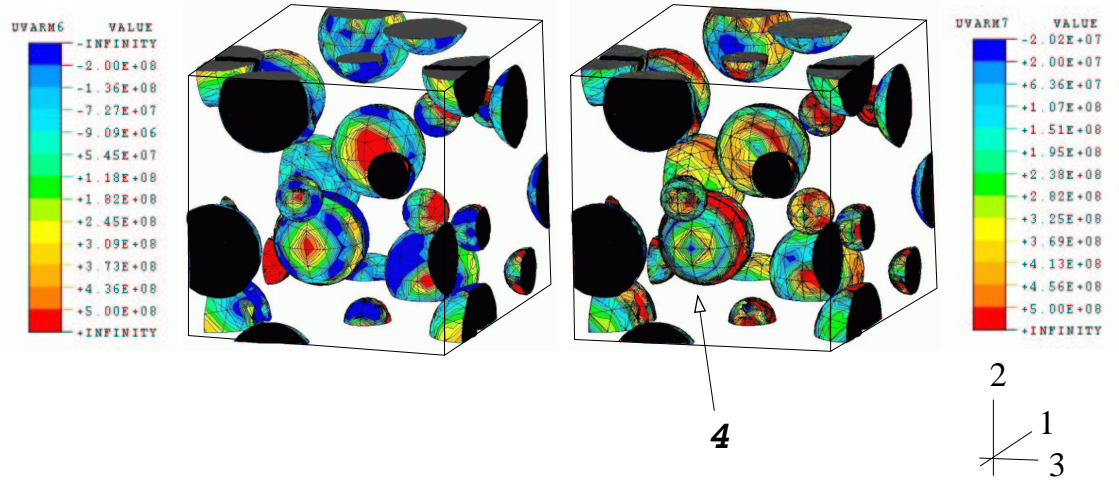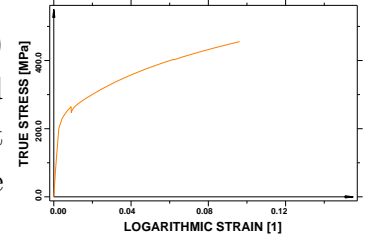
Figure 51: AA2618/SiC$^{bi}_{15p}$-T4–E/MCW: Predicted normal components (left) and magnitudes of the tangential components (right) of the interfacial tractions at the particle surfaces at an applied strain in 1-direction of $\varepsilon^a = 0.155$, $\sigma^a = 469.6$ MPa. Both images correspond to the final point of this simulation run, where also the big particle 4 has undergone failure.
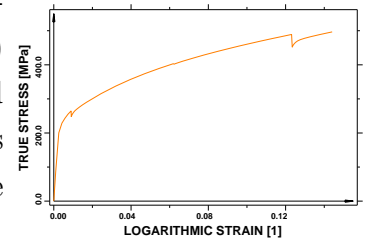
Figure 52: AA2618/SiC$^{bi}_{15p}$-T4–F/MCW: Stress-strain relations predicted with unit cell F for uniaxial tensile loading in 2-direction (top left), corresponding reductions of the composite's elastic modulus being depicted in a bar diagram (top right), and predicted evolution of pore volume fraction (bottom) in the course of the uniaxial loading-unloading-sequences. The dashed parts of the curves display overall unloading sequences, which were introduced at uniaxial strains of $\varepsilon^a_A = 0.017$, $\varepsilon^a_B = 0.05$ and $\varepsilon^a_C = 0.09$ (the corresponding pore volume fractions, f_A, f_B and f_C, are given). The thinner dashed lines mark the expected stress-strain curves, which would be obtained with smaller incrementation steps during the simulation runs. The maximum homogenized stress, $\sigma^a = 533.8$MPa, was reached in this simulation at the overall strain of $\varepsilon^a = 0.22$ (the pore volume fraction being $f_v = 2.42\%$ at this state).
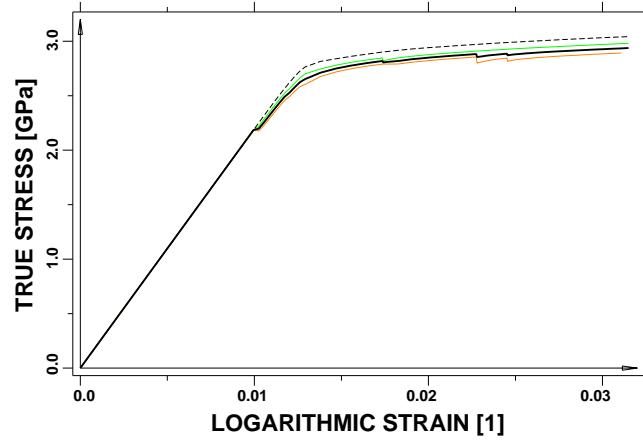
Figure 53: $\text{HSS}^{\mu 1}_{6.3\%}$–arrangements `A` and `B`/`MCW`: Predicted overall stress-strain behavior of HSS containing uniformly sized spherical carbides (black): Average out of four simulations using arrangement `A` (orange, average of two runs) and arrangement `B` (green, average of two runs). The dashed black curve represents the materials' uniaxial stress-strain behavior when particle cleavage is suppressed.
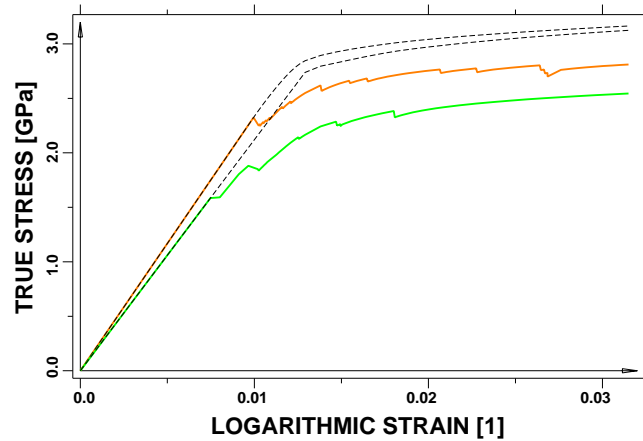
Figure 54: $\text{HSS}^{\mu 2}_{15\%}$–`C`/`MCW` and $\text{HSS}^{\mu 3}_{15\%}$–`C`/`MCW`: Predicted overall stress-strain behavior of HSS containing uniformly sized spherical carbides. Orange curve: particles of type `carbide A` ("$\text{HSS}^{\mu 2}_{15\%}$") — Green curve: particles of type `carbide B` ("$\text{HSS}^{\mu 3}_{15\%}$"), refer to table 11. The curves are averages of three simulations in both cases and the black dashed curves show the behavior when particle cleavage is suppressed.
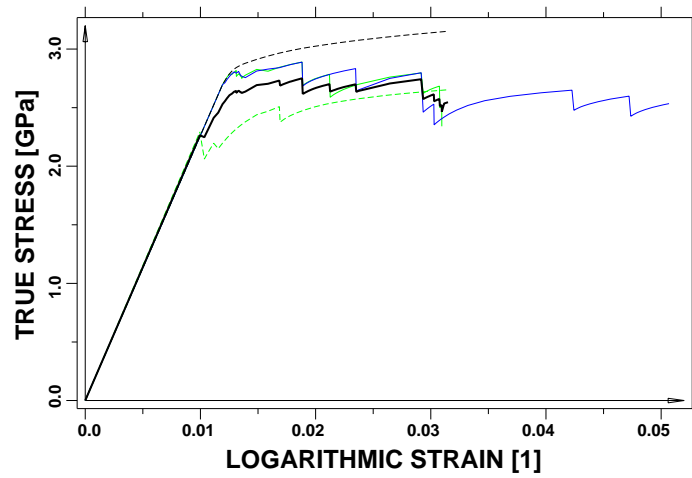
Figure 55: $\text{HSS}^{\mu4}_{15\%}$–`E`/`MCW`: Predicted overall stress-strain response using model `E` (big particles are of type `carbide A`, $\xi_{\text{big}} = 13$ vol.%, small particles are of type `carbide B`, $\xi_{\text{small}} = 2$ vol.%). Green curves: loading in 2-direction, blue curve: loading in 3-direction, black: averaged response, black dashed curve: particle cleavage suppressed.
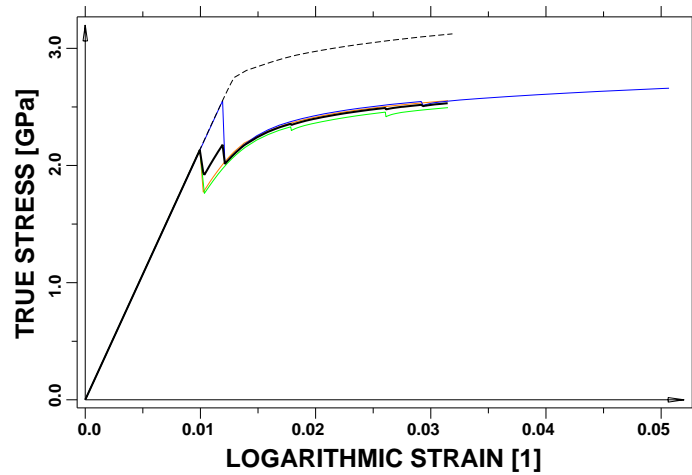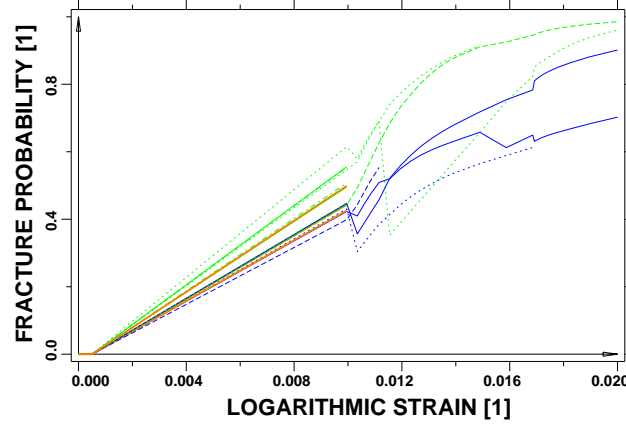

Figure 56: $\text{HSS}^{\mu5}_{15\%}$–`E`/`MCW`: Predicted overall stress-strain response using model `E` (big particles are of type `carbide B`, $\xi_{\text{big}} = 13$ vol.%, small particles are of type `carbide A`, $\xi_{\text{small}} = 2$ vol.% modeled). Orange: Loading in 1-direction, green: loading in 2-direction, blue: loading in 3-direction, black: averaged response, black dashed curve: particle cleavage suppressed.

Figure 57: $\text{HSS}^{\mu 4}_{15\%}$–E/MCW: Evolution of the Weibull fracture probabilities corresponding to the particles within model E with particle material properties coupled to particle size. Blue: big particles of material type `carbide A`, $\xi_{\text{big}} = 13$ vol.%, green: small particles of type `carbide B`, $\xi_{\text{small}} = 2$ vol.% modeled, orange: first failing big particles, see text.
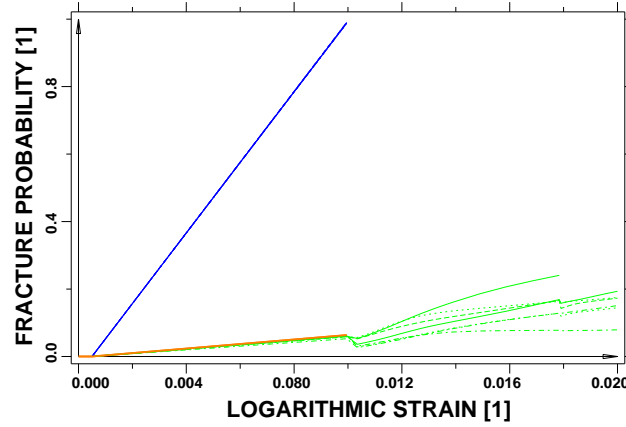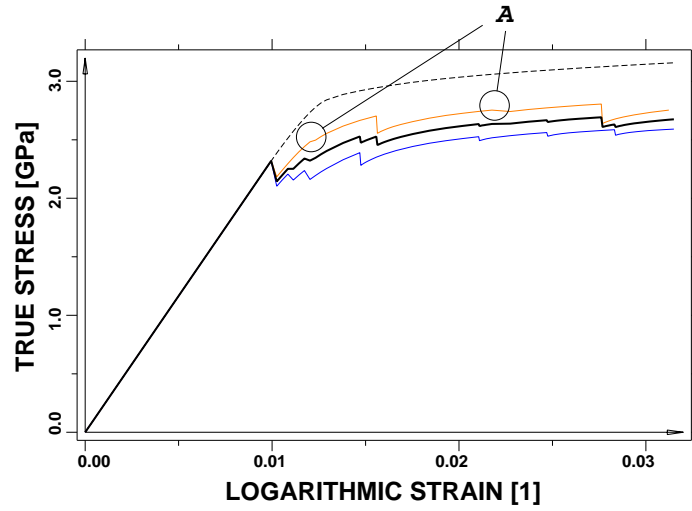

Figure 58: $\text{HSS}^{\mu 5}_{15\%}$–E/MCW: Evolution of the Weibull fracture probabilities corresponding to the particles within model E with particle material properties coupled to particle size. Blue: big particles are of type `carbide B`, $\xi_{\text{big}} = 13$ vol.%, green: small particles are of type `carbide A`, $\xi_{\text{small}} = 2$ vol.% modeled, orange: first failing big particles, see text.

Figure 59: HSS$_{15\%}^{\mu 6}$–E/MCW: Predicted overall stress-strain behavior of HSS with differently sized particles of same material type, `carbide A`. Orange curve: uniaxial loading in 1-direction, blue curve: loading in 3-direction, black curve: average response, dashed curve: particle cleavage suppressed.
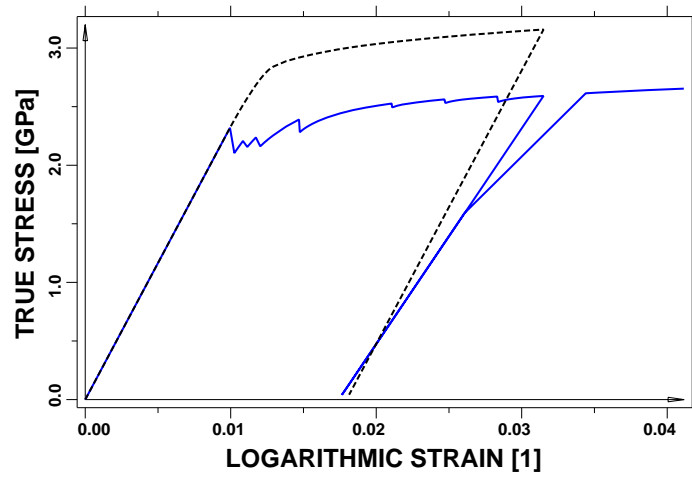

Figure 60: HSS$_{15\%}^{\mu 6}$–E/MCW: Predicted overall stress-strain behavior for a loading-unloading-loading process applied to arrangement `E` with particles of type `carbide A` (dashed black curve: particle cleavage suppressed – blue curve: loading in 3-direction).
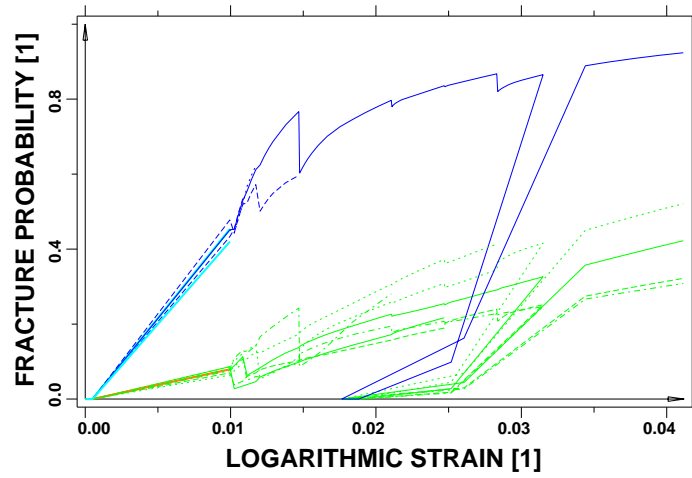
Figure 61: HSS$_{15\%}^{\mu 6}$–E/MCW: Weibull fracture probability evolution of big (blue curves; the solid blue curve refers to particle 13) and small (green curves) particles (corresponding to the blue colored stress-strain behavior in figure 60). The particle fracture probability of the first failing particles are drawn as cyan (big particles) and as orange (small particle) curves, respectively.
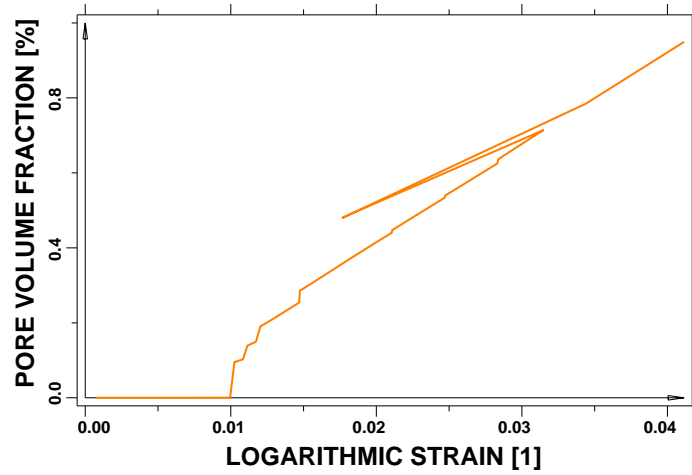

Figure 62: HSS$_{15\%}^{\mu 6}$–E/MCW: Predicted evolution of pore volume fraction in the course of the loading-unloading-loading process, corresponding stress-strain behavior is depicted in figure 60.
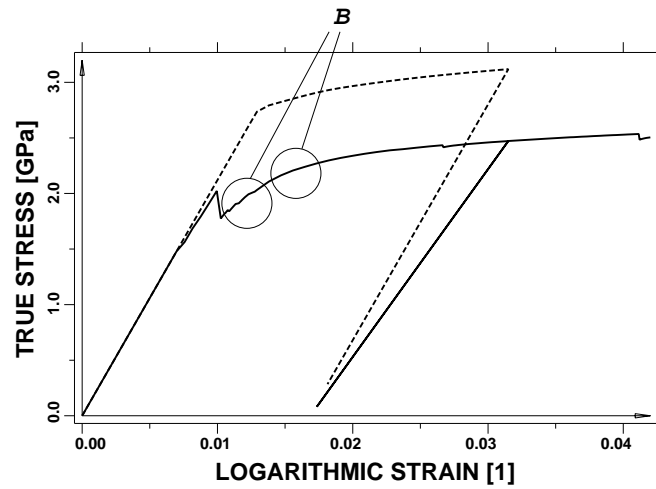
Figure 63: $\mathrm{HSS}_{15\%}^{\mu 7}$–`E/MCW`: Predicted overall stress-strain behavior of HSS with bidispersely sized paricles of material type `carbide` B. At a uniaxial strain of about $\varepsilon^{\mathrm{a}} = 0.032$ the material is unloaded and reloaded again. Black solid curve: Average of responses obtained for loading in 1-, 2- and 3-directions. Dashed curve: particle cleavage suppressed.
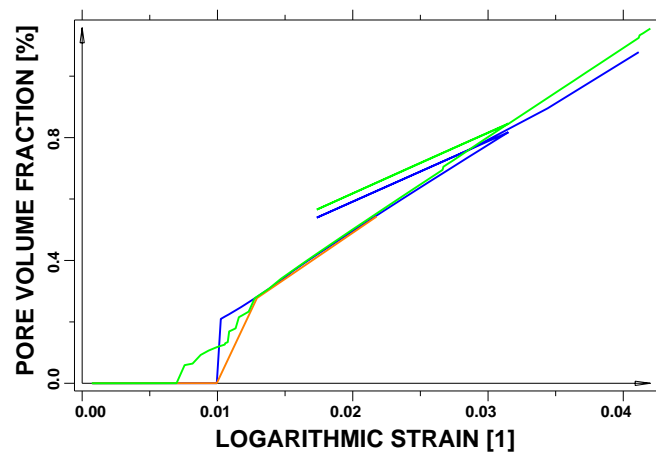

Figure 64: $\mathrm{HSS}_{15\%}^{\mu 7}$–`E/MCW`: Predicted evolution of pore volume fraction in the course of the uniaxial loading-unloading-loading processes in 1(orange curve)-, 2(green curve)- and 3(blue curve)-directions, of which the averaged stress-strain relation is shown in figure 63.
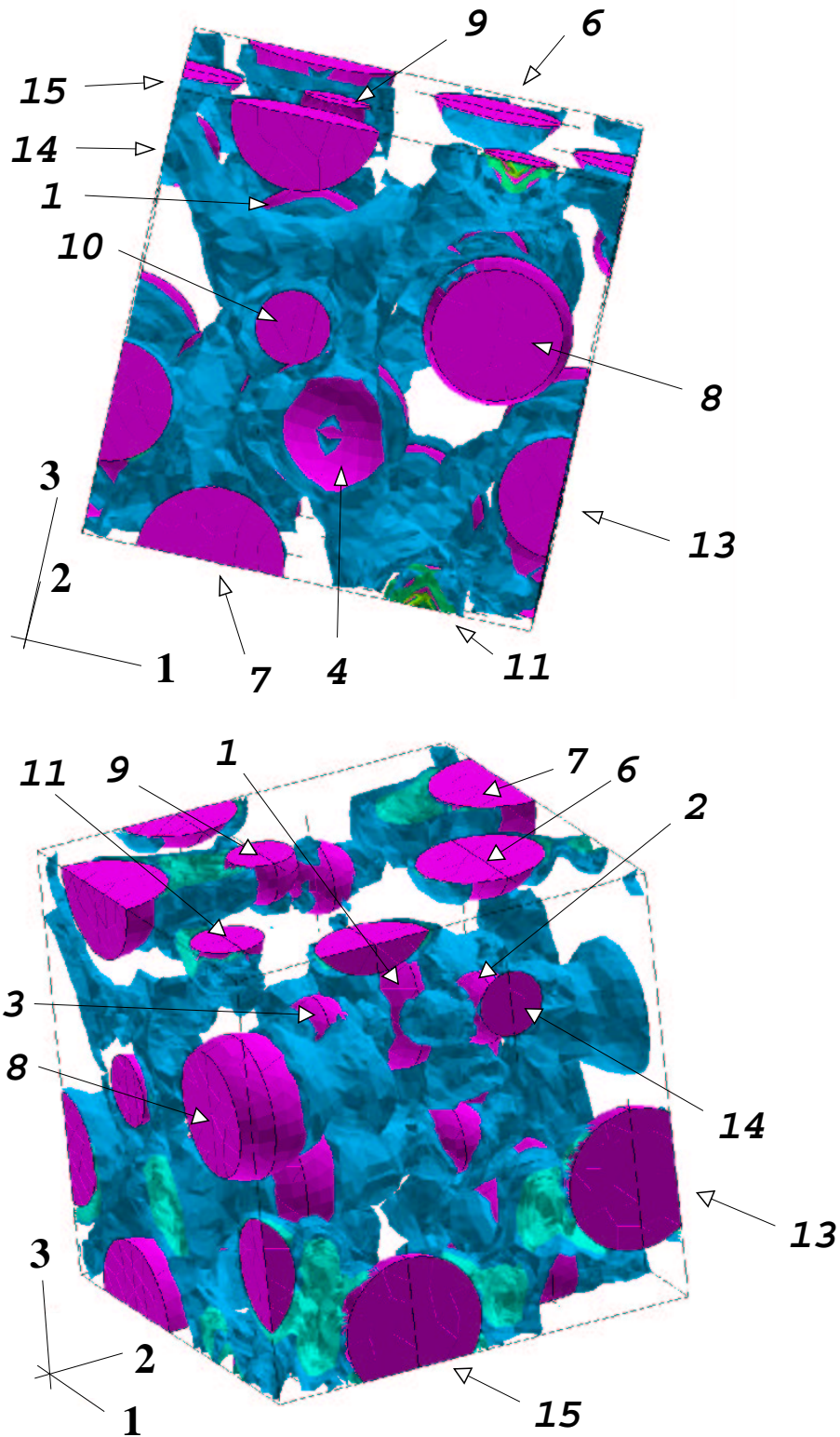
Figure 65: $\text{HSS}^{\mu 7}_{15\%}$–E/MCW: Equivalent plastic strain isosurfaces within the damage-free model after loading in 2-direction up to overall tensile strain of $\varepsilon^{\text{a}} = 0.032$, corresponding to an overall stress of $\sigma^{\text{a}} = 3.12$ GPa. The blue colored isosurfaces correspond to an equivalent plastic strain of $\varepsilon^{\text{(m)}}_{\text{eq,p}} = 0.023$ (the data corresponding to the other isosurfaces is given in the text). Particles are shown in magenta.
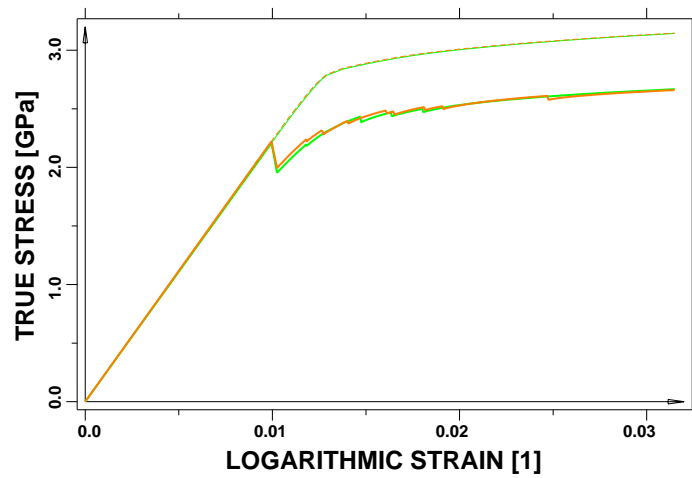
Figure 66: $HSS_{15\%}^{\mu8}$ and $HSS_{15\%}^{\mu9}$–C/MCW: Predicted overall stress-strain behavior. The green curve corresponds to microstructure $HSS_{15\%}^{\mu8}$ (7 vol.% of particles of type `carbide A`, 8 vol.% of type `carbide B`) and the orange curve to microstructure $HSS_{15\%}^{\mu9}$ (8 vol.% of particles of type `carbide A`, 7 vol.% of type `carbide B`). Both curves are averages of three simulations in three different loading directions.
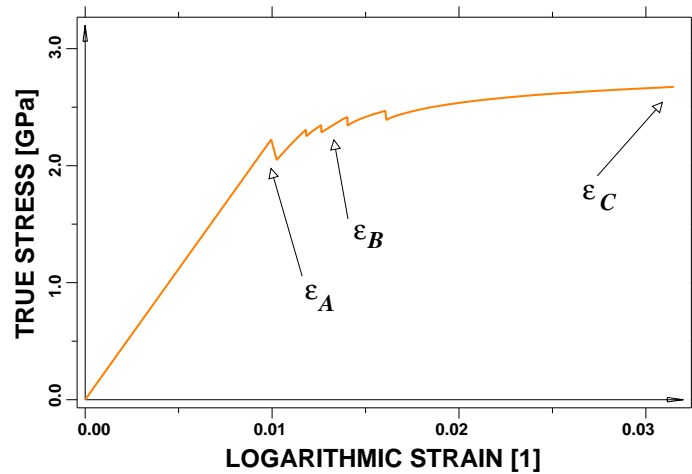

Figure 67: $HSS_{15\%}^{\mu9}$–C/MCW: Predicted stress-strain curve for model `C` (HSS with equally sized particles, a volume fraction of 8 % were modeled as type `carbide A` and 7 % as type `carbide B`, respectively) loaded in 1-direction (for the averaged behavior of a number of runs see figure 66, orange solid curve).
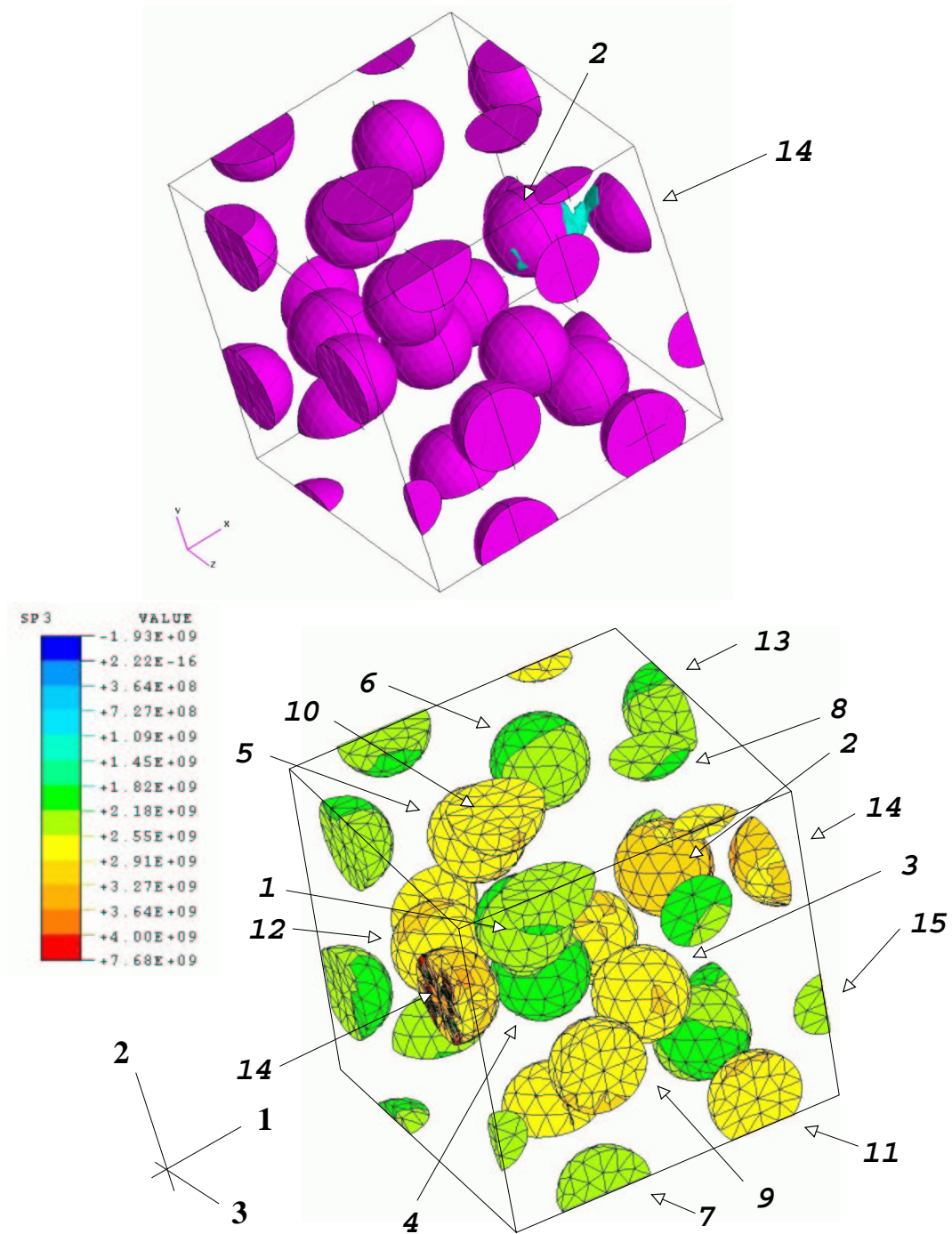
Figure 68: $\mathrm{HSS}^{\mu 9}_{15\%}$–C/MCW: Isosurfaces of equivalent plastic strain within the matrix (top, $\varepsilon^{(\mathrm{m})}_{\mathrm{eq,p}} = 0.0017$ is colored in turquoise; maximum value in this image: $\varepsilon^{(\mathrm{m})}_{\mathrm{eq,p}} = 0.014$) and maximum principal stresses within the particles (bottom). Tensile loading in 1-direction (overall strain: $\varepsilon^{\mathrm{a}}_A = 0.010$, $\sigma^{\mathrm{a}}_A = 2.22$ GPa – compare figure 67).
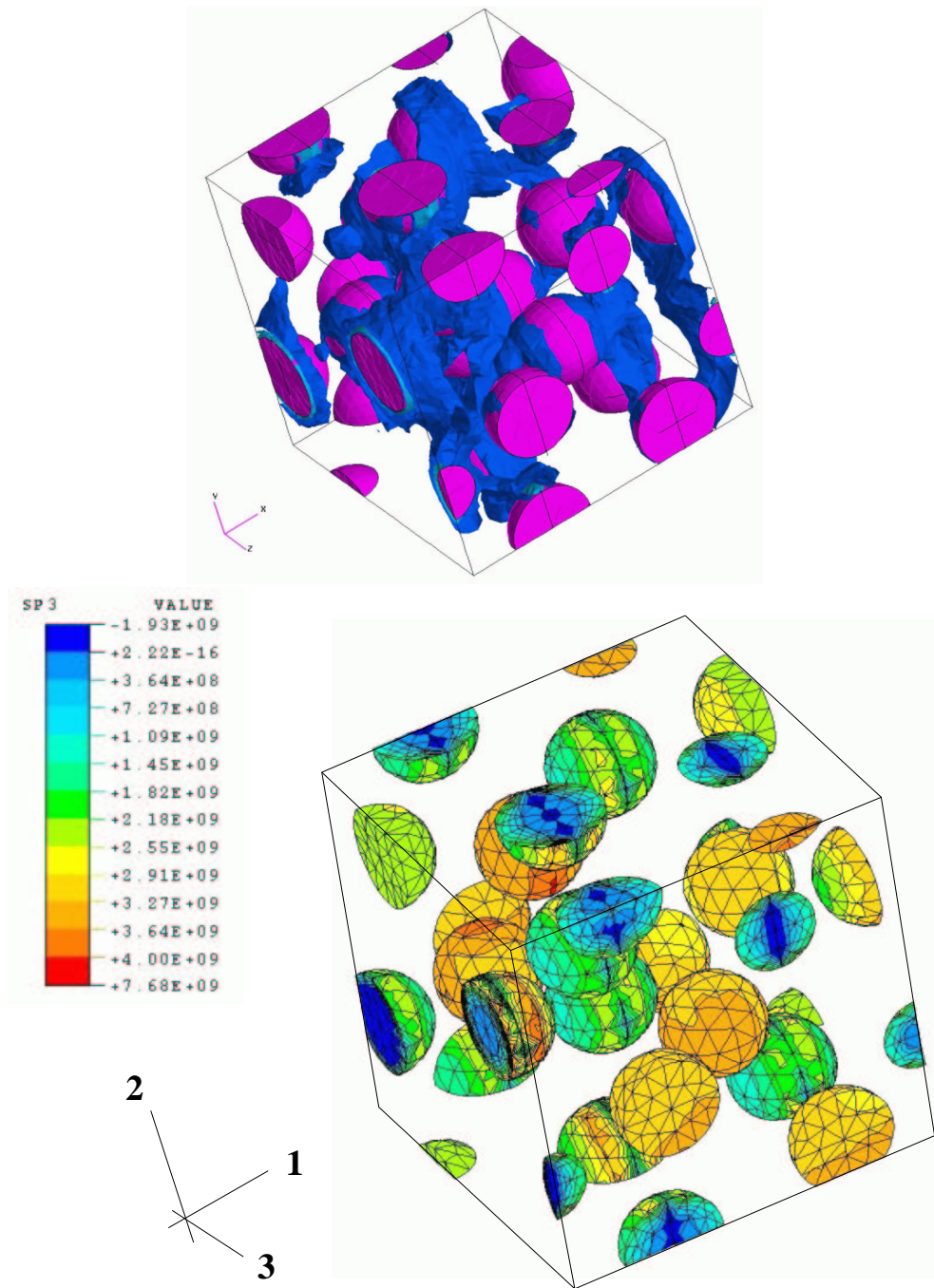
Figure 69: $\mathrm{HSS}^{\mu 9}_{15\%}$–C/MCW: Isosurfaces of equivalent plastic strain within the matrix (top, $\varepsilon^{(\mathrm{m})}_{\mathrm{eq,p}} = 0.013$ is colored in blue and $\varepsilon^{(\mathrm{m})}_{\mathrm{eq,p}} = 0.040$ in light blue; maximum value in this image: $\varepsilon^{(\mathrm{m})}_{\mathrm{eq,p}} = 0.19$) and maximum principal stresses within the particles (bottom) after the failure of nine particles. Tensile loading in 1-direction (overall strain: $\varepsilon^{\mathrm{a}}_B = 0.013$, $\sigma^{\mathrm{a}}_B = 2.29$ GPa – compare figure 67).
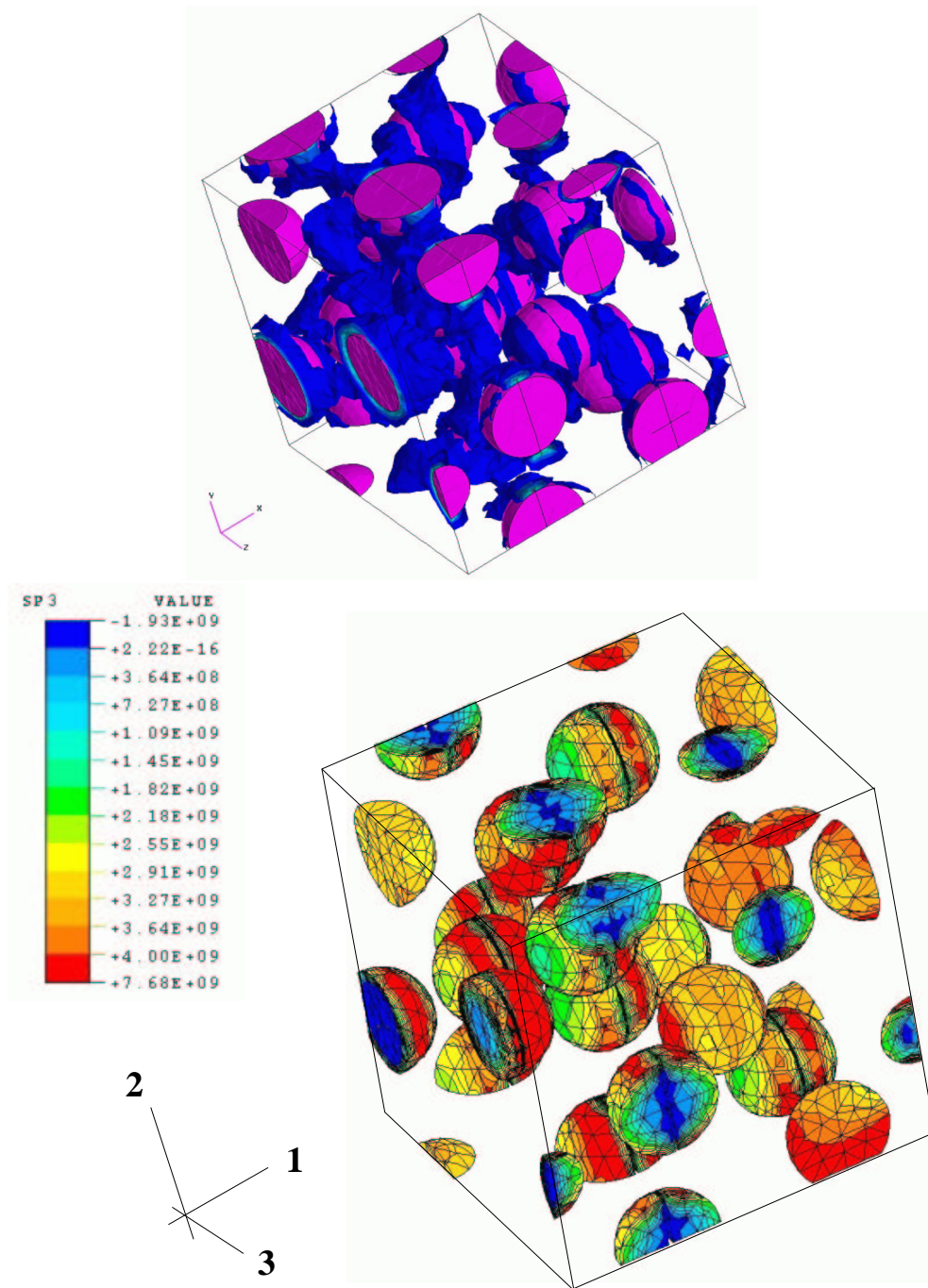
Figure 70: $\mathrm{HSS}^{\mu 9}_{15\%}$–C/MCW: Isosurfaces of equivalent plastic strain (top, $\varepsilon^{(\mathrm{m})}_{\mathrm{eq,p}} = 0.034$ is colored in blue and $\varepsilon^{(\mathrm{m})}_{\mathrm{eq,p}} = 0.14$ in turquoise; maximum value in this image: $\varepsilon^{(\mathrm{m})}_{\mathrm{eq,p}} = 0.52$) and corresponding maximum principal stresses within the particles (bottom) after overall loading in 1-direction up to $\varepsilon^{\mathrm{a}}_{C} = 0.032$ ($\sigma^{\mathrm{a}}_{C} = 2.67\,\mathrm{GPa}$) and after failure of eleven particles. For the corresponding stress-strain curve see figure 67.

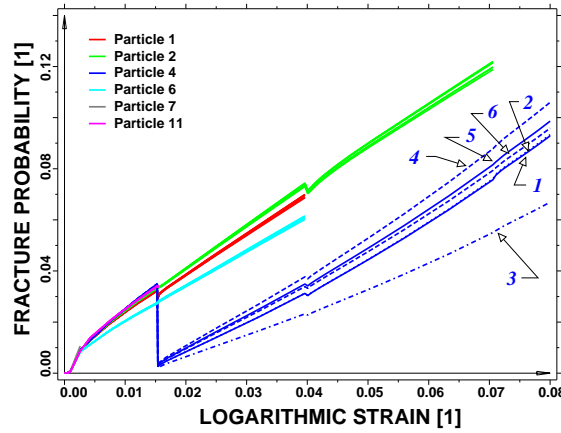*Figure 71:* AA2618/SiC$_{6.3p}^{eq}$-T4–`A`/`MCW`: Comparison of different methods for evaluating particle fracture probabilities. Tensile loading in 1-direction (one selected run out of the set presented in figure 25). Designations of curves correspond to the following methods: First Principal Stresses (1), All Principal Stresses (2), Complanar Energy Release Rate Criterion (3), Maximum Tangent Stress Criterion (4), Maximum Energy Release Rate Criterion (5), Richard Criterion (6). For detailed explanations see appendix A.3.

Figure 72: HSS$_{15\%}^{\mu6}$–`E`/`MCW`: Comparison of different methods for evaluating particle fracture probabilities. Tensile loading in 3-direction (results correspond to overall stress-strain curve (blue colored) given in figure 59). Designations of curves correspond to the following methods: First Principal Stresses (1), All Principal Stresses (2), Complanar Energy Release Rate Criterion (3), Maximum Tangent Stress Criterion (4), Maximum Energy Release Rate Criterion (5), Richard Criterion (6). For detailed explanations see appendix A.3.
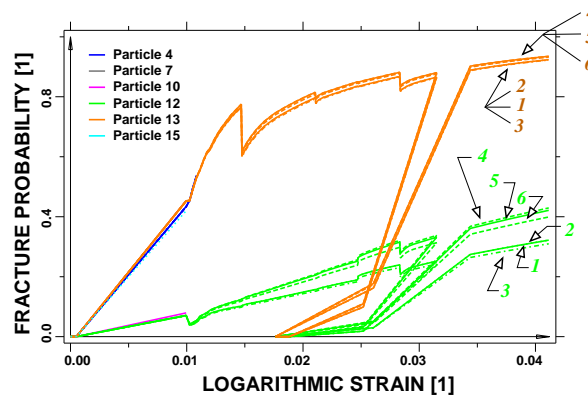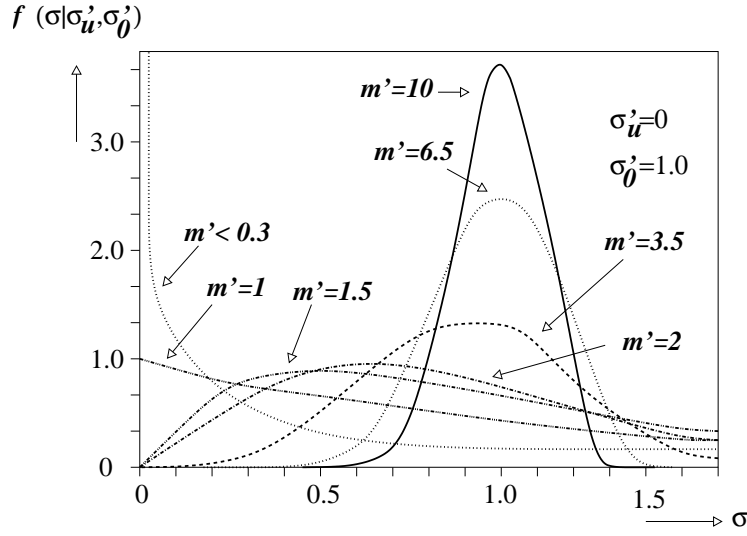
Figure 73: The standardized Weibull distribution density function $f = f(\sigma|\sigma'_u = 0, \sigma'_0 = 1, m')$ (two parametric) for different shape parameters m ("Weibull modulus"), see also eqn. (B.1), schematically drawn.
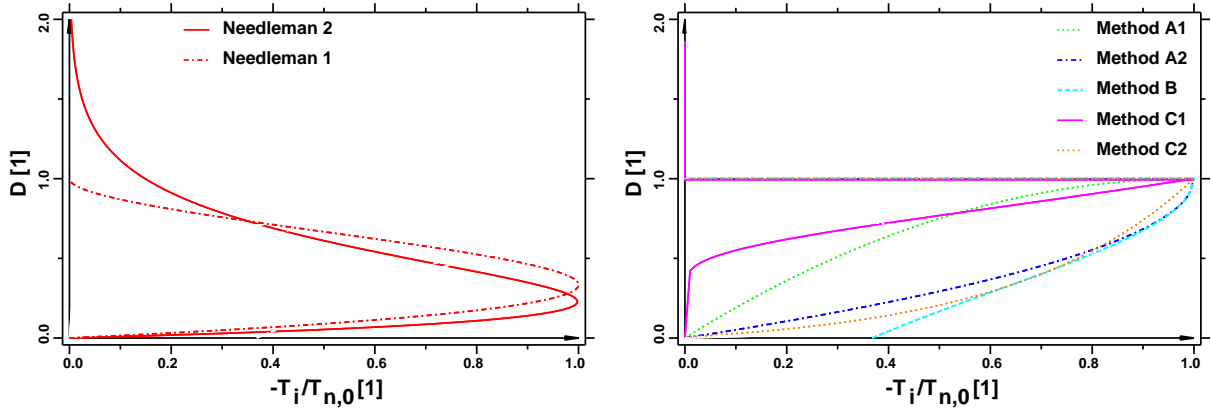
Figure 74: Separation relations for purely normal interfacial debonding $(i = \text{n})$ "Needleman 1", from Needleman [1987] and "Needleman 2", from Needleman [1990], left diagram, in comparison to the separation relations implemented within this work (valid for normal $i = \text{n}$ and tangential $i = \text{t}$ separation relations), right.

Appendix A

Overview and Comparison of Implemented Particle Failure Criteria

Within this work particle fracture probabilities are evaluated within the assumption of a mode I failure mechanism and fracture criteria based on Weibull-type statistics are used, the maximum principal stress being relevant for the Weibull fracture statistics. For comparison fracture criteria established in the literature are discussed, considering the predefined crack plane of each particle in the FE model (see chapter 3) as a loaded critical crack. Next the particle fracture criteria implemented in the ABAQUS subroutines are listed. The different properties of these methods are discussed in appendix A.3.

A.1   Methods Using Principal Stress Criteria

The density of risk of fracture, $n(\sigma_{\mathrm{I,eq}})$, can be used to evaluate the risk of fracture, B, of some volume V as

$$B = \int_V n(\sigma_{\mathrm{I,eq}}) \; dV \quad , \tag{A.1}$$

so that the fracture probability can be rewritten as

$$P_{\mathrm{fr}} = 1 - \exp(-B) \qquad . \tag{A.2}$$

In the following a number of methods for determining the equivalent mode I stress, $\sigma_{\mathrm{I,eq}}$, and consequently the risk of fracture, B, are introduced and compared.

Throughout the present work overall uniaxial tensile loading was applied for all simulations. Thus, as explained in detail in chapter 2, the so called **First Principal Stress - 3 Parameter Method** formulated as

$$B_j(\sigma_1) = \frac{1}{V_0} \int\limits_{V_j : \sigma_1(\underline{r}) \geq 0} \left(\frac{\sigma_1(\underline{r})}{\sigma_0} \right)^m \, dV \qquad (A.3)$$

was used. This method is valid for calculating the fracture probability of particle j, if mode I failure, a dominant maximum principal stress in the tensile range, and limited deviation of the orientation of the local principal stresses from the global load direction can be expected. For comparison, and to account for stress multiaxiality effects, an **All Principal Stresses - 3 Parameter Method**, based on the PIA was also tested. It evaluates the risk of fracture as

$$B_j(\sigma_1, \sigma_2, \sigma_3) = \frac{1}{V_0} \int\limits_{V_j} \left[\left(\frac{\sigma_1(\underline{r})}{\sigma_0} \right)^m + \left(\frac{\sigma_2(\underline{r})}{\sigma_0} \right)^m + \left(\frac{\sigma_3(\underline{r})}{\sigma_0} \right)^m \right] \, dV, \qquad (A.4)$$

where the intermediate and minimum principal stresses, σ_2 and σ_3, are also taken into account.

Based on these two equations, eqn. (A.3) and eqn. (A.4), in the literature sometimes variants that use a lower limit strength σ_{u} are used, to give the **First Principal Stress - 4 Parameter Method**

$$B_j(\sigma_1) = \frac{1}{V_0} \int\limits_{V_j : \sigma_1(\underline{r}) \geq 0} \left(\frac{\sigma_1 - \sigma_{\mathrm{u}}}{\sigma_0 - \sigma_{\mathrm{u}}} \right)^m \, dV \qquad (A.5)$$

and the **All Principal Stresses - 4 Parameter Method**

$$B_j(\sigma_1, \sigma_2, \sigma_3) = \frac{1}{V_0} \int\limits_{V_j} \left[\left(\frac{\sigma_1(\underline{r}) - \sigma_{\mathrm{u}}}{\sigma_0 - \sigma_{\mathrm{u}}} \right)^m + \left(\frac{\sigma_2(\underline{r}) - \sigma_{\mathrm{u}}}{\sigma_0 - \sigma_{\mathrm{u}}} \right)^m + \left(\frac{\sigma_3(\underline{r}) - \sigma_{\mathrm{u}}}{\sigma_0 - \sigma_{\mathrm{u}}} \right)^m \right] \, dV.$$
$$(A.6)$$

However, all these methods are based on a "direct relation" of the principal stress distribution within a particle to the fracture probability of a particle and do not regard any crack mechanism (only assuming mode I crack). Furthermore, only tensile principal stresses are considered, so the difference between eqns. (A.3) and (A.4) and between eqns. (A.5) and (A.6) are expected to be small for the present case of uniaxial tensile loading. In order to explicitly consider crack extension mechanisms Thiemeier [1987] and Heger [1993] suggested extensions as follows:

A.2   Methods Considering Fracture Criteria

For evaluating the risk of fracture B_j of particle j the equivalent stress for mode I fracture, $\sigma_{\mathrm{I,eq}}$, is evaluated considering a critical crack to occur in a plane the orientation of which is described by the angles φ (angle in xy-plane) and θ (angle to the positive z-axis). With the stress tensor $\underline{\underline{\sigma}}$ at position $\underline{r}$ and the crack orientation $\underline{n}$,

$$\underline{\underline{\sigma}} = \begin{pmatrix} \sigma_1 & \tau_{\mathrm{xy}} & \tau_{\mathrm{xz}} \\ \tau_{\mathrm{yx}} & \sigma_2 & \tau_{\mathrm{yz}} \\ \tau_{\mathrm{zx}} & \tau_{\mathrm{zy}} & \sigma_3 \end{pmatrix} \qquad \underline{n} = \begin{pmatrix} \sin\theta\cos\varphi \\ \sin\theta\sin\varphi \\ \cos\theta \end{pmatrix} \quad , \tag{A.7}$$

the stress vector, $\underline{\sigma}$, and its component normal to the crack plane, $\sigma_\perp$ (see figure 9), are determined as:

$$\underline{\sigma} = \underline{\underline{\sigma}} \cdot \underline{n} \qquad \sigma_\perp = \underline{\sigma} \cdot \underline{n} \tag{A.8}$$

whereas the shear stress in the crack plane (the in-plane component of $\underline{\sigma}$) is

$$\tau_\| = \sqrt{\underline{\sigma} \cdot \underline{\sigma} - \sigma_\perp^2} \quad . \tag{A.9}$$

For a planar circular crack in a 3D volume the stress intensity factors for loading in mode I, II and III can be written as

$$K_{\mathrm{I}} = \sigma_\perp \sqrt{a}\, Y_{\mathrm{I}} \qquad K_{\mathrm{II}} = \tau_\| \sqrt{a}\, Y_{\mathrm{II}} \qquad K_{\mathrm{III}} = \tau_\| \sqrt{a}\, Y_{\mathrm{III}} \quad , \tag{A.10}$$

the geometry factors being known analytically (Sih and Liebowitz [1965]) as

$$Y_{\mathrm{I}} = \frac{2}{\sqrt{\pi}} \tag{A.11}$$

$$Y_{\mathrm{II}} = \frac{4}{\sqrt{\pi}} \frac{1}{2-\nu} \cos\gamma \tag{A.12}$$

$$Y_{\mathrm{III}} = \frac{4}{\sqrt{\pi}} \frac{1-\nu}{2-\nu} \sin\gamma \quad , \tag{A.13}$$

Here ν stands for the Poisson's ratio and γ for the angle between the crack contour and the orientation of the shear stress $\tau_\|$, see figure 9.

The standard procedure for obtaining a failure criterion under pure mode I loading, which consists in comparing K_{I} to some critical stress intensity factor $K_{\mathrm{I,c}}$, can

be extended to more general load cases by defining an equivalent stress intensity factor $K_{\mathrm{I,eq}}(K_{\mathrm{I}}, K_{\mathrm{II}}, K_{\mathrm{III}})$ which is assessed with reference to $K_{\mathrm{I,c}}$. Alternatively, an "equivalent mode I stress" $\sigma_{\mathrm{I,eq}}$ can be compared to a critical mode I stress $\sigma_{\mathrm{I,c}}$, i.e.

$$
\left.
\begin{aligned}
&K_{\mathrm{I,eq}}(K_{\mathrm{I}}, K_{\mathrm{II}}, K_{\mathrm{III}}) \geq K_{\mathrm{I,c}} \\
&\sigma_{\mathrm{I,eq}}\left(\sigma_\perp(\varphi,\theta), \tau_\parallel(\varphi,\theta), \tfrac{Y_{\mathrm{II}}}{Y_{\mathrm{I}}}, \tfrac{Y_{\mathrm{III}}}{Y_{\mathrm{I}}}\right) \geq \sigma_{\mathrm{I,c}}
\end{aligned}
\right\} \Longrightarrow \text{failure}
\tag{A.14}
$$

In the present work the equivalent mode I stress is evaluated with the use of one of the methods listed in the following and used for the computation of the particle fracture probability based on Weibull's method. Due to the modeling technique just one crack plane is given for each particle, which is oriented normally to the overall maximum principal stress (see detailed explanations in chapter 2). For simplicity this crack plane is defined as the "critical" crack plane, so that the evaluation of the crack plane normal stresses $\sigma_\perp$ and the shear stresses $\tau_\parallel$ acting in the crack plane is trivial.

The following fracture criteria are well established in the literature (see Thiemeier [1987]), and were originally formulated for linear elastic multimode fracture. Here they are used for evaluating the failure probabilities of particles and are therefore rewritten in the "stress form" (normally these criteria are given in the stress intensity factor formulation using eqn. (A.10)):

Complanar Energy Release Rate Criterion: The most used criterion in the literature (the maximum value of $\sigma_{\mathrm{I,eq}}$ occurs at $\gamma = 0$, and therefore this value is used, see figure 9), that sets $K_{\mathrm{I,c}} = K_{\mathrm{II,c}}$, is, rewritten for the equivalent mode I stress

$$
\sigma_{\mathrm{I,eq}} = \sqrt{\sigma_\perp^2 + \tau_\parallel^2 \left(\frac{Y_{\mathrm{II}}}{Y_{\mathrm{I}}}\right)^2 + \left(\frac{\tau_\parallel^2}{1-\nu}\right)\left(\frac{Y_{\mathrm{III}}}{Y_{\mathrm{II}}}\right)^2} \quad .
\tag{A.15}
$$

Maximum Tangent Stress Criterion: Based on the hypothesis that crack growth occurs in the direction of the maximum tangential component of the stress tensor close to the crack tip:

$$
\sigma_{\mathrm{I,eq}} = \frac{\sqrt{8}\left[\left(2\sigma_\perp + 6\sqrt{\sigma_\perp^2 + 8\left(\frac{Y_{\mathrm{II}}}{Y_{\mathrm{I}}}\tau_\parallel\right)^2}\right)\left(\frac{Y_{\mathrm{II}}}{Y_{\mathrm{I}}}\tau_\parallel\right)^3\right]}{\left[\sigma_\perp^2 + 12\left(\frac{Y_{\mathrm{II}}}{Y_{\mathrm{I}}}\tau_\parallel\right)^2 - \sigma_\perp\sqrt{\sigma_\perp^2 + 8\left(\frac{Y_{\mathrm{II}}}{Y_{\mathrm{I}}}\tau_\parallel\right)^2}\right]^{1.5}}
\tag{A.16}
$$

Maximum Energy Release Rate Criterion: The crack growth orientation is given as a result of the maximum energy release rate:

$$\sigma_{\text{I,eq}} = \sqrt[4]{\sigma_\perp^4 + 6\sigma_\perp^2 \left(\frac{Y_{\text{II}}}{Y_{\text{I}}}\tau_\|\right)^2 + \left(\frac{Y_{\text{II}}}{Y_{\text{I}}}\tau_\|\right)^4} \tag{A.17}$$

The empirical Richard Criterion:

$$\sigma_{\text{I,eq}} = \frac{1}{2}\left[\sigma_\perp + \sqrt{\sigma_\perp^2 + 4\left(\frac{Y_{\text{II}}}{Y_{\text{I}}}\tau_\|\alpha_1\right)^2}\right] \qquad 0.5 < \alpha < 1.3 \quad \text{(found by experiment)}$$

$$\tag{A.18}$$

$\alpha = \frac{K_{\text{I,c}}}{K_{\text{II,c}}}$ is chosen as 1.0 in the present context.

The next section shows some typical results obtained with these methods.

A.3 Comparison of Different Methods for Evaluating Fracture Probabilities

In the main body of the present work the particle Weibull fracture probabilities are computed with the formulation given in eqn. (2.21), considering particle cleavage primarily as a classical mode I failure. In appendix A.1 a number of different methods for evaluating Weibull fracture probabilities are listed, closely following Thiemeier [1987], that are based, on the one hand, on simple combinations of principal stresses via the PIA and, on the other hand, consider different classical crack failure criteria. In this section a comparison of the methods is carried out by observing the Weibull fracture probabilities evaluated with the different methods.

First the unit cell model, arrangement `A`, with material properties of aluminium reinforced by silicon carbides is considered. The evolution of the fracture probabilities using the mentioned methods and predicted for a number of particles within the model during uniaxial loading, is shown in figure 71 (for the corresponding overall material response refer to figure 25). There the evolution of the fracture probabilities are shown for particles `7`, `11`, `1` and `6` (which fail in this sequence) as well as `2` and `4` (which survive the applied strain of $\varepsilon^{\text{a}} = 8\%$). By using the same random seed, different methods for evaluating the fracture probabilities could be compared. The different methods do not give noticably different results until after the first two particles have failed. From then on small differences between

the different curves can be discerned, which correspond to the methods "First Principal Stresses (*1*)", "All Principal Stresses (*2*)", "Complanar Energy Release Rate Criterion (*3*)", "Maximum Tangent Stress Criterion (*4*)", "Maximum Energy Release Rate Criterion (*5*)", and "Richard Criterion (*6*)", which are described in appendices A.1 and A.2.

In the investigation discussed here, using `RPC` unit cells and Al2618-T4 material properties, the small influence of the second and third principal stresses might be ascribed to the relatively low particle volume fraction and to the relatively large inter-particle distances. However, the same behavior was found for different unit cell models and different material properties, see figure 72. Despite the higher volume fractions (unit cell `C`) and the use of different material properties, the effects lie in the same same range and the influence on the intact particles' fracture probabilities, which are plotted for inclusions `12` and `13`, is recognizeable only after the failure of a number of particles.

Generally it can be stated that, when no particle failure occurs, all the introduced methods lead to very similar fracture probability values for globally uniaxial tensile load cases (which is in fact not surprising, as only one critical crack, oriented normal to the loading direction, is considered). With respect to the influence of the method used for evaluating the fracture probabilities of intact particles after the failure of some neighboring particles, methods *1* and *2* (First Principal Stresses and All Principal Stresses) give nearly identical results, method *3* (Complanar Energy Release Rate Criterion) predicts slightly lower, and methods *4* (Maximum Tangent Stress Criterion), *5* (Maximum Energy Release Rate Criterion) and *6* (Richard Criterion) predict slightly higher fracture probabilities.

For the present problem, i.e. modeling particle damage in uniaxially loaded particle reinforced metal matrix composites and disregarding other damage modes, method *1* evidently is sufficient for describing the macroscopic and microscopic material responses.

Appendix B

Some Mathematical Considerations on the Weibull Distribution

A continuous random variable σ satifies a three parameter Weibull-Distribution function with the parameters $m > 0$ and $\sigma - \sigma_\mathrm{u} > 0$, when the distribution density is given as

$$f(\sigma|\sigma_\mathrm{u}, \sigma_0, m) = \begin{cases} \frac{m}{\sigma_0} \left(\frac{\sigma - \sigma_\mathrm{u}}{\sigma_0} \right)^{m-1} \exp\left\{ -\left(\frac{\sigma - \sigma_\mathrm{u}}{\sigma_0} \right)^m \right\} & \forall \, \sigma \geq \sigma_\mathrm{u} \\ 0 & \forall \, \sigma < \sigma_\mathrm{u} \end{cases} \quad . \tag{B.1}$$

Consequently the distribution function $(F(\sigma) = \int\limits_{-\infty}^{\sigma} f(t) \, dt)$ is given as

$$F(\sigma|\sigma_\mathrm{u}, \sigma_0, m) := \begin{cases} 1 - \exp\left\{ -\left(\frac{\sigma - \sigma_\mathrm{u}}{\sigma_0} \right)^m \right\} & \forall \, \sigma \geq \sigma_\mathrm{u} \\ 0 & \forall \, \sigma < \sigma_\mathrm{u} \end{cases} \tag{B.2}$$

$m \in \mathrm{R}^+$ stands for the shape parameter (here Weibull parameter), $\sigma_\mathrm{u} \in \mathrm{R}^+$ is the location or threshold parameter, and $\sigma \in \mathrm{R}^+$ is the scale parameter. σ_u is often chosen as zero.

The mean value and the variance are obtained as (Gross and Seelig [2001]; Bronštein *et al.* [1999]):

$$\langle \sigma - \sigma_\mathrm{u} \rangle = \sigma \Gamma(1 + \frac{1}{m}) \qquad \mathrm{var}(\sigma - \sigma_\mathrm{u}) = \sigma^2 [\Gamma(1 + \frac{2}{m}) - \Gamma^2(1 + \frac{1}{m})] \tag{B.3}$$

In figures 7 and 73 the standardized (i.e. $\sigma_\mathrm{u} = 0$ and $\sigma_0 = 1$) Weibull density function and the Weibull distribution function (Ashby and Jones [1986]), respectively, are plotted:

$$F(\sigma|0, 1, m) = 1 - \exp\{-\sigma^m\} \tag{B.4}$$

In the following the Weibull function is discussed. Setting $m = 1$ reduces the function to the exponential distribution. In the literature the case of $m = 2$ is called Rayleigh-Distribution (Bosch [1996]; Reidinger [1989]). For the present application of Weibull functions only the region $m > 0$ is of interest (figures 7, 73).

- $m \rightarrow 0$: the smaller m is chosen, the more the density curve is concentrated to the ordinate and becomes a Dirac-distribution.

- $0 < m < 1$: the Weibull density $f(\sigma|m)$ falls monotonously and convexly (Reidinger [1989] shows, that for $m \leq \frac{1}{5}$ the zero points are not real and therefore inflection points do not exist).

- $m = 0$: the monotonous, convexly falling density-function of the exponential distribution is obtained. The inflection points are in the origin.

- $1 < m \leq 2$: one inflection point exists for positive σ. The maximum of the density function (Bosch [1996]) moves to the right side with increasing m.

- $m > 2$: two inflection points are now in the positive region, one on each side of the maximum of the density function. The curve becomes more and more symmetric.

- for $m \rightarrow \infty$ the density becomes a Dirac-distribution at $\sigma = 1$:

$$\lim_{m \to \infty} f(\text{max}|\text{m}) = \infty \tag{B.5}$$

where "max" represents the maximum of the density function. The corresponding distribution function is a step function at $\sigma = 1$.

Appendix C

Interfacial Decohesion

With the user subroutines implemented within the present work, and if the FE-model is approximately prepared, also interfacial debonding can be modeled. The nodal stress components and the magnitudes of the normal and tangential components of the tractions are evaluated, and node release is triggered by a separation function similar to the ones used in the Cohesive Zone Models (note that implementations of the latter type using ABAQUS, e.g. that by Scheider [2000], have employed **U**ser defined **EL**ements (UEL) (see Hibbitt *et al.* [1998]) instead). Concentrating on the interfacial failure and assuming a crack orientation within the boundary defined by the particle's surface and the surrounding matrix makes a crack orientation treatment as carried out e.g. by Ohmenhäuser *et al.* [1999] unnecessary.

In Needleman [1987] the mechanical response of the interface is described via a constitutive relation that gives the dependence of the tractions T_i on the separation u_i. This response in terms of a polynomial potential Φ dependent only on the displacement difference across the interface is chosen in such way, that during the interface separation the tractions increase, achieve a maximum and fall to zero when complete separation has occured. For purely normal separation (no shear is present) the normal interfacial tractions $-\frac{T_n}{T_{n,0}}$ are related to the separation $d_n = \frac{u_n}{\delta_{n,0}}$ as presented in figure 74, curve "Needleman 1", where the maximum interfacial stress is achieved at $u_n = \delta$ and complete separation occurs when $u_n = \delta_{n,0}$ (i.e. a well defined decohesion point). The modification of the traction-separation relation, as given in Needleman [1990]; Scheider [2000], where exponential forms in the style of atomistic calculations of interfacial separation are introduced, leads to the correlation "Needleman 2" in figure 74 for purely normal decohesion. The exponential potential vanishes only at $u_n \to \infty$ and the separation work done between

$u_{\mathrm{n}} = 0$ and $u_{\mathrm{n}} = \delta$ would be about 0.95 Φ_{sep}.

In contrast to the above approaches within the present work a node release technique is used and a separation relation is used in the reverse direction. The traction values at nodes lying in the interface affect individual separations $d_{\mathrm{n}}, d_{\mathrm{t}}$, evaluated by a simple correlation of "virtual displacement" and "actual traction" fulfilling the conditions of $(i = \mathrm{n}, \mathrm{t})$

- full separation $d_i = \frac{u_i}{\delta_{i,0}}$ at $u_i = \delta_{i,0}$ and

- a limiting traction for $T_i = T_{i,0}$.

For the first assumption the separation relations for normal debonding are the same as for tangential separation and we chose to closely approach the rising part of the $d = d(T)$-relations of Needleman [1990]. The three implemented separation relations (normally the parameters are chosen to fulfill $M_i = M_{\mathrm{n}} = M_{\mathrm{t}} = M_2$) are:

Method A (compare figure 74: A1: $M_i = 0.5$, A2: $M_i = 3$):

$$d_i = 1 - \left(1 - \frac{T_i}{T_{i,0}}\right)^{\frac{1}{M_i}} \tag{C.1}$$

Method B (compare figure 74: $M_i = 0.5$):

$$d_i = 1 - \left(-\ln\left|\frac{T_i}{T_{i,0}}\right|\right)^{\frac{1}{M_i}} \tag{C.2}$$

Method C (compare figure 74: C1: $M_i = 0.5$, C2: $M_i = 3$):

$$d_i = \frac{1}{1 + \left(-\ln\left|\frac{T_i}{T_{i,0}}\right|\right)^{\frac{1}{M_i}}} \tag{C.3}$$

In figure 74 the separation relations are compared with the relations given by Needleman [1987, 1990] for some values of M_i. The individual expressions for normal and tangential separation are combined (mostly using $M_1 = 2$) to a total separation d with

$$d = \left(d_{\mathrm{n}}^{M_1} + d_{\mathrm{t}}^{M_1}\right)^{\frac{1}{M_1}} . \tag{C.4}$$

The algorithm is implemented at the interface nodes and at neighboring matrix nodes (in the direction of expected matrix crack growth) assuming the knowledge of the crack path. Interface (matrix) failure (i.e. node release) occurs, if d is close to 1 (mostly $d \geq 0.98$

was chosen). An implemented procedure limits the motion of the released nodes to gliding on the inclusion surface or movement away from it and penetration of matrix nodes into the inclusion is prevented. For numerical reasons mainly method `A1` was used.

Without doubt the specific choice of the potential has limited physical interpretation (equal to a problem of a body lying on a surface with friction) and is mesh dependent (averaged stress values at the element nodes are used for calculation). Nevertheless it has been used for first investigations in developing interfacial failure node release modeling and seems to be a promising principle.

Bibliography

Antretter, T. (1998); *Micromechanical Modeling of High Speed Steel*, vol. 18/232 of *Fortschrittberichte VDI*, VDI Verlag, Düsseldorf.

Antretter, T. and Fischer, F. D. (1998); Particle Cleavage and Ductile Crack Growth in a Two-Phase Composite on a Microscale, *Comp. Mat. Sci.*, 13: 1–7.

Ashby, M. F. and Jones, D. R. H. (1986); *Engineering Materials II*, vol. 1, pp. 169–177, Pergamon Press, Oxford UK.

Batdorf, S. B. and Crose, J. G. (1974); A Statistical Theory for the Fracture of Brittle Structures Subjected to Nonuniform Polyaxial Stresses, *J. Appl. Mech.*, 41/2: 459–464.

Berns, H., Melander, A., Weichert, D., Asnafi, N., Broeckmann, C. and Gross-Weege, A. (1998); A New Material for Cold Forging Tools, *Comp. Mat. Sci.*, 11: 166–188.

Böhm, H. J. (1991); *Computer Based Micromechanical Investigations of the Thermomechanical of Metal Matrix Composites*, vol. 18/101 of *Fortschrittberichte VDI*, VDI Verlag, Düsseldorf.

Böhm, H. J. and Han, W. (2001); Comparisons Between Three-Dimensional and Two-Dimensional Multi-Particle Unit Cell Models for Particle Reinforced Metal Matrix Composites, *Modell. Simul. Mater. Sci. Eng.*, 9: 47–65.

Böhm, H. J., Han, W. and Eckschlager, A. (2002); Multi-Inclusion Unit Cell Studies of Reinforcement Stresses and Particle Failure in Discontinuously Reinforced Ductile Matrix Composites, *submitted to Comput. Meth. Eng. Sci.*.

Bosch, K. (1996); *Grosses Lehrbuch der Statistik*, R. Oldenbourg Verlag, München, Wien.

Bréchet, Y., Embury, J. D., Tao, S. and Luo, L. (1991); Damage Initiation in Metal Matrix Composites, *Acta Metall. Mater.*, 39/8: 1781–1786.

Broeckmann, C. (1996); *Progress in Tool Steels*, vol. 1, chap. Fracture of Tool Steel on a Microscopical Scale, pp. 491–499, Schürmann and Klagges, Bochum.

Broeckmann, C. (2001); *Kriechen partikelverstärkter metallischer Werkstoffe*, vol. 5/612 of *Fortschrittberichte VDI*, VDI Verlag, Düsseldorf.

Bronštein, I. N., Semendjajew, K. A., Musiol, G. and Mühlig, H. (1999); *Taschenbuch der Mathematik*, Verlag Harri Deutsch, Frankfurt, 4th edn.

Bulsara, V. N., Talreja, R. and Qu, J. (1999); Damage Initiation under Transverse Loading of Unidirectional Composites with Arbitrarily Distributed Fibers, *Comp. Sci. and Tech.*, 59: 673–682.

Clyne, T. W. and Withers, P. J. (1993); *An Introduction to Metal Matrix Composites*, Cambridge University Press, Cambridge UK.

Danzer, R. (1992); A General Strength Distribution Function for Brittle Materials, *J. European Ceram. Soc.*, 10: 461–472.

Danzer, R., Reisner, G. and Schubert, H. (1992); Der Einfluß von Gradienten in der Defektdichte und Festigkeit auf die Bruchstatistik von spröden Werkstoffen, *Z. Metallkd.*, 83/7: 508–517.

Drugan, J. and Willis, J. R. (1996); A Micromechanics-based Nonlocal Consitutive Equation and Estimates of Representative Volume Element Size for Elastic Composites, *J. Mech. Phys. Solids*, 44: 497–524.

Duffy, S. F. and Arnold, S. M. (1990); Noninteractive Macroscopic Reliability Model for Whisker-Reinforced Ceramic Composites, *J. Comp. Mat.*, 24: 293–308.

Eckschlager, A. and Böhm, H. J. (2002); 3D Finite Element Unit Cell Study of Particle Failure in Brittle Particle Reinforced Ductile Matrix Composites, in *Fifth World Congress on Compuational Mechanics (WCCM V)* (edited by H. A. Mang, F. G. Rammerstorfer and J. Eberhardsteiner), p. No. 80869.

Eckschlager, A., Böhm, H. J. and Han, W. (2001a); Modeling of Brittle Particle Failure in Particle Reinforced Ductile Matrix Composites by 3D Unit Cells, in *Proceedings of the 13th International Conference on Composite Materials ICCM-13* (edited by Y. Zhang), p. No. 1342, Scientific and Technical Documents Publishing House, Beijing, China.

Eckschlager, A., Böhm, H. J. and Han, W. (2001b); A Unit Cell Model for Brittle Fracture of Particles Embedded in a Ductile Matrix, *Comp. Mat. Sci., in print*.

Elomari, S., Skibo, M. D., Sundarrajan, A. and Richards, H. (1998); Thermal Expansion Behavior of Particulate Metal–Matrix Composites, *Comp. Sci. and Tech.*, 58: 369–376.

Eshelby, J. D. (1957); The Determination of the Elastic Field of an Ellipsoidal Inclusion and Related Problems, *Proc. R. Soc. Lond. A*, 241: 376–396.

Estevez, R., Maire, E., Franciosi, P. and Wilkinson, D. S. (1999); Effect of Particle Clustering on the Strengthening versus Damage Rivalry in Particulate Reinforced Elastic Plastic Materials: A 3-D Analysis from a Self-Consistent Modelling, *Eur. J. Mech. A/Solids*, 18: 785–804.

Finot, M., Shen, Y.-L., Needleman, A. and Suresh, S. (1994); Micromechanical Modeling of Reinforcement Fracture in Particle-Reinforced Metal-Matrix Composites, *Metall. and Mat. Trans. A*, 25A: 2403–2420.

Fischer, F. D., Kolednik, O., Shan, G. and Rammerstorfer, F. G. (1995); A Note on Calibration of Ductile Failure Damage Indicators, *Int. J. Fract.*, 73: 345–357.

Flom, Y. and Arsenault, R. J. (1986); Interfacial Bond Strength in an Aluminum Alloy 6061–SiC Composite, *Materials Sci. Eng.*, 77: 191–197.

Freudenthal, A. M. (1965); *Statistical Approach to Brittle Fracture*, vol. 2, pp. 591–619, Academic Press, New York and London.

Ghosh, S. and Moorthy, S. (1998); Particle Fracture Simulation in Non-Uniform Microstructures of Metal-Matrix Composites, *Acta Mater.*, 46: 965–982.

Goods, S. H. and Brown, L. M. (1978); The Nucleation of Cavities by Plastic Deformation, *Acta Metall.*, 27: 1–15.

Green, D. J. (1998); An Introduction to the Mechanical Properties of Ceramics, *Cambridge University Press, Cambridge UK*.

Gross, D. and Seelig, T. (2001); *Bruchmechanik*, Springer-Verlag Berlin, 3rd edn.

Gross-Weege, A. (1996); *Deformation and Damage Behavior of Particle Reinforced Metal Matrix Composites*, Ph.D. thesis, Ecole Universitaire d'Ingeniéurs de Lille.

Gross-Weege, A., Weichert, D. and Broeckmann, C. (1996); Finite Element Simulation of Crack Initiation in Hard Two-Phase Materials, *Comp. Mat. Sci.*, 5: 126–142.

Gunawardena, S. R., Jansson, S. and Leckie, F. A. (1991); Transverse Ductility of Metal Matrix Composites, in *Failure Mechanisms in High Temperature Composite Materials* (edited by K. Haritos, G. Newaz and S. Mall), vol. AD–Vol.22/AMD–Vol.122, pp. 23–30, ASME, New York, NY.

Gurson, A. L. (1977); Continuum Theory of Ductile Rupture by Void Nucleation and Growth: Part I — Yield Criteria and Flow Rules for Porous Ductile Media, *J. Eng. Mat. Technol.*, 99: 2–15.

Gusev, A. A. (1997); Representative Volume Element Size for Elastic Composites: A Numerical Study, *J. Mech. Phys. Solids*, 45/9: 1449–1459.

Gyekenyesi, J. P. and Nemeth, N. N. (1987); Surface Flaw Reliability Analysis of Ceramic Components With the SCARE Finite Element Postprocessor Program, *J. Eng. Gas Turbines and Power*, 109: 274–281.

Han, W. and Böhm, H. J. (2002); *Unit Cell Studies of Discontinuously Reinforced Metal Matrix Composites and High Speed Steels*, vol. 37-01 of *CDL-FMD Reports*, TU Wien.

Han, W., Eckschlager, A. and Böhm, H. J. (2001a); The Effects of Three-Dimensional Multi-Particle Arrangements on the Mechanical Behavior and Damage Initiation of Particle-Reinforced MMCs, *Comp. Sci. and Tech.*, 61: 1581–1590.

Han, W., Eckschlager, A. and Böhm, H. J. (2001b); Numerical Modeling of Discontinuously Reinforced MMCs by Three-Dimensional Multi-Inclusion Unit Cells, in *Proceedings of the 13th International Conference on Composite Materials ICCM-13* (edited by Y. Zhang), p. No. 1222, Scientific and Technical Documents Publishing House, Beijing, China.

Hancock, J. W. and Mackenzie, A. C. (1976); On the Mechanics of Ductile Failure in High Strength Steels Subjected to Multi-Axial Stress States, *J. Mech. Phys. Solids*, 24: 147–169.

Hashin, Z. (1983); Analysis of Composite Materials–A Survey, *J. Appl. Mech.*, 50: 481–505.

Heger, A. (1993); *Bewertung der Zuverlässigkeit mehrachsig belasteter keramischer Bauteile*, Ph.D. thesis, Universität Karlsruhe.

Hibbitt, Karlsson and Sorensen Inc. (1998); *ABAQUS/Standard V.5.8.*, Pawtucket RI.

Ho, S. and Lavernia, E. (1995); Thermal Residual Stresses in Metal Matrix Composites: A Review, *Appl. Comp. Mat.*, 2: 1–30.

Hom, C. L. and McMeeking, R. M. (1991); Plastic Flow in Ductile Materials Containing a Cubic Array of Rigid Spheres, *Int. J. Plast.*, 7: 255–274.

Hunt, R. A. and McCartney, L. N. (1979); A New Approach to Weibull's Statistical Theory of Brittle Fracture, *Int. J. Fract.*, 15: 362–375.

Iung, T. and Grange, M. (1995); Mechanical Behavior of Two-Phase Materials Investigated by the Finite Element Method: Necessity of Three-Dimensional Modeling, *Materials Sci. Eng.*, A201: L8–L11.

Kouzeli, M., Weber, L., Marchi, C. S. and Mortensen, A. (2001); Influence of Damage on the Tensile Behavior of Pure Aluminium Reinforced with $\geq$ 40 vol. pct. Alumina Particles, *Acta Mater.*, 49: 3699–3709.

Lee, J. C. and Subramanian, K. N. (1992); Failure Behavior of Particulate-Reinforced Aluminum Alloy Composites under Uniaxial Tension, *J. Mat. Sci.*, 27: 5453–5462.

Lewis, C. A. and Withers, P. J. (1995); Weibull Modelling of Particle Cracking in Metal Matrix Composites, *Acta Metall. Mater.*, 43: 3685–3699.

Li, C. and Ellyin, F. (1998); A Micro-Macro Correlation Analysis For Metal-Matrix Composites undergoing Multiaxial Damage, *Int. J. Sol. Struct.*, 35/7-8: 637–649.

Lippmann, N. (1995); *Beitrag zur Untersuchung des Bruchverhaltens von Werkzeugen aus Schnellarbeitsstählen unter statischer Beanspruchung*, Ph.D. thesis, Technische Universität Bergakademie Freiberg.

Lippmann, N., Lehmann, A., Steinkopff, T. and Spies, H.-J. (1996); Modelling the Fracture Behaviour of High Speed Steels Using Finite Element Method, *Comp. Mat. Sci.*, 7: 123–130.

LLorca, J. (1996); A Numerical Analysis of the Damage Mechanisms in Metal-Matrix Composites under Cyclic Deformation, *Comp. Mat. Sci.*, 7: 118–122.

LLorca, J. and González, C. (1998); Microstructural Factors Controlling the Strength and Ductility of Partile Reinforced Metal-Matrix Composites, *J. Mech. Phys. Solids*, 46: 1–28.

LLorca, J., Martín, A., Ruiz, J. and Elices, M. (1993); Particulate Fracture during Deformation of a Spray Formed Metal Matrix Composite, *Metall. Trans.*, A24: 1575–1588.

LLorca, J., Martínez, J. L. and Elices, M. (1997); Reinforcement Fracture and Tensile Ductility in Sphere-Reinforced Metal-Matrix Composites, *Fatigue Fract. Eng. Mat. Struct.*, 20/5: 689–702.

LLorca, J., Needleman, A. and Suresh, S. (1991); An Analysis of the Effects of Matrix Void Growth on Deformation and Ductility in Metal–Ceramic Composites, *Acta Metall. Mater.*, 39/10: 2317–2335.

LLorca, J. and Poza, P. (1995); Influence of Reinforcement Fracture on the Cyclic Stress-Strain Curve of Metal-Matrix Composites, *Acta Metall. Mater.*, 43/11: 3959–3969.

MacNeal-Schwendler Corp. (1998); *MSC/PATRAN V.8.0.*, Los Angeles CA.

Margetson, J. and Cooper, N. R. (1984); Brittle Material Design Using Three Parameter Weibull Distributions, in *Probabilistic Methods in the Mechanics of Solids and Structures* (edited by N. C. L. S. Eggwertz), pp. 253–262, Springer-Verlag Berlin.

Markov, K. (2000); *Elementary Micromechanics of Heterogeneous Media*, pp. 1–162, K. Markov and L. Preziosi, Birkhäuser Boston, MA.

Mawsouf, N. M. (2000); A Micromechanical Mechanism of Fracture Initiation in Discontinuously Reinforced Metal Matrix Composite, *Mater. Charact.*, 44: 321–327.

Miodownik, A. P. (1994); Young's Modulus for Carbides of $3d$ Elements (With Particular Reference to FeC_3), *Materials Sci. Technol.*, 10/3: 190–192.

Mishnaevsky, L., Dong, M., Hönle, S. and Schmauder, S. (1999); Computational Mesomechanics of Particle-Reinforced Composites, *Comp. Mat. Sci.*, 16: 133–143.

Mishnaevsky, L., Lippmann, N. and Schmauder, S. (2001); Experimental-Numerical Analysis of Mechanics of Damage Initiation in Tool Steels, in *Proc. 10th International Conference Fracture, Honolulu, HA*.

Mummery, P. M., Derby, B. and Scruby, C. B. (1993); Acoustic Emission from Particulate Metal Matrix Composites, *Acta Metall. Mater.*, 41/5: 1431–1445.

Mura, T. (1987); *Micromechanics of Defects in Solids*, Kluwer Academic Publishers, Dordrecht, NL, 2nd edn.

Needleman, A. (1987); A Continuum Model for Void Nucleation by Inclusion Debonding, *J. Appl. Mech.*, 54: 525–531.

Needleman, A. (1990); An Analysis of Decohesion Along an Imperfect Interface, *Int. J. Fract.*, 42: 21–40.

Nutt, S. R. and Needleman, A. (1987); Void Nucleation at Fiber Ends in Al–SiC Composites, *Scripta metall.*, 21: 705–710.

Ohmenhäuser, F., Weihe, S. and Kröplin, B. (1999); Algorithmic Implementation of a generalized Cohesive Crack Model, *Comp. Mat. Sci.*, 16: 294–306.

Pandorf, R. (2000); *Beitrag zur FE-Simulation des Kriechens partikelverstärkter Metallmatrix-Verbundwerkstoffe*, vol. 5/585 of *Fortschrittberichte VDI*, VDI Verlag, Düsseldorf.

Plankensteiner, A. (2000); *Multiscale Treatment of Heterogeneous Nonlinear Solids and Structures*, vol. 18/248 of *Fortschrittberichte VDI*, VDI Verlag, Düsseldorf.

Polmear, I. J. (1995); *Light Alloys: Metallurgy of the Light Metals*, Halsted Press, Wiley, London, 3rd edn.

Pyrz, R. (1994a); Correlation of Microstructure Variability and Local Stress Field in Two-Phase Materials, *Materials Sci. Eng.*, A177: 253–259.

Pyrz, R. (1994b); Quantitative Description of the Microstructure of Composites. Part I: Morphology of Unidirectional Composite systems, *Comp. Sci. and Tech.*, 50: 197–208.

Reidinger, M. (1989); *Die Weibull-Verteilung als stochastisches Modell in der Zuverlässigkeitsanalyse*, Master's thesis, Vienna University of Technology.

Rice, J. R. and Tracey, D. M. (1969); On the Ductile Enlargement of Voids in Triaxial Stress Fields, *J. Mech. Phys. Solids*, 17: 201–217.

Rintoul, M. and Torquato, S. (1997); Reconstruction of the Structure of Dispersions, *J. Colloid Interf. Sci.*, 186: 467–476.

R'Mili, M., Bouchaour, T. and Merle, P. (1996); Estimation of Weibull Parameters from Loose-Bundle Tests, *Comp. Sci. and Tech.*, 56: 831–834.

Scheider, I. (2000); Kohäsivzonenmodell für die Modellierung von Rißfortschritt in Bauteilen mit elastisch-plastischem Materialverhalten. Teil 1: Grundlagen und Implementierung, *Interner Bericht GKSS*, Technical Note GKSS/WMS/00/19: 1–32.

Schöberl, J. (1997); NETGEN – An Advancing Front 2D/3D-Mesh Generator Based On Abstract Rules, *Comput. Visual. Sci.*, 1: 41–52, available at http://nathan.numa.uni–linz.ac.at/Staff/joachim/papers/netgen.ps.gz.

Sih, G. C. and Liebowitz, H. (1965); *Mathematical Theories of Brittle Fracture*, vol. 2, pp. 67–190, Academic Press, New York and London.

Stanley, P., Fessler, H. and Sivill, A. (1973); An Engineer's Approach to the Prediction of Failure Probability of Brittle Components, *Proc. Brit. Cer. Soc.*, 22: 453.

Steglich, D. (1999); *Bestimmung von mikrostrukturellen Parametern in Schädigungsmodellen für duktile Metalle*, Ph.D. thesis, TU Berlin.

Suresh, S., Mortensen, A. and Needleman, A. (1993); *Fundamentals of Metal Matrix Composites*, Butterworth-Heinemann, Boston, MA.

Sutherland, L. S., Sheno, R. A. and Lewis, S. M. (1999); Size and Scale Effects in Composites: I. Literature Review, *Comp. Sci. and Tech.*, 59: 209–220.

Thiemeier, T. (1987); *Lebensdauervorhersage für keramische Bauteile unter mehrachsiger Beanspruchung*, Ph.D. thesis, Universität Karlsruhe.

Tohgo, K. and Weng, G. J. (1994); A Progressive Damage Mechanics in Particle-Reinforced Metal-Matrix Composites under High Triaxial Tension, *J. Eng. Mat. Technol.*, 116: 414–420.

Tvergaard, V. (1982); Influence of Void Nucleation on Ductile Shear Fracture at a Free Surface, *J. Mech. Phys. Solids*, 30/6: 399–425.

Tvergaard, V. and Needleman, A. (1984); Analysis of the Cup-Cone Fracture in a Round Tensile Bar, *Acta Metall.*, 32/1: 157–169.

Wallin, K., Saario, T. and Törrönen, K. (1987); Fracture of Brittle Particles in a Ductile Matrix, *Int. J. Fract.*, 32: 201–209.

Weibull, W. (1939); A Statistical Theory of the Strength of Materials, *Ingeniörsvetenskapsakademiens Handlingar*, 151: 5–45.

Weibull, W. (1951); A Statistical Distribution Function of Wide Applicability, *J. Appl. Mech.*, 18: 293–298.

Weissenbek, E. (1994); *Finite Element Modelling of Discontinuously Reinforced Metal Matrix Composites*, vol. 18/164 of *Fortschrittberichte VDI*, VDI Verlag, Düsseldorf.

Weissenbek, E., Böhm, H. and Rammerstorfer, F. (1994); Micromechanical Investigations of Arrangement Effects in Particle Reinforced Metal Matrix Composites, *Comp. Mat. Sci.*, 3: 263–278.

Weißmantel, C. and Hamann, C. (1980); *Grundlagen der Festkörperphysik*, Springer-Verlag Berlin Heidelberg.

Curriculum Vitae

Personal Data

Name   :   Anton Eckschlager
Date of birth :   October 25, 1971
Place of birth :   Salzburg, Austria
Citizenship   :   Austrian

Education

1999 – 2002	Doctoral Student at the Christian Doppler Laboratory for Functionally Oriented Materials Design at the Institute of Light Weight Structures and Aerospace Engineering, Vienna University of Technology, Vienna/Austria.
1990 – 1997	Studies of "Technical Physics" at the University of Technology, Graz/Austria, graduation date with the degree of Diplom-Ingenieur: January 8, 1997.
1985 – 1990	Technical High School (HTL) in Electrical Engineering "Höhere Technische Bundeslehranstalt", Salzburg/Austria, graduation date: October 15, 1990.
1981 – 1985	4 years Secondary School in Eugendorf/Austria.
1977 – 1981	4 years Primary School in Eugendorf/Austria.

Employment

Dec. 1998 – July 2002	Research assistant at the Christian Doppler Laboratory for Functionally Oriented Materials Design at the Institute of Light Weight Structures and Aerospace Engineering, Vienna University of Technology.
Dec. 1997 – Dec. 1998	System integration analyst with Siemens PSE Vienna and Munich.
Dec. 1990 – Oct. 1991	Project manager with Salzburger Aufzugdienst Ges.m.b.H.